

University of New Hampshire

University of New Hampshire Scholars' Repository

Master's Theses and Capstones

Student Scholarship

Winter 2010

Deep Ocean Delivery System

Carin Campbell

University of New Hampshire, Durham

Follow this and additional works at: <https://scholars.unh.edu/thesis>

Recommended Citation

Campbell, Carin, "Deep Ocean Delivery System" (2010). *Master's Theses and Capstones*. 831.
<https://scholars.unh.edu/thesis/831>

This Thesis is brought to you for free and open access by the Student Scholarship at University of New Hampshire Scholars' Repository. It has been accepted for inclusion in Master's Theses and Capstones by an authorized administrator of University of New Hampshire Scholars' Repository. For more information, please contact Scholarly.Communication@unh.edu.

DEEP OCEAN DELIVERY SYSTEM

BY

CARIN CAMPBELL

B.S. Mechanical Engineering, University of New Hampshire, 2009

THESIS

Submitted to the University of New Hampshire

in Partial Fulfillment of

the Requirements for the Degree of

Master of Science

in

Mechanical Engineering

December, 2010

UMI Number: 1489972

All rights reserved

INFORMATION TO ALL USERS

The quality of this reproduction is dependent upon the quality of the copy submitted.

In the unlikely event that the author did not send a complete manuscript and there are missing pages, these will be noted. Also, if material had to be removed, a note will indicate the deletion.



UMI 1489972

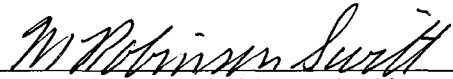
Copyright 2011 by ProQuest LLC.

All rights reserved. This edition of the work is protected against unauthorized copying under Title 17, United States Code.

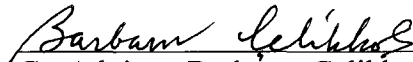


ProQuest LLC
789 East Eisenhower Parkway
P.O. Box 1346
Ann Arbor, MI 48106-1346

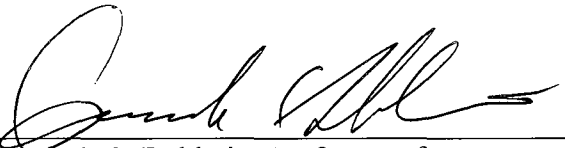
This thesis has been examined and approved.



Co-Advisor, M. Robinson Swift, Professor
of Mechanical and Ocean Engineering



Co-Advisor, Barbaros Celikkol, Professor of
Mechanical Engineering



Kenneth C. Baldwin, Professor of
Mechanical and Ocean Engineering

December 10, 2010

Date

ACKNOWLEDGMENTS

I would like to thank the following people who have contributed to this project and helped me along the way: To my thesis committee: Professor Rob Swift, Professor Barbaros Celikkol, and Professor Ken Baldwin for their support and guidance, both technical and otherwise. To Professor Igor Tsukrov for introducing me to the project and his advice regarding graduate school. To Jud DeCew for the countless hours that he put into the project and the encouragement he offered along the way. To Paul Lavoie for his design insight and impeccable craftsmanship. To Ryan Despins and the Ocean Engineering graduate students for keeping me company and making the work day that much more enjoyable. To the divers, deckhands, and boat captain for making the field testing a success. To Michael Chambers and Win Watson for all their help with the HTI acoustic tracking system. To my friends and family for standing by me. And last, but certainly not least, to Rob Nation, Jeff Reuter, Bill Terry, Jessica Murray, and Tim Camitta from BAE Systems for the funding support and all of their hard work.

TABLE OF CONTENTS

ACKNOWLEDGMENTS	iii
LIST OF TABLES	vii
LIST OF FIGURES	viii
ABSTRACT	x
INTRODUCTION	1
Previous Work.....	1
Goals.....	2
Approach	2
CHAPTER I: DESIGN CRITERIA.....	5
CHAPTER II: GENERAL CONFIGURATION	6
CHAPTER III: PRESSURE PROTECTION.....	8
<u>Housing Shapes</u>	8
Theory for Spherical and Cylindrical Cases.....	8
Results for Specific Materials	11
Pressure Tolerant Batteries.....	17
CHAPTER IV: CONCEPTUAL FULL SCALE DESIGN	19
CHAPTER V: HORIZONTAL DISPLACEMENT OF TRAJECTORY	20
Theory	20
Results for Prescribed Profile.....	22
WOCE Currents	23
CHAPTER VI: LANDING.....	28
Sediment Impact.....	28

Seabed Penetration	29
Maximum Seafloor Impact Velocity	33
Results	33
Drogue Deceleration	38
CHAPTER VII: PHYSICAL MODEL TANK TESTING	41
Froude-Scaled Model	41
Model Construction.....	42
Test Procedures	44
Trajectory Test Results.....	45
Drogue Tests	47
CHAPTER VIII: OPEN OCEAN TESTING	51
Conceptual Design of Large Scale Model	51
Tracking Methods	52
Accelerometers	53
Acoustic Tracking	57
Visual Tracking	63
Final Large Scale Model Design and Construction.....	63
Field Test.....	67
<u>Vessel, Equipment and Location</u>	69
<u>Test Procedures</u>	76
Test Results	82
CHAPTER IX: CONCLUSIONS.....	87
LIST OF REFERENCES.....	88

APPENDICES	90
APPENDIX A: SEDIMENT INTERACTIONS.....	91
APPENDIX B: HTI TANK TESTING RESULTS.....	101

LIST OF TABLES

Table 1: Pressure vessel approach check	11
Table 2: Material properties.....	13
Table 3: Single pressure vessel configurations.....	14
Table 4: Trajectory characteristics for selected pressure vessel configurations.....	15
Table 5: Pressure vessel combinations	16
Table 6: Free fall characteristics for two selected shapes.....	23
Table 7: Two stage drogue deployment.....	39
Table 8: Three stage drogue deployment.....	40
Table 9: Small scale model characteristics	42
Table 10: Small scale model test configurations	45
Table 11: Possible large model scales and model characteristics.....	51
Table 12: Scaled physical characteristics for the open ocean model.....	64
Table 13: Weight of each concrete cylinder	65
Table 14: Site evaluation current measurements	80
Table 15: Field test results	83
Table 16: Scaled field test results	85

LIST OF FIGURES

Figure 1: Parameters in the iterative design cycle	3
Figure 2: Current profile specified as part of the design criteria	22
Figure 3: Probability distribution of the depth averaged currents at buoy	25
Figure 4: Probability distribution of the depth averaged currents at buoy	25
Figure 5: Probability distribution of the depth averaged currents at buoy	26
Figure 6: Current magnitude in the average direction at buoy ACM6	26
Figure 7: Current magnitude in the average direction at buoy PCM6.....	27
Figure 8: Current magnitude in the average direction at buoy ICM7.....	27
Figure 9: Distribution of deep ocean sediments (Bearman 1989)	29
Figure 10: Static penetration for a side impact in pelagic clay.....	34
Figure 11: Static penetration for a head-on impact in pelagic clay	35
Figure 12: Dynamic penetration depth for a side impact in pelagic clay	36
Figure 13: Deceleration for a side impact in pelagic clay	36
Figure 14: Dynamic penetration depth for a head on impact in pelagic clay	37
Figure 15: Deceleration for a head on impact in pelagic clay	37
Figure 16: Drogue diameter as a function of impact velocity	39
Figure 17: The small scale model assembled (left) and disassembled (right).....	43
Figure 18: Four fin shapes for the small scale model	44
Figure 19: Small scale model with the drogue.....	48
Figure 20: Small scale model with the drogue pack behind it.....	49
Figure 21: Wave Rider accelerometer data before separation into individual tests	54
Figure 22: Wave Rider accelerometer results in the negative direction	55

Figure 23: Wave Rider results in the positive direction	55
Figure 24: Motion Pak results in the negative direction	56
Figure 25: Motion Pak results in the positive direction.....	56
Figure 26: HTI evaluation results from the UNH engineering tank	59
Figure 27: HTI evaluation results from the UNH engineering tank (top view).....	59
Figure 28: Schematic of the HTI pier test set-up	60
Figure 29: Results from the HTI pier testing (top view)	61
Figure 30: Results from the HTI pier testing (side view).....	62
Figure 31: Cross-sectional view of the open ocean model	63
Figure 32: Large scale model center of gravity location verification.....	66
Figure 33: Large scale model center of gravity location	67
Figure 34: Schematic of the field test plan	68
Figure 35: Test platform with wood drop frame.....	70
Figure 36: Bottom frame.....	71
Figure 37: HDPE pipe fuser.....	72
Figure 38: Mount for the underwater cameras and lights.....	73
Figure 39: Electronic test equipment set-up	75
Figure 40: Portsmouth Harbor test site (NOAA nautical chart # 13282)	76
Figure 41: Bottom sampler	77
Figure 42: Still capture from the bottom inspection at the 50 foot test location	78
Figure 43: Exact test site in the mooring field.....	79
Figure 44: Average current profiles for each drop test.....	84
Figure 45: ADCP magnitude and direction data.....	86

ABSTRACT

DEEP OCEAN DELIVERY SYSTEM

by

Carin Campbell

University of New Hampshire, December, 2010

The goal of this project was to explore the design and deployment of a deep ocean delivery system to the seafloor. The overall system configuration included a cylindrical shell, a hemisphere nose cone, pressure tolerant batteries, and a pressure vessel to house the electronics. As part of the design specifications, the system was to land within a 100 meter target radius directly below the location where the system entered the water. An approach was developed to determine the horizontal displacement for a given current profile and the system's interactions with the seafloor. The horizontal displacement was investigated for a variety of current profiles from the World Ocean Circulation Experiment. The influence of the center of gravity location, fins, and a drogue were examined by testing a small scale model in the UNH engineering tank and a large scale model in field experiments.

INTRODUCTION

The main focus of this project was the design of a delivery system to deploy in the deep ocean. The system was intended to be dropped at the surface of the ocean, sink up to 5000 meters through the water column, and land on the bottom within a 100 meter radius of the location directly below water entry. As the system descended through the water column, it was carried away from the bottom target by ocean currents. Because the hydrostatic pressure 5000 meters below the surface of the water is so high, the electronics and their power supply required pressure protection. The overall size and shape of the system also had to be determined to account for these currents and meet the landing location requirements.

Previous Work

While this project presented many challenges, a lot of work had already been done on related topics. The formulation for the stresses in thin and thick wall external pressure vessels had been thoroughly documented and is available for a variety of loading cases (for example, Young 1989). The World Ocean Circulation Experiment (WOCE) recorded extensive worldwide ocean measurements between 1990 and 1998, including ocean currents. Many of these current data sets span over a year and provided a valuable source from which current profiles were extracted (WOCE 2002). Studies that explored the relationship between the center of gravity location and the orientation with which cylindrical objects fell had already been completed (Chu et al. 2002). Principles from instruments that are currently used were adopted to achieve the project objectives. For example, expendable bathythermographs (XBTs) are designed to record a temperature

profile as it falls through the water column. These devices are able to travel straight down by employing fins on the tail that cause the device to spin as it falls (Green 1984). All of these previous works were used to reach the system goals.

Goals

The overall objective of this project was to design a delivery system for deep ocean use and understand how it behaved as it sank to the seafloor. This included:

1. Developing constraints on an overall system configuration,
2. Investigating deployment scenarios including system trajectory, velocity and landing position,
3. Determining the sediment and structure interactions and response, and
4. Verifying the analytical results with scaled model testing.

Each of these tasks was achieved by understanding the theory behind the processes being investigated, carrying out preliminary calculations to quantify the problem and indentifying important design parameters.

Approach

To accomplish each objective, a combination of analytical, numerical, statistical and physical models was used. Because the goals of the project were interrelated, an iterative approach was required. A significant portion of the work on the project focused on the relationships between these interconnected parameters which are shown in Figure 1.

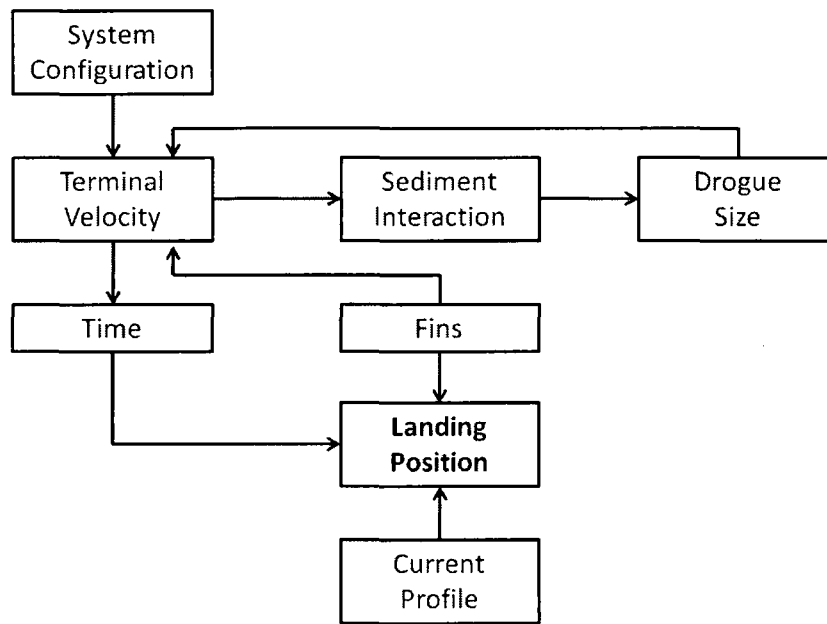


Figure 1: Parameters in the iterative design cycle

The general configuration of the system, including the size, shape, and mass distribution, directly affected its terminal velocity as it fell through the water column and, therefore, the time taken to reach the seafloor. These factors along with a given current profile resulted in a landing position, different from the bottom target. Knowing the terminal velocity and likely sediment types, the interactions with the seafloor were determined. Since the initial terminal velocity resulted in too much penetration into the sediments and excessive deceleration forces on the delivery system, a drogue was sized, which in turn altered the terminal velocity and ultimately the landing position. To be certain the system consistently landed within a desired range of the bottom target, fins were incorporated into the design. While the fins directly affected the angle with which the system fell, increasing the proximity of the landing location with the desired target, the additional drag also increased the time taken to reach the seafloor, allowing the current to carry the system further away. Understanding how all these parameters were related was vital to the development of the delivery system.

When determining the size, shape, and mass distribution of the system, the electronics and their power supply played a large role. Because the electrical components required pressure protection, they contained most of the mass and volume of the system. After resolving the pressure vessel needs, a method was developed to calculate the horizontal displacement of the system as it fell through the water column. This approach assumed that the package moved with the current, rather than experiencing a drag force from the current, as a worst case scenario. The theory and calculations were verified by testing a small scale physical model in the controlled environment of the UNH engineering tank. Taking into account new information from the small scale testing, a large scale model was constructed for testing in open ocean conditions.

CHAPTER I

DESIGN CRITERIA

A set of constraints was established to define the operating environment and design boundaries for the delivery system. Two primary constraints drove the system evolution. The weight in air was limited to 8000 lbf and the system had to arrive within a 100 meters radius target area, directly below its initial surface location in water up to 5000 meters deep. Initially the analysis was carried out with the following maximum current profile:

$$\text{Current}(in\ knots) = 0.3 + \frac{200}{\text{Depth}(in\ meters) + 100} \quad (1)$$

Later the system was subjected to actual measured current profiles.

Additional criteria placed constraints on the size of the device. The entire system was not to exceed 22.2 m³, with initial desired dimensions of no more than 3.56 meters long, 2.64 meters wide, and 2.36 meters high. The volumes for the pressure protected portions were broken down into 1.2 m³ for the power supply and 0.25m³ for the electronics. Lastly, the system was not to experience a shock load over 40 g's during deployment.

CHAPTER II

GENERAL CONFIGURATION

Ideally, systems deployed in the deep ocean have few, if any, moving parts. This focus towards simplicity limits malfunctions at depth. To satisfy the desire for a simple system, yet limit its horizontal movement, one solution was to allow the payload to free fall through the water column without the need for a guidance system or active controls.

In marine applications involving electronics, protecting those electronics and their power source is vital. The simplest way is to place all of the equipment inside a single pressure vessel with watertight connections through the pressure vessel wall for any parts that needs to be in the water. Since the pressure vessels can be very heavy to survive in deep water, another option is to place the electronics in a smaller pressure vessel and use pressure tolerant batteries.

Since the drag force is proportional to the cross-sectional area and related to the shape through the coefficient of drag, both the size and shape have a large effect on the system's behavior in the water. Decreasing the drag force would allow the system to fall more quickly through the water, in effect minimizing the horizontal movement away from the initial drop location. A decrease in drag force can be achieved by limiting the cross-sectional area and by choosing a streamline shape with a smaller coefficient of drag. In this case, the minimum cross-sectional area was defined by the size of the components within the system. For this reason, a cylindrical, free-flooding shell with a hemispherical nose was investigated.

Many systems that interact with the seafloor also aim to minimize that impact. Crashing into the seafloor not only exposes the system to the possibility of significant embedment into the sediment, but also to excessive shock loads. Either of these conditions could lead to poor system performance or a complete failure to operate. If the delivery system were allowed to impact the sediment at its terminal velocity, both embedment and shock loads would be of major concern. To prevent any unnecessary damage, the system can be slowed down as it reaches the bottom, which can be achieved by deploying a drogue.

CHAPTER III

PRESSURE PROTECTION

Housing Shapes

Before determining the approximate free fall characteristics of the system, a pressure vessel had to be sized to house the critical components which cannot operate in water under high pressure. Spherical and cylindrical pressure vessels were analyzed due to their stability under large external pressures. Both shapes were examined for yielding and elastic stability and sized for a variety of different materials and safety factors. Because the volume of sensitive equipment, including the electronics and power source, was specified to be 1.46 m³, the pressure vessels were sized for an internal volume of 2.0 m³ to account for unused space in packing the hardware.

Theory for Spherical and Cylindrical Cases

To determine the necessary pressure vessel geometry, the material yield strength, including a safety factor, was compared to the maximum stresses in the vessels when subjected to the design pressure. Radial and tangential stresses are present in a spherical pressure vessel. It can be shown that the larger of these two stresses is the tangential stress. This stress changes through the pressure vessel thickness and is greatest at the inside wall. The tangential stress is given by (see, for example Young 1989):

$$\sigma_t = \frac{p_o r_o^3 (2r_i^3 + r_i^3) - p_i r_i^3 (2r_i^3 + r_o^3)}{2r^3 (r_i^3 - r_o^3)} \quad (2)$$

where p_o is the external pressure, p_i is the internal pressure, r_o is the outside radius, r_i is the inside radius, and r is the radial distance where the stress is being computed. The external pressure for these calculations is given by:

$$p_o = \rho g d \quad (3)$$

where ρ is the density of salt water (1025 kg/m^3), g is gravity (9.81 m/s^2), and d is the water depth. At a depth of 5000 meters, the external pressure is 7290 psi. For an internal volume of 2.0 m^3 , the inside radius of a sphere is 30.8 inches. Knowing the external and internal pressures, inside radius, and maximum allowable stress, the outside radius of the pressure vessel, and therefore the wall thickness, can be found.

The elastic stability of each housing was also examined to ensure that the pressure vessels would not collapse. Instability is described by a critical pressure above which the walls of the pressure vessel will buckle. For a sphere, this critical pressure is provided by (Young 1989) as:

$$p_{cr} = \frac{2Eh^2}{r_o^2 \sqrt{3(1-\nu^2)}} \quad (4)$$

where E is the modulus of elasticity, ν is Poisson's ratio, h is the wall thickness, and r_o is the outside radius. If the critical pressure, including a safety factor, is larger than the external pressure, then the pressure vessel will fail by yielding and the computed wall thickness is acceptable. If the critical pressure is smaller than the external pressure, a new wall thickness must be calculated to withstand failure due to instability.

The same procedure was carried out to analyze cylindrical pressure vessels with hemi-spherical end caps. These pressure vessels have radial, axial and hoop stresses. The largest stress in a cylinder is the hoop stress, which varies through the wall thickness and is largest at the inside wall. It is given by:

$$\sigma_h = \frac{r_i^2 p_i - r_o^2 p_o - r_i^2 r_o^2 \frac{p_o - p_i}{r^2}}{r_o^2 - r_i^2} \quad (5)$$

(see, for example Young 1989) where p_i is the internal pressure, p_o is the external pressure, r_i is the inside radius, r_o is the outside radius, and r is the radius where the stress is being calculated. When determining the inside radius and length of the cylinder, a ratio of 1:6 was used. The internal volume is equal to that of a cylinder of length 9.11 feet and a sphere of radius 18.2 inches.

There are two different methods by which a cylinder can fail due to instability, and in the process of checking for failure, both methods were considered. The first applies to the region near the center of the cylinder tube where the effects from the end caps are not felt. When considering a thin tube under uniform radial external pressure, the critical pressure is

$$p_{cr} = \frac{E}{4(1 - \nu^2)} \frac{h^3}{r_o^3} \quad (6)$$

(Young 1989). The other loading case is present near the ends of the cylinder where the end caps contribute to maintaining the circular cross-section. The cylinder is subjected to uniform external pressure in both the radial and axial directions. The critical pressure in this case is:

$$p_{cr}(n, t_r) = \frac{E t_r}{1 + \frac{1}{2} \left(\frac{\pi r_o}{n L_i} \right)^2} \left(\frac{1}{n^2 \left(1 + \left(\frac{n L_i}{\pi r_o} \right)^2 \right)^2} + \frac{n^2 h^2}{12 r_o^2 (1 - \nu^2)} \left(1 + \left(\frac{\pi r_o}{n L_i} \right)^2 \right)^2 \right) \quad (7)$$

where n is the number of lobes formed during failing, L_i is the length of the cylinder, and t_r is the ratio of wall thickness to radius. This equation produces a set of curves for the critical pressure, one for each value of n . When the equation is evaluated at a given ratio of wall thickness to radius, a set of critical pressures is produced. The lowest of these

values is used when examining failure. As with spherical pressure vessels, if either of the critical pressures, including a safety factor, is larger than the external pressure, the vessel will fail by yielding. If the external pressure is larger, a new wall thickness is computed.

These calculations were checked for consistency by comparing their results with specifications for glass spheres produced Teledyne Benthos (Flotation 2010). Table 1 shows the three sizes of glass spheres that are currently available and the calculations for a glass sphere of the same internal volume. The calculations were carried out with a safety factor of 2.1.

Table 1: Pressure vessel approach check

	Benthos 10"	Model 10"	Benthos 13"	Model 13"	Benthos 17"	Model 17"
Inside Diameter (in)	9.3	9.3	12	12	15.9	15.9
Outside Diameter (in)	10	10	13	12.65	17	16.76
Weight in Air (lbf)	9	8.4	20	12.6	39	29.3
Net Buoyancy (lbf)	10	11.1	23	26.7	56	62.1
Depth Rating (m)	9000	9000	6700	6700	6700	6700

Results for Specific Materials

Several materials were considered for the construction of the pressure vessel, including metals, ceramics and glass. These materials were selected based on their high yield strength, availability, cost or use in other high pressure, underwater applications. Each material and its properties appear in

Table 2.

Table 2: Material properties

#	Material	Yield Strength (psi)	Young's Modulus (ksi)	Poisson's Ratio	Density (lbm/in ³)
1	1020 steel	50,800	29,700	0.29	0.284
2	Titanium Ti-6Al-4V	120,000	16,000	0.31	0.162
3	Pyrex	210,000 (USC)	8,900	0.20	0.081
4	Alumina 96%	300,000 (USC)	47,000	0.23	0.134
5	Alumina 99.5%	380,000 (USC)	54,000	0.22	0.140
6	17 - 4 PH Stainless Steel	110,000	28,500	0.27	0.282

The wall thickness and weight were calculated for each material, shape and a range of safety factors. The weight in air and weight in water were also computed, including the contributions from other components in the system. Table 3 shows the results of these calculations.

Table 3: Single pressure vessel configurations

#	Shape	Material	Safety Factor	Outside Radius (in)	Wall Thickness (in)	Instability Pcr (ksi)	Instability Thickness (in)	Material Volume (ft ³)	Weight of Pressure Vessel (lbf)	Buoyancy of Pressure Vessel (lbf)	Net Weight (lbf)	Total Weight (lbf)
1S	Sphere	1020 steel	1	33.36	2.59	215.9	0.45	19.4	9.507	5.759	8.161	17.451
			2	37.12	6.35	524.5	0.63	53.4	26,199	7.936	22,677	34,144
			3	43.49	12.72	1021.3	0.78	128.7	63,175	12,757	54,831	71,120
2S	Sphere	Titanium Ti-6Al-4V	1	31.77	1.00	19.1	0.61	7.1	1.982	4.973	1.423	9.927
			2	32.91	2.13	40.9	0.87	15.7	4,406	5.527	3,293	12,351
			3	34.23	3.46	66.0	1.07	26.6	7,438	6,220	5,632	15,383
3S	Sphere	Pyrex	1	31.33	0.55	3.3	0.83	5.9	825	4,897	342	8,770
			2	31.92	1.15	6.8	1.19	8.5	1,194	5,065	542	9,138
			3	32.56	1.79	10.6	1.47	13.1	1,830	5,356	887	9,775
4S	Sphere	Alumina 96%	1	31.15	0.38	8.4	0.36	2.7	619	4,690	341	8,563
			2	31.56	0.79	17.3	0.51	5.6	1,286	4,875	824	9,231
			3	31.98	1.21	26.6	0.62	8.7	2,008	5,074	1,347	9,952
5S	Sphere	Alumina 99.5%	1	31.07	0.30	6.0	0.33	2.3	559	4,667	305	8,504
			2	31.39	0.61	12.2	0.47	4.3	1,043	4,795	661	8,988
			3	31.71	0.94	18.7	0.58	6.7	1,614	4,947	1,081	9,559
6S	Sphere	17 - 4 PH SS	1	31.86	1.09	40.2	0.47	7.8	3,799	5,018	3,194	11,743
			2	33.13	2.36	86.7	0.68	17.5	8,540	5,641	7,312	16,485
			3	34.63	3.86	141.2	0.88	30.0	14,625	6,440	12,598	22,569
1C	Cylinder	1020 steel	1	21.58	3.36	30.5	2.08	36.2	17,784	6,416	15,782	25,729
			2	27.91	9.69	169.8	3.39	126.9	62,290	10,981	55,722	70,234
			3	48.86	30.46	666.5	6.80	676.5	332,011	36,116	300,308	339,956
2C	Cylinder	Titanium Ti-6Al-4V	1	19.44	1.22	1.1	2.44	25.6	7,156	5,862	5,707	15,101
			2	20.94	2.72	4.9	3.18	34.2	9,570	6,310	7,674	17,515
			3	22.85	4.63	12.3	3.74	52.1	14,586	7,231	11,768	22,530
3C	Cylinder	Pyrex	1	18.89	0.67	0.1	3.13	33.5	4,690	6,275	2,829	12,635
			2	19.63	1.41	0.4	4.12	45.6	6,386	6,899	3,900	14,331
			3	20.48	2.26	1.0	4.88	55.3	7,741	7,394	4,760	15,685
4C	Cylinder	Alumina 96%	1	18.68	0.46	0.2	1.67	17.0	3,946	5,418	2,941	11,890
			2	19.17	0.96	0.8	2.15	22.4	5,175	5,696	3,893	13,120
			3	19.71	1.49	1.8	2.51	26.3	6,907	5,902	4,608	14,042
5C	Cylinder	Alumina 99.5%	1	18.58	0.36	0.1	1.59	16.2	3,909	5,372	2,951	11,854
			2	18.96	0.74	0.4	2.04	21.2	5,116	5,632	3,897	13,061
			3	19.37	1.15	1.0	2.38	24.9	6,909	5,827	4,606	13,964
6C	Cylinder	17 - 4 PH SS	1	19.56	1.34	2.5	1.99	20.5	9,985	5,598	8,800	17,929
			2	21.25	3.03	11.2	2.57	32.4	15,788	6,217	13,984	23,733
			3	23.47	5.25	28.7	3.01	60.2	29,351	7,646	26,119	37,296

The goal was to maintain a weight in air of or below 8,000 lbf for transportation. However, the weight in water had to be large enough that the assembly sank and reached the ocean floor within the 100 meter radius. Table 4 shows the descent characteristics for selected pressure vessel configurations.

Table 4: Trajectory characteristics for selected pressure vessel configurations

#	Shape	Material	Safety Factor	Terminal Velocity (m/s)	Descent Time (min)	Lateral Drift (m)
2S	Sphere	Titanium Ti-6Al-4V	2	8.1	10.33	145.8
			3	10.1	8.21	115.9
6S	Sphere	17 - 4 PH Stainless Steel	2	12.2	6.81	96.1
			3	15.7	5.30	74.8
2C	Cylinder	Titanium Ti-6Al-4V	2	16.5	5.04	71.1
			3	20.5	4.06	57.3
6C	Cylinder	17 - 4 PH Stainless Steel	2	23.9	3.48	49.2
			3	29.7	2.81	39.6

Finding a pressure vessel that met both requirements with the above materials was not possible. Those which met the requirement for weight in air would float on the ocean surface or land outside the 100 meter landing radius and those which were capable of sinking to the ocean floor were too heavy for air transportation. (Details of the lateral displacement by current calculations are given in Chapter V.)

Since a single pressure vessel could not provide the desired weight characteristics, several combinations of pressure vessels were investigated. These combinations included two or more housings with different shapes and materials; reducing the number of batteries was also explored. The glass was very low weight and would help maintain the in air weight. The metals would safely house the batteries in the event of any unexpected reactions and add the necessary ballast. The results of this analysis are presented in Table 5. Again, the pressure vessel combination that met the weight in air requirements would

float and the combinations that met the landing requirement were too heavy for transportation.

Table 5: Pressure vessel combinations

Description	Weight in Air (lbf)	Weight in Water (lbf)	Terminal Velocity (m/s)	Descent Time (min)	Lateral Drift (m)
1 SS Sphere, 2.0 m ³ , SF = 2, r _o = 33.131 in	16,484.7	7,312.4	11.9	7.0	98.5
2 SS Spheres, each enclosing 1.0 m ³ , SF = 2, r _o = 26.296 in	16,484.7	7,312.4	15.0	5.5	78.2
1 SS Cylinder, 2.0 m ³ , SF = 2, r _o = 21.25 in	23,732.5	13,983.9	25.8	3.2	45.7
2 SS Cylinders, 1.0 m ³ , SF = 2, r _o = 16.87 in	23,732.4	13,983.9	32.4	2.6	36.3
SS Cylinder enclosing batteries, 1.6 m ³ , Pyrex Sphere enclosing remaining volume, 0.4m ³ , SF = 2, r _o = 18.692	20,411.3	10,901.2	25.8	3.2	45.5
SS Cylinder w/ half the batteries, 0.8 m ³ , Pyrex Sphere enclosing electronics, 0.4m ³ , SF = 2, r _o = 18.692 in	13,521.1	6,470.9	19.9	4.2	59.1
Titanium Cylinder enclosing batteries, 1.6m ³ , Pyrex Sphere enclosing remaining volume, 0.4m ³ , SF = 2, r _o = 18.692	15,657.5	6,071.8	19.3	4.3	61.0
Titanium Cylinder w/ half the batteries, 0.8 m ³ , Pyrex Sphere enclosing electronics, 0.4m ³ , SF = 2, r _o = 18.692 in	10,725.0	3,634.3	14.9	5.6	78.8
4 Pyrex Spheres, arranged inline, 0.5m ³ , SF = 2, r _o = 20.135 in	9,138.2	541.7	5.3	15.6	219.9
4 Pyrex Spheres, arranged inline, 0.5m ³ , SF = 2, r _o = 20.135 in w/ enough ballast to bring in water weight to 2620 lbf	11,216.5	2,620.0	11.8	7.1	100.0

Note: SS stands for stainless steel and SF stands for safety factor.

Pressure Tolerant Batteries

Since a pressure vessel or combination of pressure vessels was not found that would both meet the requirements for weight and landing proximity, a new approach was developed. Since the batteries comprise most of the pressure and water sensitive material, the decision was made to investigate other energy storage technologies. Some AUVs and submersible watercraft utilize unpressurized batteries in an oil bath as their power source. Generally these underwater vehicles operate for a short time and return to the surface where their batteries can be taken out and recharged. Since this delivery system will remain at the bottom of the ocean and operate for an extended period of time, the particular batteries in the underwater vehicles are not suitable, but the technology behind them is very much still under development.

One company, which is heavily involved in the field, is Bluefin Robotics, a spin-off from MIT's Autonomous Underwater Vehicle Laboratory. They have developed a 1.5 kW battery which is composed of rechargeable lithium polymer cells in an oil-filled aluminum box and are currently working on an 8.8 kW battery. These batteries are pressure tolerant to 10,000 psi and the larger of the two weighs 173 lbf in air and 79 lbf in water (Bluefin 2010).

By replacing the previous batteries with enough Bluefin Smart batteries to achieve the same kW-h of energy and removing the need for a pressure vessel to house the batteries, the weight in air of the system can be significantly reduced. If the previous batteries were housed in a cylindrical stainless steel pressure vessel with a safety factor of 2, the weight in air of the batteries and housing alone would be 19,600 lbf; the Bluefin batteries would weigh 5,882 lbf. This would give an entire system weight of 9,750 lbf in

air and 3,094 lbf in water, which was light enough to transport, yet heavy enough to sink to the sea floor quickly. The in air weight was over the 8,000 lbf target weight, but deemed acceptable by the customer.

CHAPTER IV

CONCEPTUAL FULL SCALE DESIGN

Having determined the contents of the delivery system and their weight characteristics, a conceptual design was formalized. As mentioned in the previous section, the weight in air will be 9,750 lbf and the weight in water will be 3094 lbf. The pressure tolerant batteries will be stacked in the nose of the system since they are the heaviest components. Positioning the majority of the weight near the nose will give the system a more stable orientation as it falls. The effects of the center of gravity position were further explored during small scale testing.

The water and pressure sensitive electronics will be housed in four 17 inch diameter, spherical pressure vessels produced by Teledyne Benthos. These are the same glass spheres that were used to check the pressure vessel calculations in the previous section. Positioning the four glass spheres in-plane dictated that the system could have a minimum diameter of 42 inches. The shape of the system was developed while investigating the horizontal movement during descent.

CHAPTER V

HORIZONTAL DISPLACEMENT OF TRAJECTORY

Theory

As part of the project specifications, the device must land within 100 meters of an intended target. To determine if this restriction could be met in a free fall scenario, an approach was developed knowing the system's size, shape, and weight and a specified current profile. This method was used to determine the lateral displacement for both a world average current profile and three ocean current measurement datasets.

Newton's second law dictates that the sum of weight in water and force due to drag is equal to the product of mass and the time rate of change of velocity as the system falls through the water column:

$$W - \frac{1}{2} C_D \rho_w A v^2 = m \frac{dv}{dt} \quad (8)$$

where W is the weight in water, C_D is the drag coefficient based on the shape, ρ_w is the density of sea water, A is the cross-sectional area, v is the velocity, and m is the mass of the system including an enclosed water. Once the velocity becomes constant, the system has reached its terminal velocity and Equation (8) can be rewritten as:

$$v_t = \sqrt{\frac{W}{\frac{1}{2} C_D \rho_w A}} \quad (9)$$

where v_t is the terminal velocity.

Since the system will experience some horizontal movement while it is accelerating towards the seafloor, the elapsed time and depth where the system reaches its

terminal velocity is of interest. By making a simple substitution, noting that $\frac{dv}{dt} = \frac{dv}{ds} \frac{ds}{dt} = \frac{dv}{ds} v$, and rearranging Equation (8), the time and depth when terminal velocity is reached can be, respectively, expressed as:

$$t_t = \int_0^{0.9v_t} \frac{m}{W - \frac{1}{2}\rho_w A C_D v^2} dv \quad (10)$$

$$s_t = \int_0^{0.9v_t} \frac{mv}{W - \frac{1}{2}\rho_w A C_D v^2} dv \quad (11)$$

In calculating both quantities the, bounds of integration are from 0 m/s at the surface to 90% of the terminal velocity. The upper bound cannot be the terminal velocity exactly because mathematically the solution to the integral would not converge to a numerical answer, but would instead be infinity.

To determine the horizontal movement, initially the specified current profile was used. Recall the current profile from Equation (1):

$$\text{Current}(in\ knots) = 0.3 + \frac{200}{\text{Depth}(in\ meters) + 100} \quad (1)$$

As a worst-case scenario, the system is assumed to travel with the current rather than feeling a drag force from it. As a result, the current in Equation (1) is actually the system's time rate of change of horizontal position, which can be integrated to obtain horizontal displacement. For both simplicity and a worst case scenario, the current is assumed be constant and equal to the current at the surface. Knowing the time that the system experiences this current, the horizontal movement can be found. Figure 2 shows a plot of this current profile. Note that the current at the surface is 2.3 knots, far higher than the current near the seafloor.

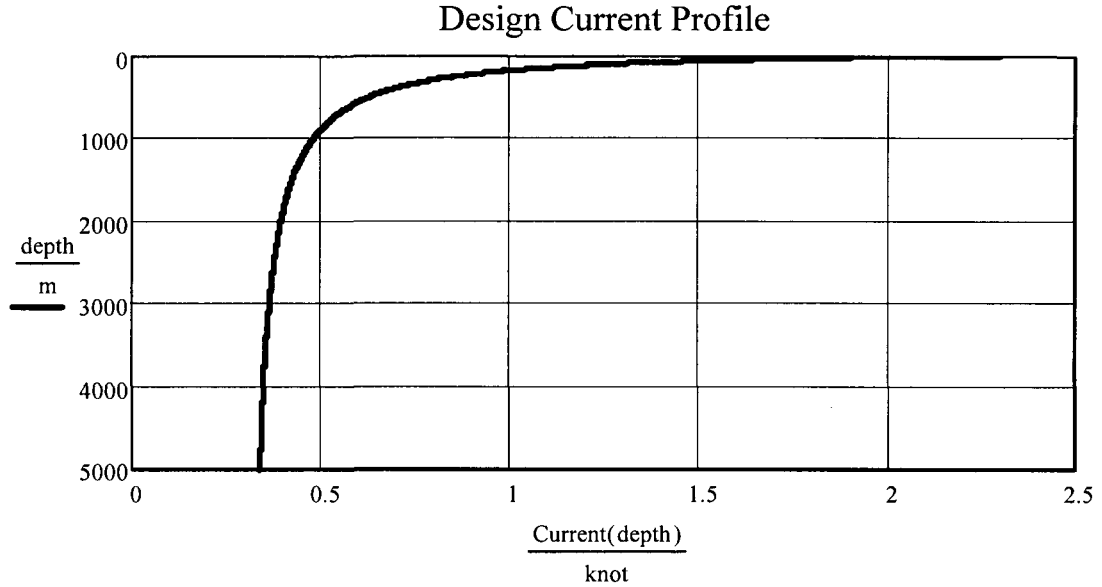


Figure 2: Current profile specified as part of the design criteria

Because the system travels at the known terminal velocity for the remainder of the descent, the integral

$$x = \int_{t_o}^{t_f} 0.3knot + \frac{200knot * m}{v_T t + 100m} dt \quad (12)$$

can be employed. The bounds for integration are the times when the system first reaches terminal velocity and the seafloor if it had been traveling at the terminal velocity for the entire descent. These times are used to ensure the substitution for depth is consistent. Adding the two portions of the decent gives the total time and horizontal displacement.

Results for Prescribed Profile

These calculations were initially carried out for three system configurations, each weighing 3,094 lbf in water with a cross-sectional area of 1385 in³, which corresponding to the minimum 42 inch diameter. The shapes included a rectangular prism, a blunt-end cylinder, and a hemispherical-nosed cylinder. For these calculations, the change in the

density with depth was assumed to be negligible. The results from these calculations appear in Table 6.

Table 6: Free fall characteristics for two selected shapes

Shape	Flat End Rectangular Prism	Flat End Cylinder	Hemispherical End Cylinder
Cross-Section	3.1 ft by 3.1 ft	42 inch diameter	42 inch diameter
Drag Coefficient*	1.5	0.8	0.2
Terminal Velocity	4.475 m/s	6.128 m/s	12.256 m/s
Time	18.64 min	13.63 min	6.86 min
Horizontal Displacement	264.4 m	191.1 m	101.1 m

*(Hoerner 1964)

From these results it is clear that a rounded cylinder is the best shape to satisfy the lateral travel specifications. Based on the terminal velocity, however, some means of slowing down the payload before reaching the sea floor may be required to avoid a shock load and burial in the ocean sediments upon impact.

WOCE Currents

Because the specified current profile was a world average, it could not represent a maximum current situation. For this reason the system's response was evaluated for a variety of actual deep water ocean current profiles. Specifically, the horizontal displacement as a result of the currents and the probability of system landing outside the 100 meter target radius was investigated. Data for three deep water sites was obtained from the WOCE current profiles:

- Buoy ACM6 – located in the North Atlantic
- Buoy ICM7 - located in the Western Arabian Sea
- Buoy PCM6 – located in the Northwest Pacific

The WOCE datasets gave water velocities at select depths in the water column, which varied by location. The information for each location was provided in a set of

files, with one file for every depth at which measurements were taken. The files included three components of velocity and the date and time they were recorded with at least 2 measurements per day for over a year (WOCE 2002).

For each location the following steps were taken to determine the probability that the delivery system would land outside the target radius.

- The data from all depth measurements was compiled into a matrix, matching east and north velocities by time step.
- The depth averaged velocity was calculated for both the east and north components.
- The probability distribution of vertically averaged velocity was computed.
- Since it was shown that the system would land within the target radius under the specified profile in Equation (1), the WOCE depth averaged velocities were compared to the specified profile's depth averaged velocity of 23.5 cm/s.
- The mean and standard deviation was calculated.
- The boundaries were adjusted to simulate dropping the payload up-current.
- The percentage of time steps for which the payload would land outside of 100 meters was found.

Figure 3 shows the probability distribution, with standard statistical parameters, of the east and north water velocity components for the North Atlantic buoy deployment. The solid red line represents the velocity limits for which the payload will land within target radius. The dotted blue line shows the same limits adjusted to simulate dropping the system upstream and allowing the dominant current to carry it to the desired location on the seafloor.

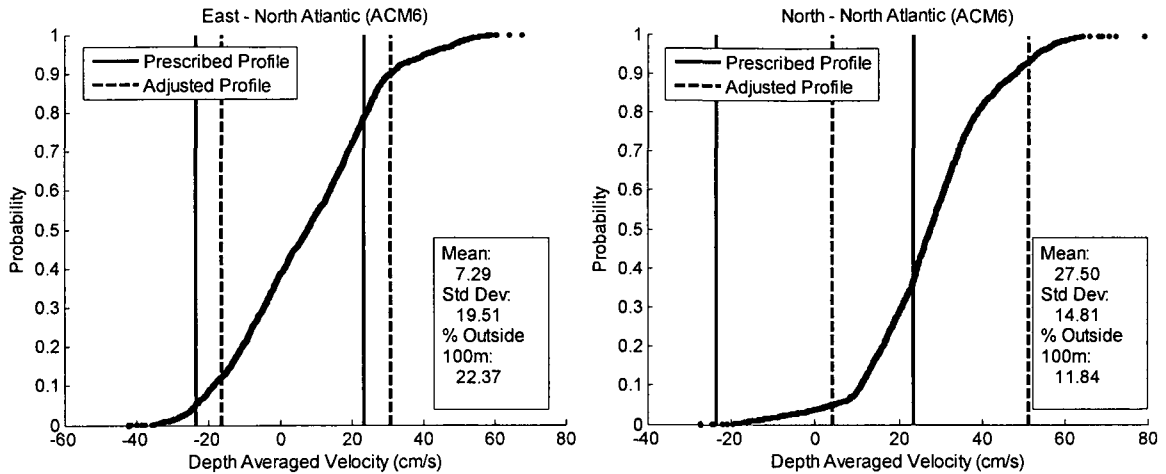


Figure 3: Probability distribution of the depth averaged currents at buoy ACM6

The payload was found to reach the landing target radius for a majority of the sites. The worst case occurred in the North Atlantic, where approximately 1 in 5 payload trajectories would land outside the target area. This was deemed acceptable, as it was found that the maximum displacement was less than 200 meters in these extreme cases. The results for the remaining sites are presented in the following figures:

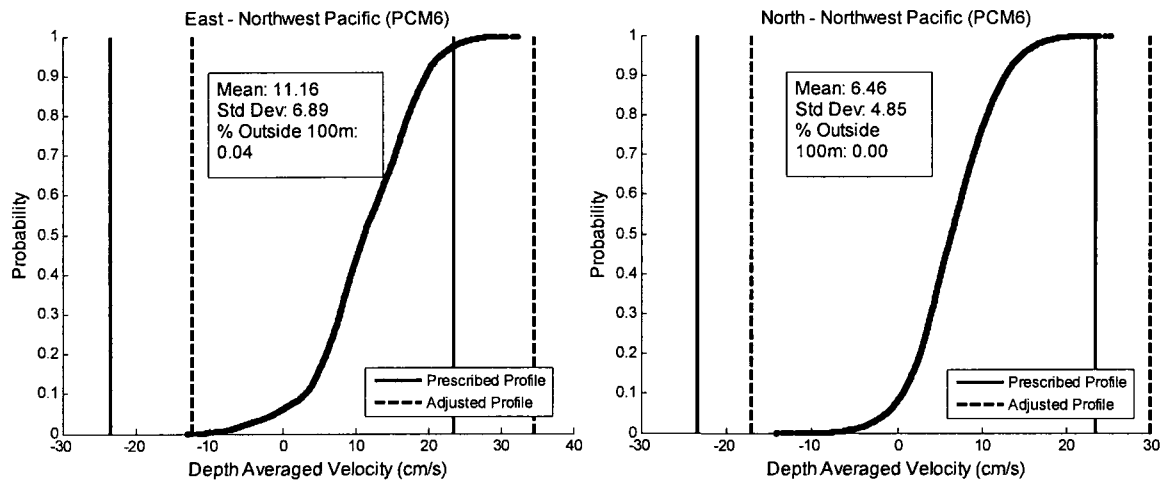


Figure 4: Probability distribution of the depth averaged currents at buoy PCM6

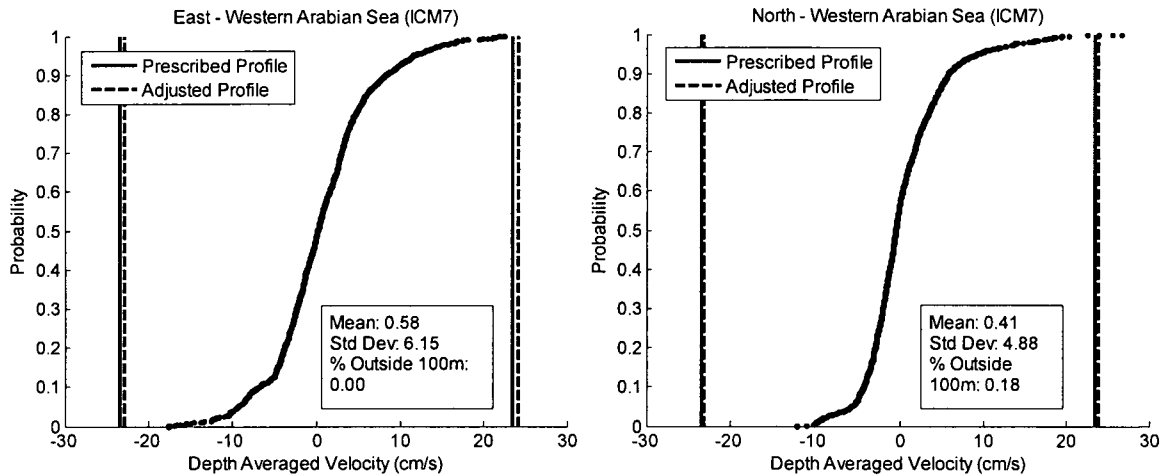


Figure 5: Probability distribution of the depth averaged currents at buoy ICM7

Since the previous analysis only looked at the two components of the current at each site, it was possible that the largest currents were in a different direction. For that reason the current magnitude in the dominant direction for each time step was also investigated. These results are shown in Figure 6 through Figure 8. For almost all cases, the system would land within the 100 meter target radius.

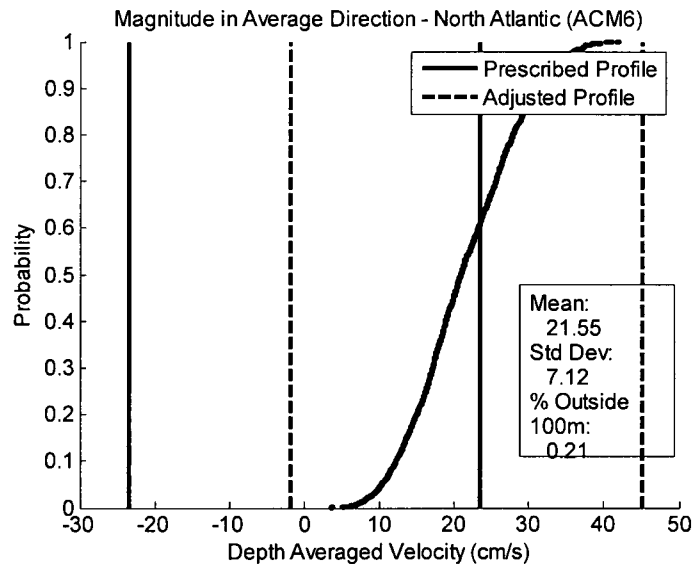


Figure 6: Current magnitude in the average direction at buoy ACM6

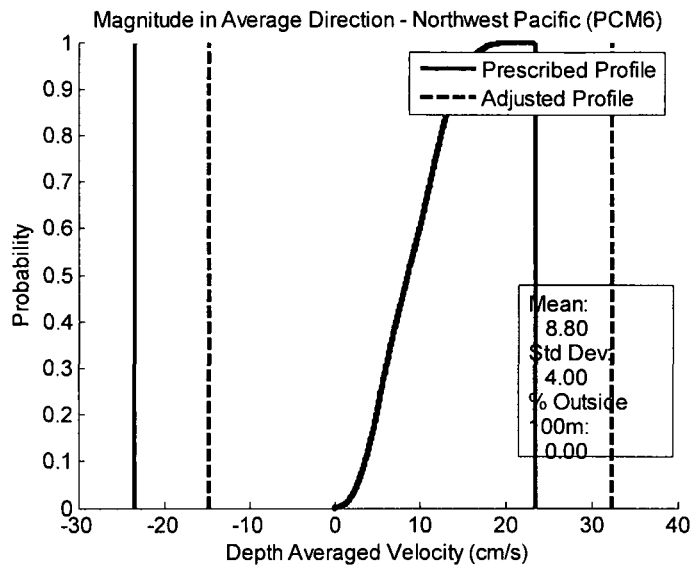


Figure 7: Current magnitude in the average direction at buoy PCM6

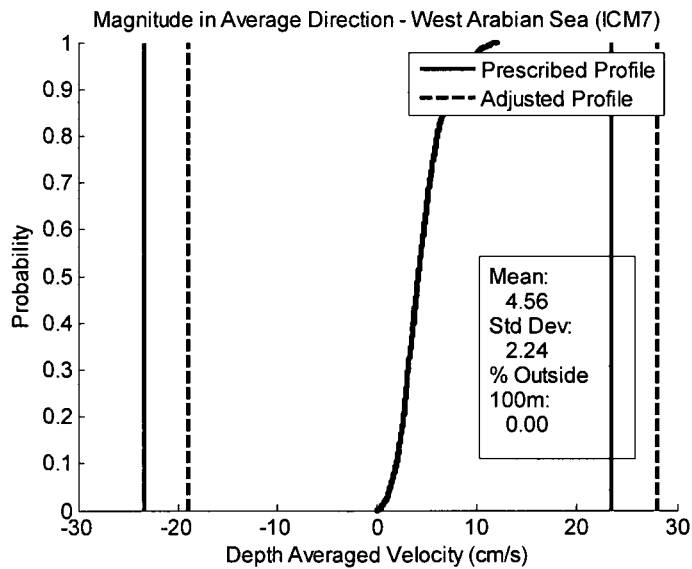


Figure 8: Current magnitude in the average direction at buoy ICM7

The system would land within the target radius for almost all 100% of the time for all three locations.

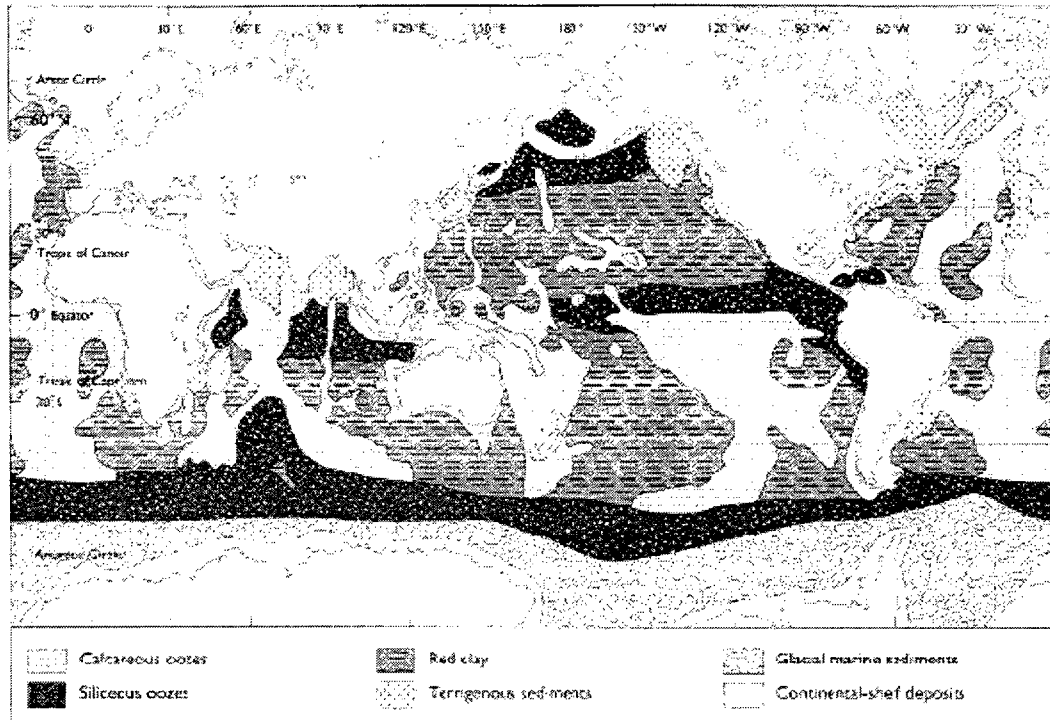
CHAPTER VI

LANDING

Sediment Impact

Author's note: The work in the following section is not that of the author's. It was performed and written by Jud DeCew, who has been also working on the project. The results in this section are a significant part of the decision making process, and are therefore included. The approach taken in this chapter follows those presented in the *Handbook for Marine Geotechnical Engineering* by Karl Rocker (1985).

After determining the system's behavior as it fell through the water column, the interactions with the sediments were explored. The deep water sediment was investigated and the approach to determine the bearing capacity of the sediment was developed. The instrumentation package will be deployed in depths between 3000 and 5000 meters. There are three dominate sediment types in this depth range: pelagic clays (red clay), calcareous oozes and siliceous oozes, shown in Figure 9. The Calcium Compensation Depth (CCD) is a driving factor behind which sediment will be present at these depths. If the system payload lands below the CCD, pelagic clays will be the dominant sediment type. If it is above the CCD, the sediment will most likely be calcareous or siliceous ooze. It is important to note that the CCD is different in various oceans (Berger and Winterer, 1974); therefore all three sediment types were investigated for this analysis.



(a) DEEP-SEA SEDIMENT DISTRIBUTION

Figure 9: Distribution of deep ocean sediments (Bearman 1989)

Seabed Penetration

It is important for the payload to have limited seafloor penetration, or rest on the seafloor, to insure proper deployment. The penetration depth is a function of the sediment properties, the system weight and configuration and its velocity at impact. Shock loads are also important and have to be monitored. According to Rocker (1985), analysis of a structure penetrating into the seafloor can be broken down into three categories: shallow static, deep static and dynamic penetration.

Shallow static penetration analysis requires the terminal velocity of the system to be less than 0.91 m/s and the ratio of penetration depth, z_{pen} , to minimum lateral dimension, B , to be less than 2.5. Note that the penetration depth is also referred as the

depth below the seafloor throughout this text. This analysis is similar to sediment bearing capacity analysis and is given by:

$$Q_{u_pen} = A_t(s_u N_c + \gamma_b z_{pen}) \quad (13)$$

where Q_{u_pen} is the sediment penetration bearing capacity, A_t is penetrator bearing surface area, s_u is the un-drained sediment shear strength, N_c is a dimensionless sediment bearing capacity factor, γ_b is the buoyant weight of the soil and z_{pen} is the penetration depth. The sediment shear strength is a function of the depth below the seafloor (typically increasing with depth). Therefore, the penetration depth is iteratively selected until the bearing load of the sediment equals the payload's in-water weight. In the event the ratio of the penetration depth to minimum lateral dimension is greater than 2.5, the static deep penetration analysis must be performed. Note that a shallow static penetration of the payload would be ideal for operational logistics.

For deep static penetration, the payload's terminal velocity must be less than 0.91 m/s and the ratio of penetration depth to minimum lateral dimension greater than 2.5. This analysis is similar to the shallow static calculations except that the side friction of the payload cannot be neglected, as shown by:

$$Q_{u_pen} = A_t(s_u N_c + \gamma_b z_{pen}) + A_s \alpha s_u \quad (14)$$

where A_s is the surface area in contact with the soil and α is an adhesion factor. A similar process is employed where the penetration depth is selected where the bearing load of the sediment matches the payload's in-water weight. Deep penetration should be avoided, if possible, to reduce or eliminate possible interferences between the sediment and the device.

If the terminal velocity cannot be controlled or the payload impacts the sediment at a speed greater than 0.91 m/s, then dynamic penetration analysis must take place. This iterative process takes into account the sediment bearing capacity, soil strain rate, remolding of the soil and fluid drag effects. This iterative procedure is required because many of the effects, such as side friction and hydraulic drag, are velocity dependant. Therefore, the approach examines the payloads penetration into the sediment in equal finite depth increments. The sum of the forces are calculated at each time step and used to determine the payloads velocity. Subsequent iterations utilize the output values as input, repeating the steps until the velocity of the unit reaches zero. The forces acting on the payload as it penetrates into the sediment can be shown to be:

$$F_i = F_{di} + W_{bi} - Q_{ni} - F_{si} - F_{hi} \quad (15)$$

where F_i is the net downward force exerted by the penetrator, F_{di} is any external driving force, W_{bi} is the penetrator buoyant weight, Q_{ni} is the payload nose bearing resistance, F_{si} is the side friction, F_{hi} is the fluid drag force, the i subscript is the depth increment. Note that Q_{ni} , F_{si} , and F_{hi} are velocity or depth dependant.

The payloads nose bearing resistance is described as:

$$Q_{ni} = s_{ui} s_{ei} N_{ti} A_t \quad (16)$$

where s_{ei} is the strain rate factor, N_{ti} is a dimensionless nose resistance factor, and A_t is the impact area of the payload. The nose resistance factor can be determined by:

$$N_{ti} = 5 \left[1 + 0.2 \left(\frac{B}{L} \right) \right] \left[1 + 0.2 \left(\frac{z_i}{B} \right) \right] \quad (17)$$

where B is the width of the payloads bearing surface, L is the length of the payloads bearing surface, z_i is the depth below the sediment. Note that N_{ti} must be less than or equal to 10. The strain rate factor is described by:

$$s_{\dot{\epsilon}i} = \frac{s'_{\dot{\epsilon}}}{1 + 1/\left[\frac{C_{\dot{\epsilon}}v_{i-1}}{s_{ui}D} + C_o\right]^{0.5}} \quad (18)$$

where $s'_{\dot{\epsilon}}$ is the maximum strain rate factor, $C_{\dot{\epsilon}}$ is the empirical strain rate coefficient, v_{i-1} is the velocity entering the i th layer, C_o is the empirical strain rate constant, D is the equivalent diameter of the payload. The side friction term can be shown to be:

$$F_{si} = \left[\frac{s_{ui}}{s_{ti}}\right] s_{\dot{\epsilon}i} A_s \quad (19)$$

where S_{ti} is the soil sensitivity, and A_s is the side area of the penetrator. The final force required for the dynamic penetration analysis is the fluid drag force:

$$F_{hi} = (0.5)C_d\rho A_t v_i^2 \quad (20)$$

where C_d is the fluid drag coefficient, ρ is the density of the fluid and v_i is the payloads velocity. At the point of impact, it is assumed that this force continues into the sediment, where the density term changes from that of seawater to the mass density of the soil. To solve this procedure, the forces are summed at each time step, and the resulting payloads velocity is obtained. The solution is complete when the velocity of the payload reaches zero.

Modifying Newton's second law, the following relationship can be obtained:

$$F_i = Mv_i \left(\frac{dv}{dz}\right) \quad (21)$$

where M is the payload mass and dv/dz is the instantaneous change in velocity. For incremental calculations, the dv/dz term can be changed to $(2\Delta v)/(2\Delta z)$, with the double increments used to minimize errors in the predicted penetration calculations. Solving for Δv ,

$$2\Delta v = \frac{2\Delta z}{M} \left(\frac{F_i}{v_i} \right) \quad (22)$$

The velocity at the next time step can be shown to be:

$$v_{i+1} = v_{i-1} + 2\Delta v_i \quad (23)$$

To initiate the approach, the water velocity at the first iteration needs to be determined.

This is approximated by

$$v_1 = v_0 + \left(\frac{1}{v_0} \right) \left[\frac{\Delta z}{M} \right] (F_{d1} + W_{b1} - Q_{n1} - F_{s1} - F_{h1}) \quad (24)$$

where v_0 is the impact velocity of the payload.

Maximum Seafloor Impact Velocity

Preliminary calculations were also performed to estimate the maximum payload impact velocity the system may have such that the resulting shock loads would be less than the designated 40g's. This calculation was performed independent of the sediment properties to provide insight into the maximum impact speed the system can sustain. The maximum velocity before impact can be found to be:

$$v_{bi} = (2a\Delta s)^{\frac{1}{2}} \quad (25)$$

where V_{bi} is the velocity at before impact, a is the acceleration of the payload and Δs is the distance over which the payload decelerates. If the acceleration is limited to -40g's and the penetrating depth is estimated to be 0.25 m, the resulting maximum landing velocity is 14 m/s. It is important to note that preliminary calculations showed that the terminal velocity needed to limit the horizontal drift of the device to 100m was 12 m/s.

Results

The static and dynamic penetration sediment bearing capacity and penetration analysis was performed for both a side and head-on impact. Figure 10 and Figure 11

show the sediment penetration depth for the static analysis in pelagic clay. The results for the other sediment types can be found in Appendix A. The penetration depth for the system is the intersection of the system weight (marked by the red star in the figure) and sediment bearing capacity (bearing load). Recall that this calculation is only valid when the impact velocity is less than 0.91 m/s.

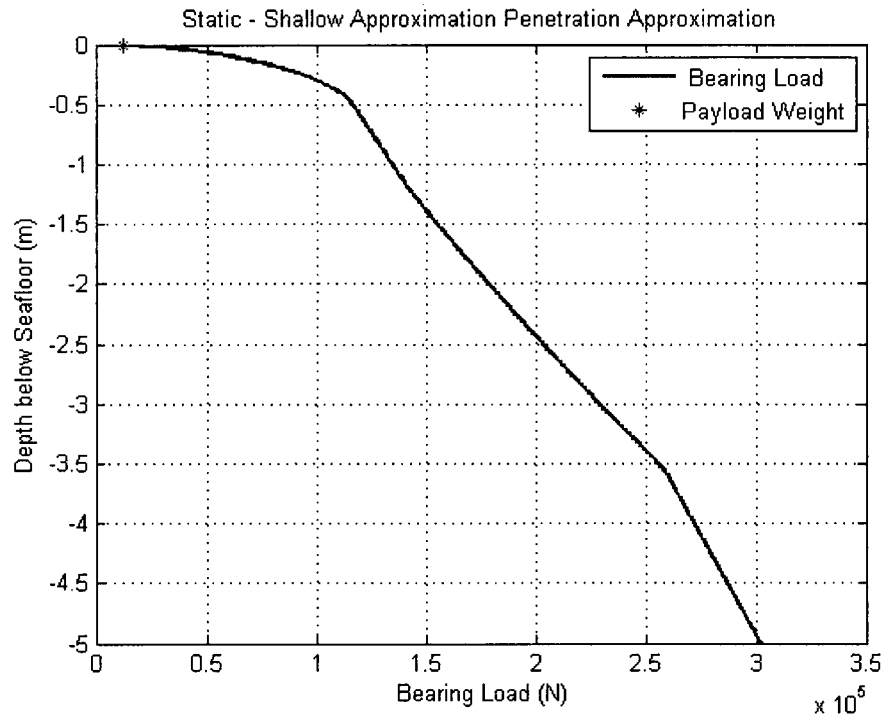


Figure 10: Static penetration for a side impact in pelagic clay

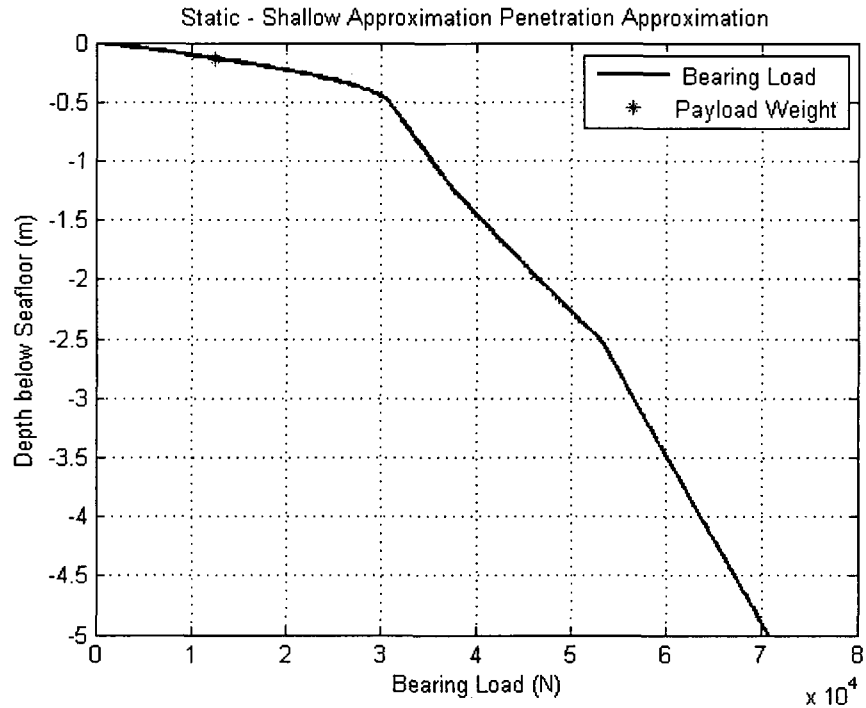


Figure 11: Static penetration for a head-on impact in pelagic clay

It can be seen that the side impact penetrates the seafloor sediment less than when impacting head on due to the increased impact surface area of the unit.

The dynamic penetration of the unit was also examined. The penetration depth of the payload for a side impact in pelagic clay is presented in Figure 12. Likewise, the linear acceleration of this unit was predicted, using Equation (25), to estimate the gravitation forces associated with the acceleration of the payload (Figure 13). This linear calculation provided preliminary information regarding individual component acceleration specifications. Recall that this analysis is valid for impact velocities greater than 0.91 m/s

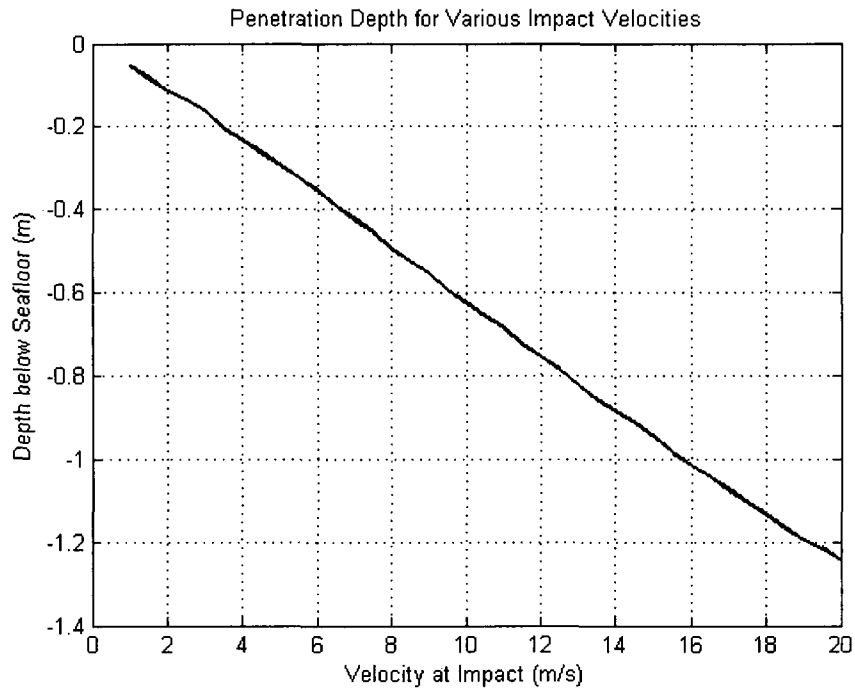


Figure 12: Dynamic penetration depth for a side impact in pelagic clay

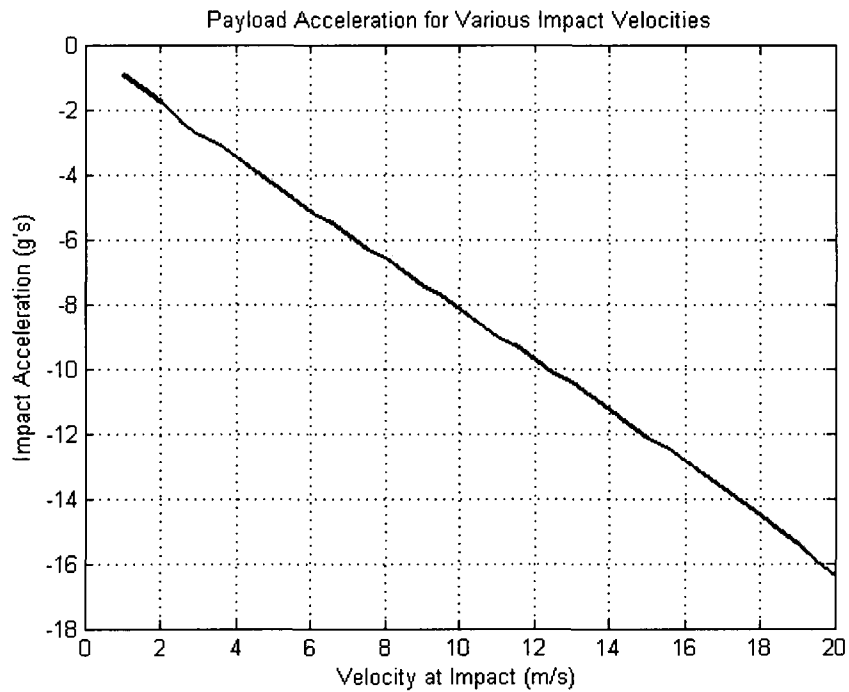


Figure 13: Deceleration for a side impact in pelagic clay

Similarly, the results from a head-on impact are shown in Figure 14 and Figure 15.

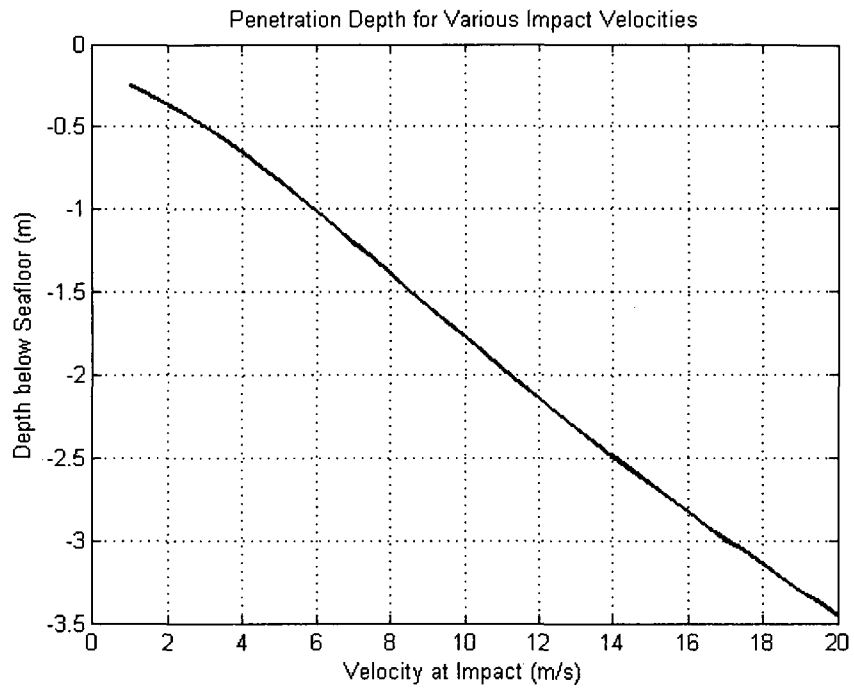


Figure 14: Dynamic penetration depth for a head on impact in pelagic clay

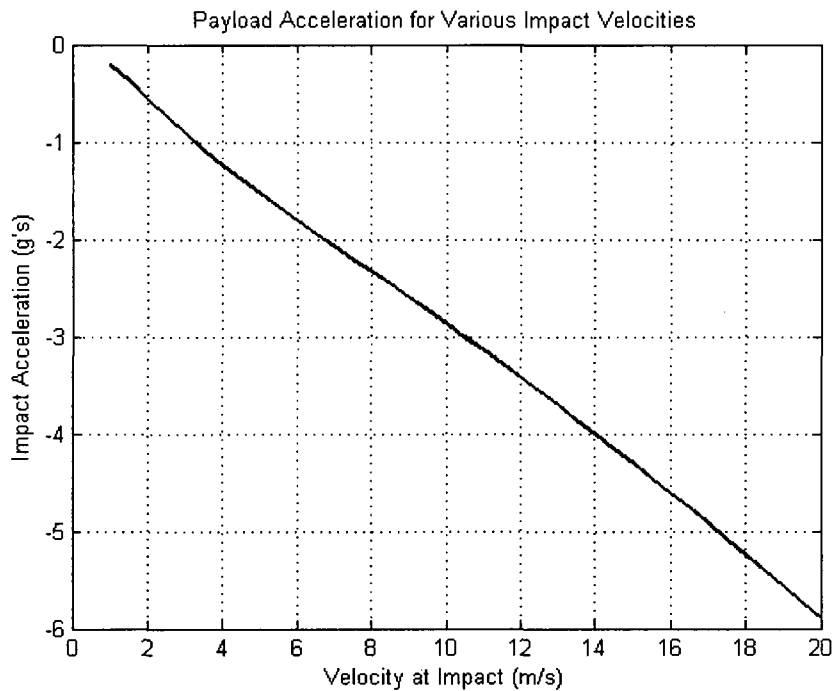


Figure 15: Deceleration for a head on impact in pelagic clay

If the system were allowed to free fall from the surface, it would impact the seafloor head-on at its terminal velocity of 12.26 m/s. The system would penetrate about 2.2 meters into the sediment and experience a deceleration just over 3.5 g's.

Drogue Deceleration

Based on the sediment interaction results, a method needed to be developed to reduce the velocity of the system before impact. Decreasing the terminal velocity could be achieved by increasing the projected area, drag coefficient, or both. The simplest method by which either of these objectives can be accomplished is deploying a drogue near the seafloor. An altimeter could be installed in the nose cone to trigger a release mechanism at a predetermined height above the sea floor.

When sizing the drogue, Equation (9) that was used for terminal velocity earlier applies. Since the drag from the drogue would be far greater than the drag from the system, only the drag from the drogue was considered. The drag coefficient for a hollow hemisphere open to the direction of fluid flow is 1.3 (Hoerner 1964). Figure 16 illustrates the relationship between the diameter of the drogue and the velocity with which the system would impact the sediment after deployment.

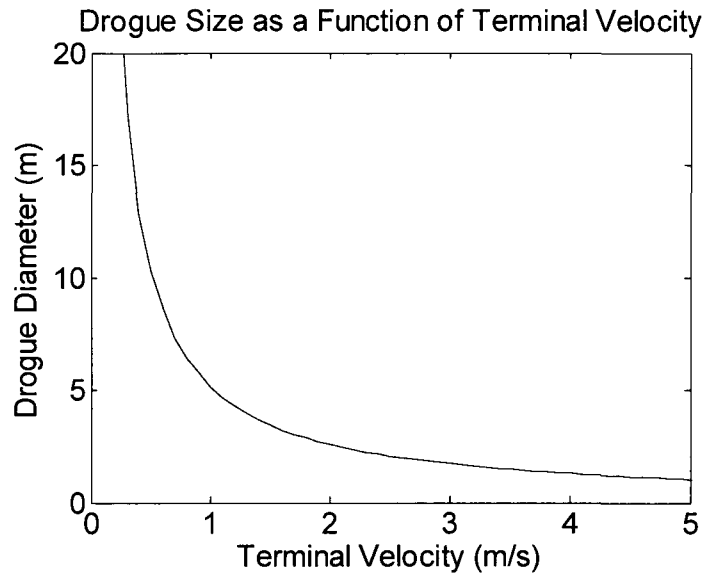


Figure 16: Drogue diameter as a function of impact velocity

The results from the sediment interaction analysis show that a lower terminal velocity will decrease both the penetration depth and the deceleration. For impact velocities under 1 m/s, the required drogue diameter increases exponentially. For this reason, an impact velocity of 1 m/s was chosen, which corresponds to a drogue that is 5.13 meters in diameter. If the drogue is assumed to open instantaneously, the system will experience a deceleration of 34.5 g's and a drag force of 465,000 lbf to be distributed among the drogue shroud lines. Since the shock from a single drogue was too high, a method was developed to slow the system in steps by deploying a series of drogues. The following tables show some of these scenarios:

Table 7: Two stage drogue deployment

	Drogue 1	Drogue2
Velocity (m/s)	3.5	1
Diameter (m)	1.47	5.13
Deceleration (g)	2.8	2.8
Drag Force (lbf)	37,900	37,900

Table 8: Three stage drogue deployment

	Drogue 1	Drogue 2	Drogue 3
Velocity (m/s)	5.3	2.3	1
Diameter (m)	0.96	2.22	5.13
Deceleration (g)	1.2	1.2	1.2
Drag Force (lbf)	16,400	16,400	16,400

Deploying the drogues in staged significantly reduces the shock load on the system and the tension in the shroud lines. During investigation into using drogues was carried out during small scale testing in the tank.

CHAPTER VII

PHYSICAL MODEL TANK TESTING

The analysis to this point has shown that the payload met the required weight constraints, descended through the water column while limiting the horizontal movement, and slowed to an acceptable speed before seafloor impact. However, this assumed that the system traveled “nose first” through the water column. The system orientation in the water column is primarily a function of the locations of the center of gravity (CG) and center of buoyancy (CB). Previous studies have shown that a separation distance between the CG and CB of 20% of the overall length is required for a flat ended cylinder to descend vertically (Chu et al. 2002).

The analyzed configuration, however, has a CG – CB separation distance of only 4.6% of the total length. To determine if the system will descend through the water column in the proper orientation, a physical model was constructed and tested in the UNH Ocean Engineering Laboratories 60 feet by 40 feet by 20 feet tank.

Froude-Scaled Model

When conducting a scaled test in a fluid, there are two primary characteristic numbers that can be matched: the Reynolds number and the Froude number. The number which is used depends on the forces involved. The Reynolds number is a ratio of the inertia forces to the viscous forces while the Froude number is related to the ratio of the inertia forces to the gravity forces. Since these tests involved an object falling through the water, the Froude number:

$$Fr = \frac{v}{\sqrt{gL}} \quad (26)$$

was more appropriate to use. If the Froude number is matched and the ratio of full-scale and model-scale lengths is used, the weight scales by the ratio cubed and terminal velocity scales by the square root of the ratio. For the small model, a length scale around 1/20 was desired and based on polyvinyl chloride (PVC) pipe sizes, an exact scale of 1/22.1 was chosen.

Table 9: Small scale model characteristics

	Full Scale	Small Scale
Length	12.2 ft	6.623 in
Diameter (in)	42	1.9
Weight in Water (lbf)	2797	0.26
Center of Gravity location (in)	57.6	2.6
Terminal Velocity (m/s)	11.65	2.48
Impact Velocity (m/s)	1	0.21
Drogue Diameter (ft)	4.88	0.22

Note: The full scale design which has been presented thus far is the final design. The small scale model was based on a previous iteration which was the working design at the time.

Model Construction

The exact scale for the small scale model was chosen based upon the available sizes of PVC pipe. PVC was a relatively inexpensive, readily available material that machined easily which made it an appropriate material to use for the model. A 1.5 inch PVC pipe has an outer diameter of 1.9 inches, which imposed the exact scale. The pipe was cut to length and four axial slots were machined into the tail end of the pipe to accept fins. A nose cone was machined from a PVC block into a hemisphere with a lip that was cemented into the end of the pipe. An end cap was also machined and fit snugly into the

other end of the pipe with an O-ring to prevent water from getting into the model. It was held in place with a small screw.

A threaded rod was attached to the center of the end cap, which was able to spin. A guide rod was attached to the nose cone inside the pipe. Small slots were cut into the washers that were used as ballast weight. The washers were placed around the threaded rod and were fixed to a threaded PVC disk, as seen in Figure 17.

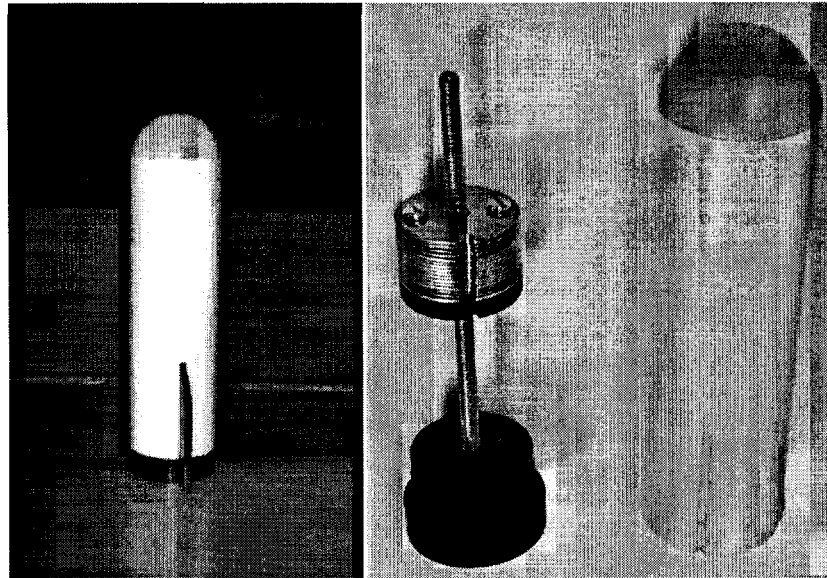


Figure 17: The small scale model assembled (left) and disassembled (right)

During assembly, the slot in the washers was lined up with the guide rod. When the center of the end cap was turned, the guide rod prevented the washers and the PVC disk from spinning and the washers moved along the length of the model. This feature provided for a way to adjust the center of gravity without unpacking and repacking the model.

In addition to the model, four sets of fins were made, all with the same surface area, from 1/8 inch PVC sheet. The first two sets were flat fins. One set was high aspect ratio fins measuring 1 inch by 1 inch; the other set had a low aspect ratio and measured 2

inches by $\frac{1}{2}$ inch. The last two sets had a high aspect ratio and were bent at 15° and 35° . These four shapes are shown in Figure 18.

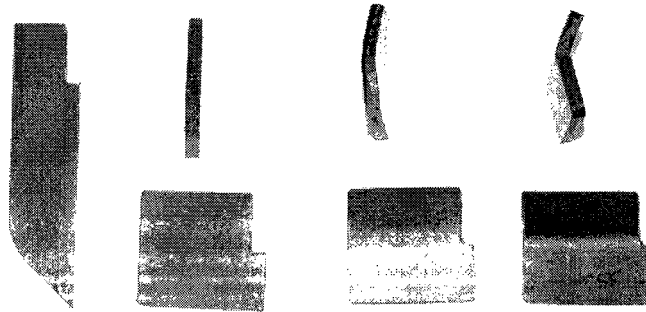


Figure 18: Four fin shapes for the small scale model

Test Procedures

The model was repeatedly dropped and observations were made regarding its orientation and trajectory in the water column. A frame-mounted target was placed on the bottom of the pool. Netting was stretched over a one meter by one meter plastic pipe frame, and a red rubber circle was affixed to the center of the net to represent the 100 meter target radius scaled down by the depth of the tank. Because the pool was 20 feet deep, the target radius was 4.8 inches. A second frame was held at the surface with strings tied to opposite corners, forming an 'x' and identifying the point directly above the target on the bottom of the pool.

For the first set of tests, the effect of the separation distance between the center of gravity and center of buoyancy was explored. Recall that the separation distance for the system was 4.6% of the overall length and previous research suggested that a distance of at least 20% was required for the model to fall vertically. Because a separation distance of 20% could not be achieved with the system components, the model was tested for distances of 4.6% and 10%.

Another set of tests was performed to evaluate the affect of fin shape on the model orientation and trajectory. Both sets of flat fins, high and low aspect ratio, were tested with 4.6% and 10% separation distances to determine which combination was most effective and which could meet the landing target requirement.

Lastly, tests were performed with the both sets of angled fins. Angled fins are used on other oceanographic instruments that are required to fall through the water vertically, such as expendable bathythermographs (XBTs). Previous studies on XBTs suggested that a rotational speed of 15 rps was sufficient to achieve the correct orientation, but did not comment on the center of gravity location (Green 1984). For this reason, the 15° and 35° fins were tested with a separation distance of 4.6%. Table 10 summarizes all the testing configurations.

Table 10: Small scale model test configurations

Test #	CG and CB Separation Distance (% of overall length)	Fins
1	4.6	None
2	10	None
3	4.6	Low aspect ratio, flat
4	10	Low aspect ratio, flat
5	4.6	High aspect ratio, flat
6	10	High aspect ratio, flat
7	4.6	High aspect ratio, with 35° bend
8	4.6	High aspect ratio, with 15° bend

Trajectory Test Results

For test number 1 the target net panel was suspended about 5 feet below the water's surface to ensure that the model would land on it since in these initial experiments trajectories were uncertain. The net was also used to retrieve the model after each drop and some tests were done releasing the model from a horizontal orientation.

For the first test, the model was dropped from a horizontal position, near the wall of the tank to allow the model to move horizontally the most while still landing on the net. The model traveled to the opposite side of the net panel, demonstrating that a 4.6% separation difference will not meet the horizontal displacement criteria.

Next, the center of gravity was moved to provide a 10% separation distance. The target net panel was placed on the bottom of the tank in one corner, and the top frame was held at the surface with the crossed strings showing the location directly over the target. The model landed on the net panel, but missed the red bull's-eye by about one radius. A 10% separation distance would not meet the target landing requirements either.

The system could not meet the landing target requirement by adjusting the center of gravity, so low aspect ratio fins were added. In test number 3 the trajectory was improved, but the results were not repeatable. The model landed within the bull's-eye for 40-50% of the drops. The center of gravity was moved for test number 4 which resulted in the model hitting the target area consistently, but with a center of gravity that would require redesigning the full scale system.

Since the landing radius target was still unable to be met, the low aspect ratio fins were replaced with the high aspect ratio fins. In test number 5, the model landed within the bull's-eye, with the current full scale center of gravity location, for each drop though some landed near the edge of the bull's-eye. The model also landed within the bull's-eye for test number 6. The high aspect ratio fins could successfully meet the horizontal displacement requirements.

To improve the landing position, bent fins were attached, causing the model to spin as it sank. In test number 7 the model landed in the center of the target repeatedly,

but the added projected area from the fins slowed the model down which could have adverse effects if currents were present. Fins with a lower projected area were used in test number 8 and the model still landed in the center of the target consistently. As a result, the most successful combination that did not require redesigning the full scale system had a center of gravity and center of buoyancy separated by a length equal 4.6% of the overall length and employed high aspect ratio fins bent at an angle of 15°.

Drogue Tests

A scaled drogue was also made to test with the small scale model. The goals of the drogue testing were to:

- explore how the drogue opens including how long it takes and what distance the model drops during that time,
- evaluate orientation and path stability with the drogue open,
- determine what length shroud lines would allow the drogue to fully open without tangling, and
- investigate the effects of a hole in the center of the drogue.

The diameter was 9.1 inches, scaled down from the 5.13 meter full scale drogue. The drogue was sewn together from eight panels of sport nylon into a hemispherical shell. Four twine shroud lines, each one drogue diameter long, were sewn into the bottom hem and tied to the fins. Previous studies showed that parachutes with a 3:1 ratio of shroud line length to drogue diameter open more fully than those with a 1:1 ratio, but because tangling in the lines was a concern, the testing started with shorter shroud lines as shown in Figure 19 (Scher & Gale 1949). Fishing line was tied to the center of the drogue to retrieve the model after each test.

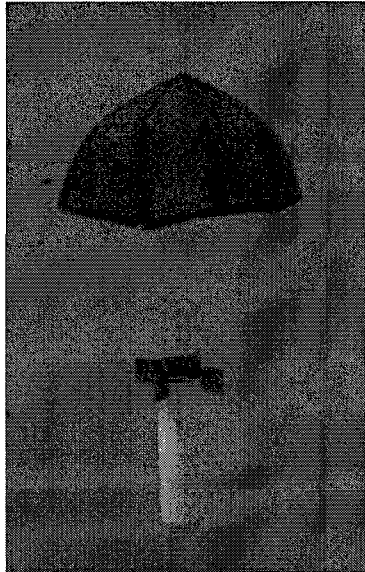


Figure 19: Small scale model with the drogue

For all of the small scale drogue tests, the center of gravity was set for a 4.6% separation distance and flat high aspect ratio fins were used since the bent fins would cause the drogue to also spin. (In the full scale model, a swivel would be used to eliminate this issue.)

For the first test the drogue was opened at the surface and the model and drogue sank to the bottom of the tank. Good stability was observed in that there was no oscillation and the path was smooth. The model, however, drifted to the same side for each of these tests. After inspecting the drogue, it was noted that one of the shroud lines was 1/8 of an inch shorter than the rest, which caused the model to drift in that direction. At a larger scale, this would not be an issue. The model took 36 seconds to reach the bottom of the tank, which resulted in a velocity of 0.17 m/s or 0.80 m/s full scale. Recall that the drogue was sized to reduce the speed of the full scale system to 1 m/s. This difference was at least partially due to only including the drag force from the drogue in the calculations. The model also contributed to the overall drag force, further slowing it

down. Additionally, the model operates at a lower Reynolds number, increasing the viscous affects.

The drogue was packed, held in place with an elastic band, and deployed underwater for the second test as shown in Figure 20.



Figure 20: Small scale model with the drogue pack behind it

The model was allowed to sink a short distance before the fishing line tied to the drogue was tugged, pulling it out from under the elastic. For each of these tests the drogue fully opened without tangling any of the shroud lines. It took about 2 seconds for the drogue to fully open after it was pulled from under the elastic, over which time the model dropped about 6-7 feet.

For the last set of drogue tests, a small hole was cut in the center of the drogue after observing that almost all commercially available drogues had this feature. The hole in the center of the drogue appeared to decrease drift, though not substantially. With a hole in the drogue, the model took 34 seconds to reach the bottom of the tank, which resulted in a terminal velocity of 0.18m/s, or 0.84 m/s for the full scale system.

Based on all of the tests, a drogue could successfully be deployed underwater, open fully, and slow the system to an acceptable impact velocity. A hole 1/8 of the

diameter in the center of the drogue improved the trajectory. Instead of four shroud lines, the full scale drogue and any subsequent scaled drogues will have eight shrouds, so the drogue better keeps its shape during descent.

CHAPTER VIII

OPEN OCEAN TESTING

After completing scaled tests with a small model in the controlled environment of a tank, the next step in testing was to build a larger model and observe its behavior in an uncontrolled environment which more closely resembles the actual operating conditions of the full scale design. Dropping the larger model in a marine setting showed how the model reacted to currents and allowed for further observation of the overall behavior.

Conceptual Design of Large Scale Model

The first step in formulating a conceptual design for the new model was to decide on a model scale. The three scales that were considered are shown in Table 11 with the model characteristics for each. A scale of 1/5 was chosen as a compromise between constructing a model whose weight could be managed out of water and whose size would accurately model interactions with the surroundings.

Table 11: Possible large model scales and model characteristics

Scale	Full scale	1/3	1/4	1/5
Dry Weight (lbf)	9750	361.1	152.3	78.0
Wet Weight (lbf)	3094	114.6	48.3	24.8
Diameter (in)	42	14.0	10.5	8.4
Length (ft)	15.7	5.23	3.93	3.14
Terminal Velocity (m/s)	12.26	7.08	6.13	5.48
CB (in)	96.12	32.04	24.03	19.22
CG (in)	73.56	24.52	18.39	14.71

Note: The CG and CB were measured from the base of the nose towards the rear of the model.

A decision also had to be made about whether or not to seal the model or allow it to free flood. The small scale model was easily sealed because it was tested in a maximum of 20 feet of water, where the hydrostatic pressure was relatively low. The large scale model, however, needed to be able to withstand the pressure in up to 100 feet of water, where the hydrostatic pressure would be 44 psi. Preventing water from entering the model at that pressure would have been more difficult, but controlling the center of buoyancy location and installing electronics in the future would be far easier. The decision was made to allow the model to free flood because construction would be much easier in addition to the model being able to tolerate some damage and still maintain reliable dynamic behavior.

Since the full scale model was going to be deployed in an ocean environment, it would need to survive any impact with the seafloor which could include a rocky bottom. Since impacting rock at the scaled terminal velocity could potentially damage the nose cone, a method needed to be determined to slow the model down. Like the full scale design and the small scale model, a drogue would be used.

Tracking Methods

The purpose of the open ocean testing was to determine how the model would react to actual operating conditions. A large portion of the evaluation was determining where the model landed in relation to a target area. To gather this information, a method to track the model and its trajectory through the water column needed to be developed. Three methods were explored: inertial tracking using accelerometers, acoustic tracking, and visual tracking.

Accelerometers

The depth of the model could easily be determined using accelerometers because of the large accelerations shortly after launch and after reaching the seafloor. However, measuring the displacement in the horizontal direction would be far more difficult given the slow movement over a short distance. Two accelerometers, Wave Rider and Motion Pak, were tested to determine if such a lateral movement could be accurately measured with accelerometers. These accelerometers are usually used on buoys to measure the buoy's motion response to waves.

The test set-up involved mounting each accelerometer on a rolling cart. The cart was pushed three feet along a single axis of the accelerometer over nine seconds to simulate the magnitude of lateral displacement expected in the open ocean tests. The Wave Rider accelerometer produced output files in 20 minute batches, and the Motion Pak accelerometer recorded in 6 minute batches which needed to be separated into the individual tests. Figure 21 shows an example of the data before it was separated.

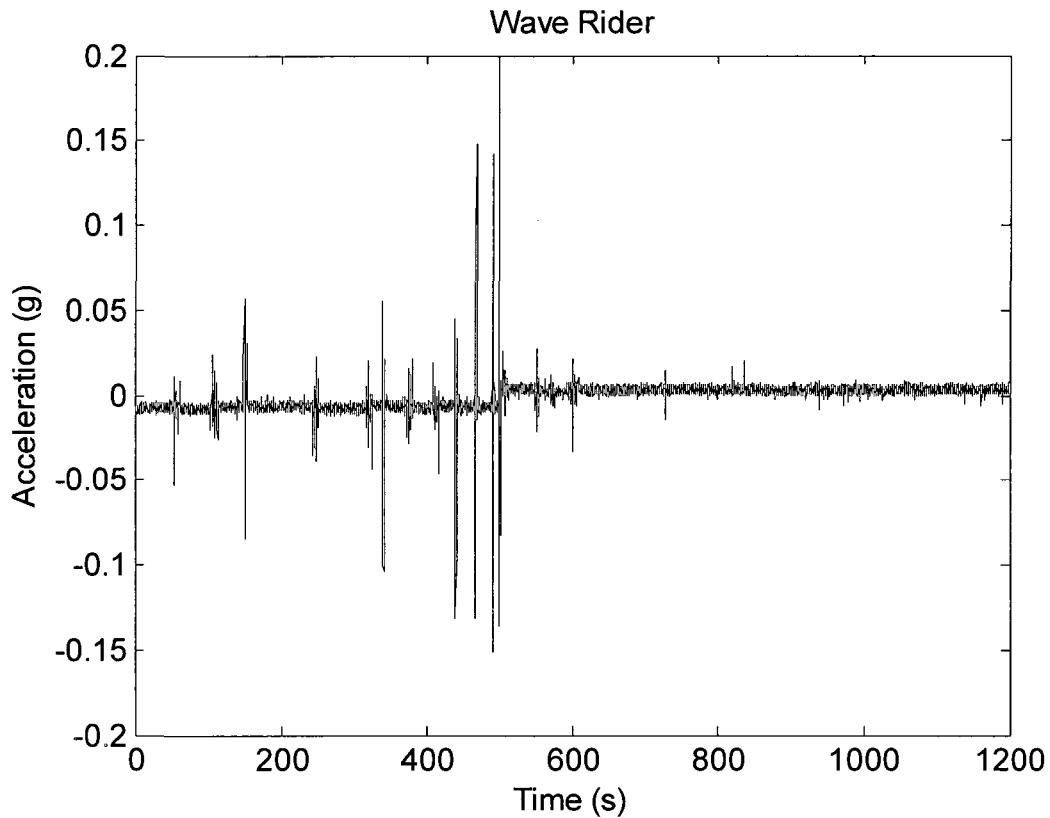


Figure 21: Wave Rider accelerometer data before separation into individual tests

The acceleration plots for the entire batch had to be inspected and the duration of each test identified by the spikes in acceleration. Since the accelerometers were still before and after each test, finding the end points was easy for this test. However, in a field experiment, determining when each drop began and ended would be quite difficult. With the time periods for each test identified, the acceleration was integrated twice to determine the displacement, which was compared to the actual movement. The tests were executed several times to determine repeatability. The results of these tests are shown in Figure 22 to Figure 25.

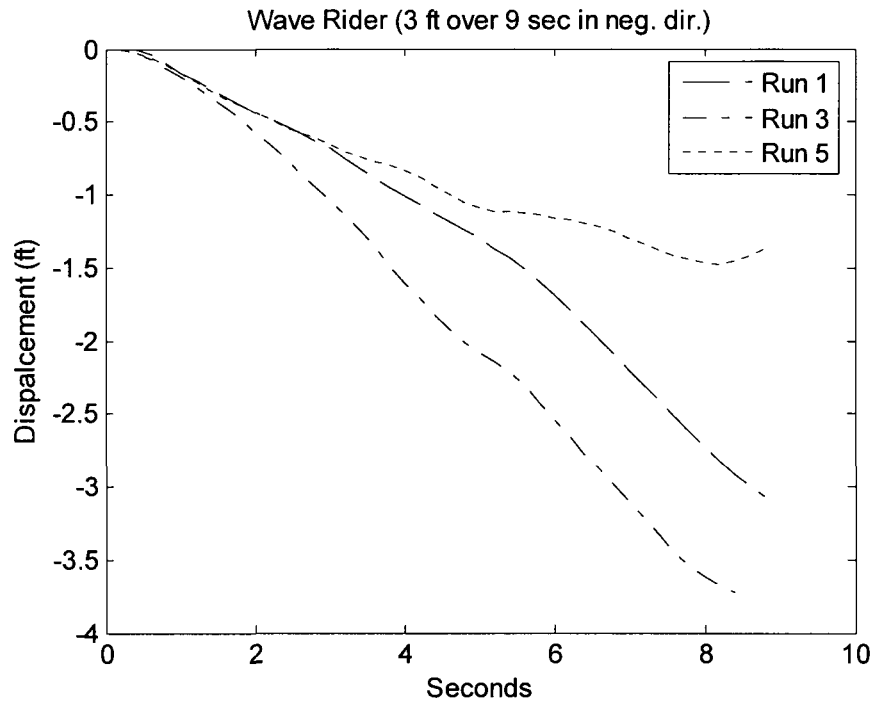


Figure 22: Wave Rider accelerometer results in the negative direction

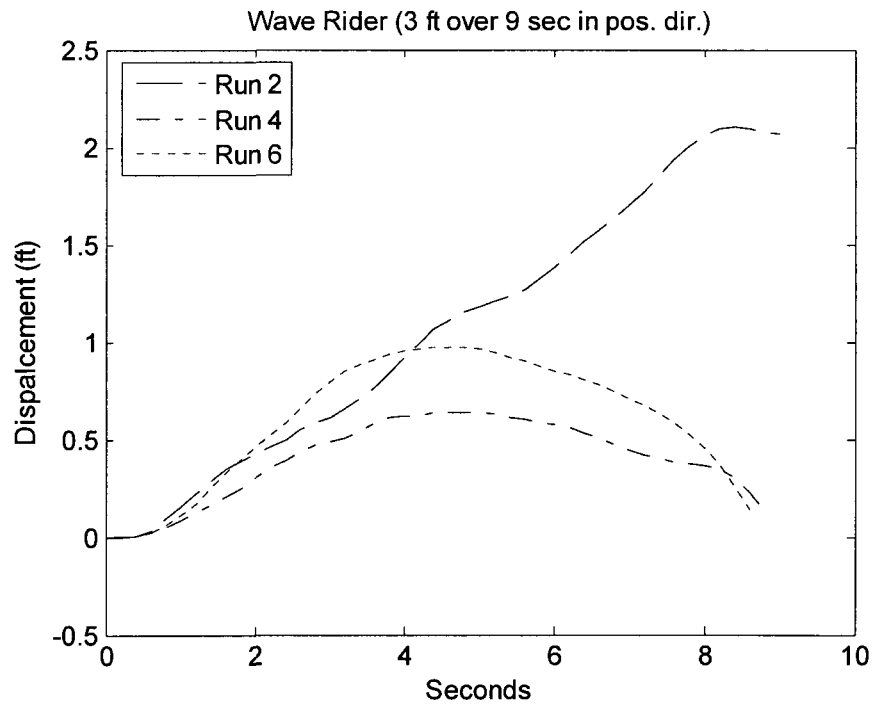


Figure 23: Wave Rider results in the positive direction

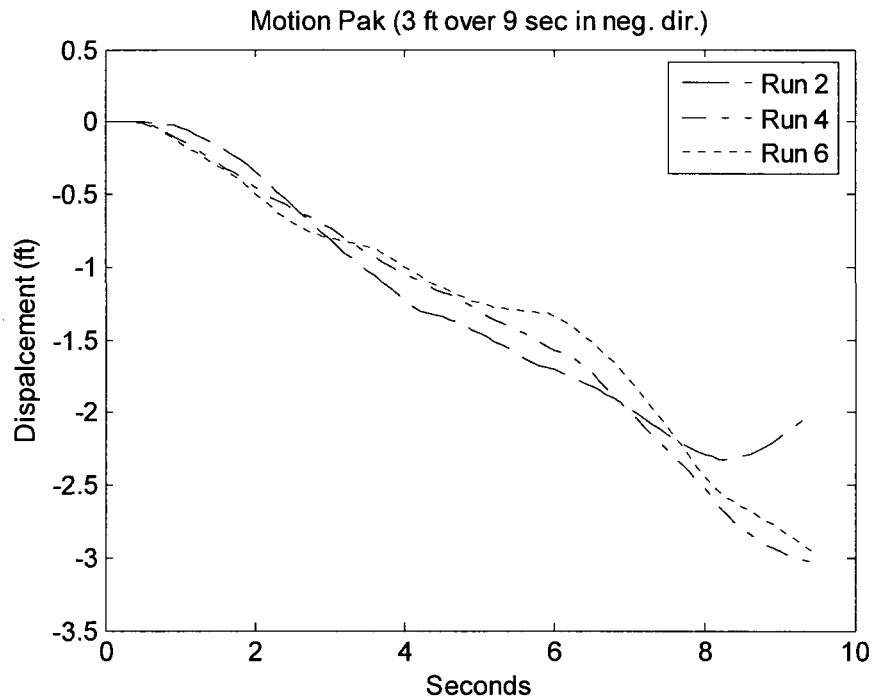


Figure 24: Motion Pak results in the negative direction

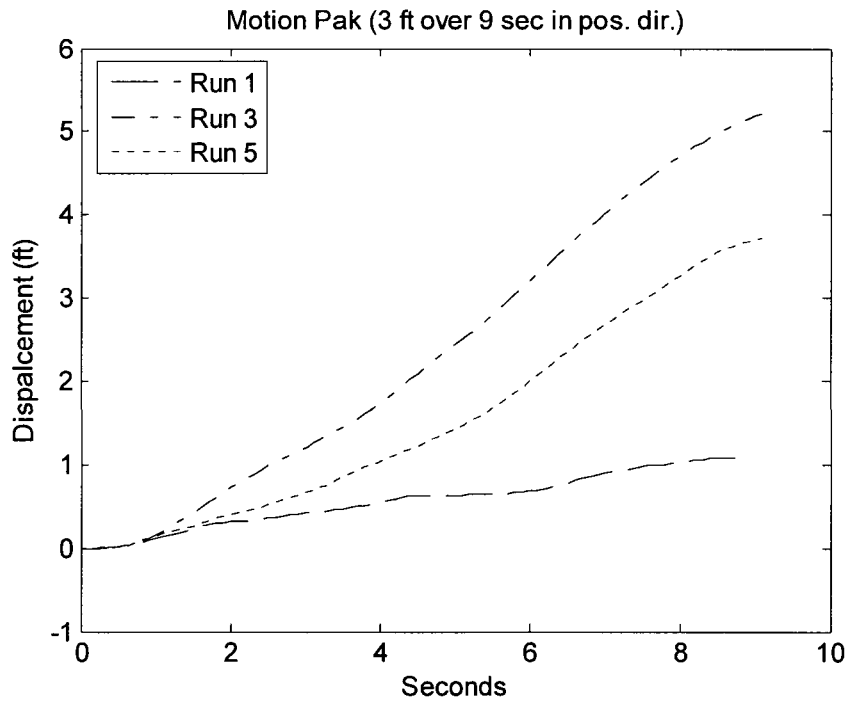


Figure 25: Motion Pak results in the positive direction

Of the six tests with the Wave Rider accelerometer only one run showed a displacement of 3 feet over the course of 9 seconds. The remaining runs had an error in

the endpoint displacement of up to 2.9 feet. As such, the Wave Rider accelerometer was not an option for tracking the scale model in a field test. The Motion Pak produced slightly more accurate results. Two out of the three runs in the negative direction showed a displacement of three feet, with the remaining run having an error of 0.9 feet. Meanwhile, only one of the three runs in the positive direction showed a displacement of three feet. It is important to note that these tests assumed that the acceleration was in one direction. In a field test, the direction of motion would be unknown and a new method for processing the data would need to be developed. The new method would also have to account for the model and accelerometer spinning during descent. Based on the poor accuracy of the tests and the time necessary to process the field data, neither accelerometer was suitable for tracking the model during field tests.

Acoustic Tracking

There are several underwater acoustic positioning systems that are commercially available and use different methods to determine position. The particular system considered in this investigation was produced by Hydroacoustic Technology, Inc (HTI) and is typically used to track fish in natural and aquaculture environments. The system uses at least four hydrophones to determine the location of up to 50 acoustic pingers. The omni-directional pingers were programmed to transmit a pulsed 307 kHz signal each with a different time between pulses. Knowing the locations of all of the hydrophones, the position of each pinger can be determined from the time difference for the signal to reach each hydrophone. For the scale model test, a pinger would be attached to the model. As the model fell from the water surface to the seafloor, the HTI system would determine its

location and provide a record of the model's starting location, trajectory, and landing position (Ehrenberg & Steig 2002; Ehrenberg & Steig 2003).

Because the system's accuracy was unknown, a series of tests was performed in the UNH engineering tank to become familiar with the system and evaluate it for use in this project. A cylindrical fish cage was suspended in the tank with 12 pingers attached to it. The first eight pingers were attached to the net halfway between the top and bottom rims. The pingers were equally spaced around the circumference. The remaining four pingers were attached to the bottom rim, also equally spaced. The first pinger was programmed with a two second pause between pings, the second with a 2.1 second pause, and so on. The hydrophones were hung around the cage from the tank's carriage. Their locations were measured with a measuring tape and entered into the system's software package.

Because the cage remained still during data recording over several hours, 12 small clusters of position points were expected in the results. The actual results for one hour are shown in Figure 26 and Figure 27 and rest of the results are shown in Appendix B. The system was only able to calculate positions for nine of the 12 pingers and those which it could calculate did not coincide with the actual pinger locations.

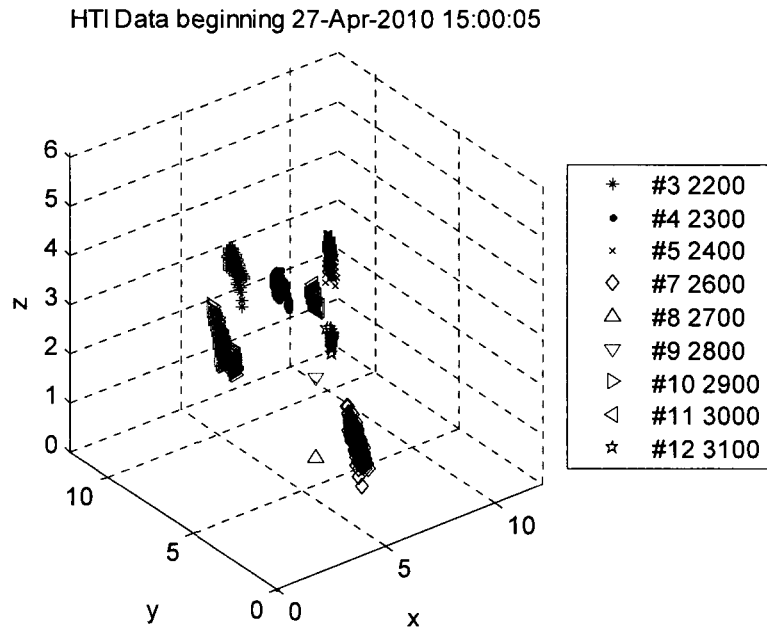


Figure 26: HTI evaluation results from the UNH engineering tank

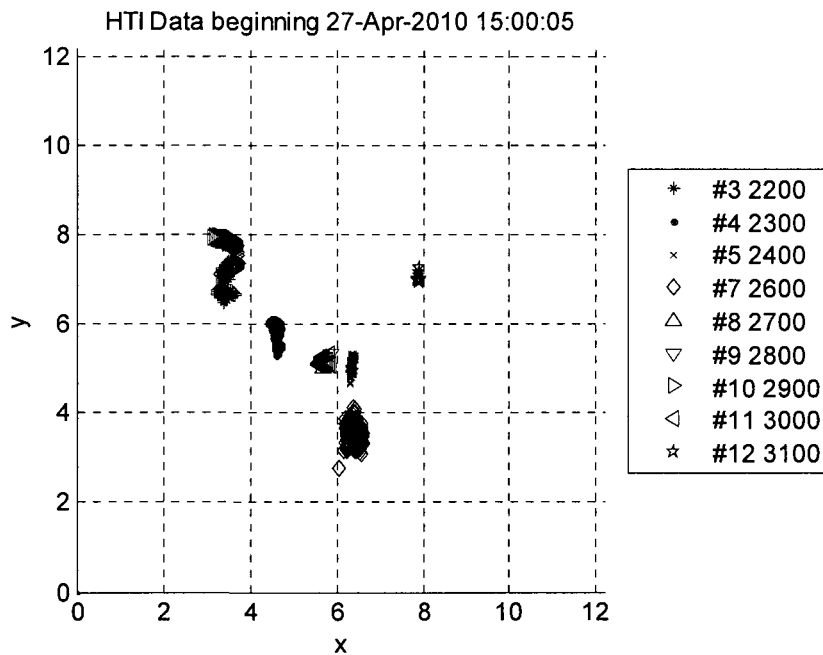


Figure 27: HTI evaluation results from the UNH engineering tank (top view)

However, several factors were identified which may have contributed to the error in reported location. Since the pingers transmit an acoustic signal, that signal may have echoed off the solid tank walls. For a single ping, the hydrophones may have recorded

the initial signal as well as a few echoes. Although, the hydrophones were said to be omni-directional, there appeared to be a dead-zone behind them where the pingers could not always be heard. Directing the hydrophones towards the pingers rather than hanging face-down may have produced more accurate results. The hydrophones' locations were also measured with a measuring tape and were, therefore, not exact. Since the algorithm that calculated the pinger locations used the hydrophone locations, any error in those locations could prevent the system of equations in the algorithm from converging to a solution. A discussion with an HTI representative revealed a method to determine a more exact location for each hydrophone.

With the new information, a second test was performed at the UNH research pier in New Castle, NH. The same cage was moored just off of the pier, with the pingers attached in the same locations as the tank tests. Figure 28 shows a schematic of the test set-up.

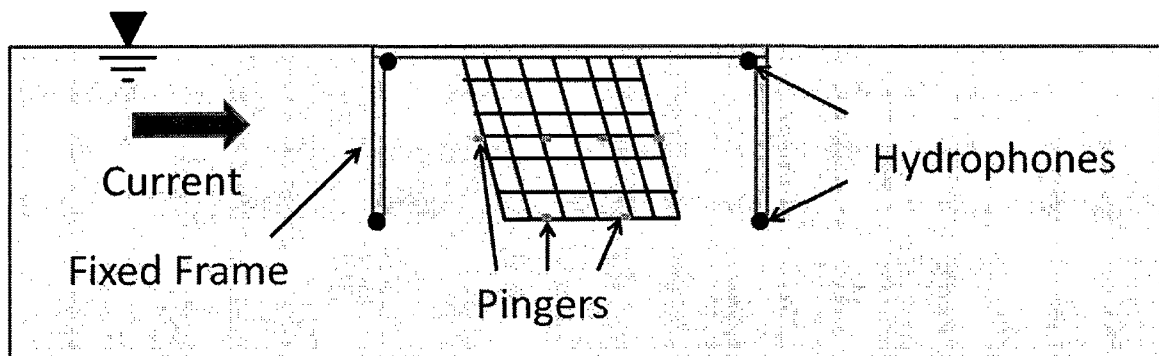


Figure 28: Schematic of the HTI pier test set-up

The hydrophones were rigidly attached to a frame surrounding the top rim of the fish cage and were directed towards the center of the cage. The hydrophones were placed at two different depths, with the opposite corners in the top view being at the same depth, since the system was shown to provide more accurate results in that configuration.

Rather than physically measuring the relative locations of the hydrophones, they were

acoustically measured. One at a time, each hydrophone was set to ping and the time taken for that signal to reach the remaining three hydrophones was recorded by the system. That data file was sent to HTI and they provided exact hydrophone locations.

The test was conducted during slack water, when the cage and pingers should have been stationary. Figure 29 and Figure 30 show the results from the HTI evaluation tests at the UNH research pier.

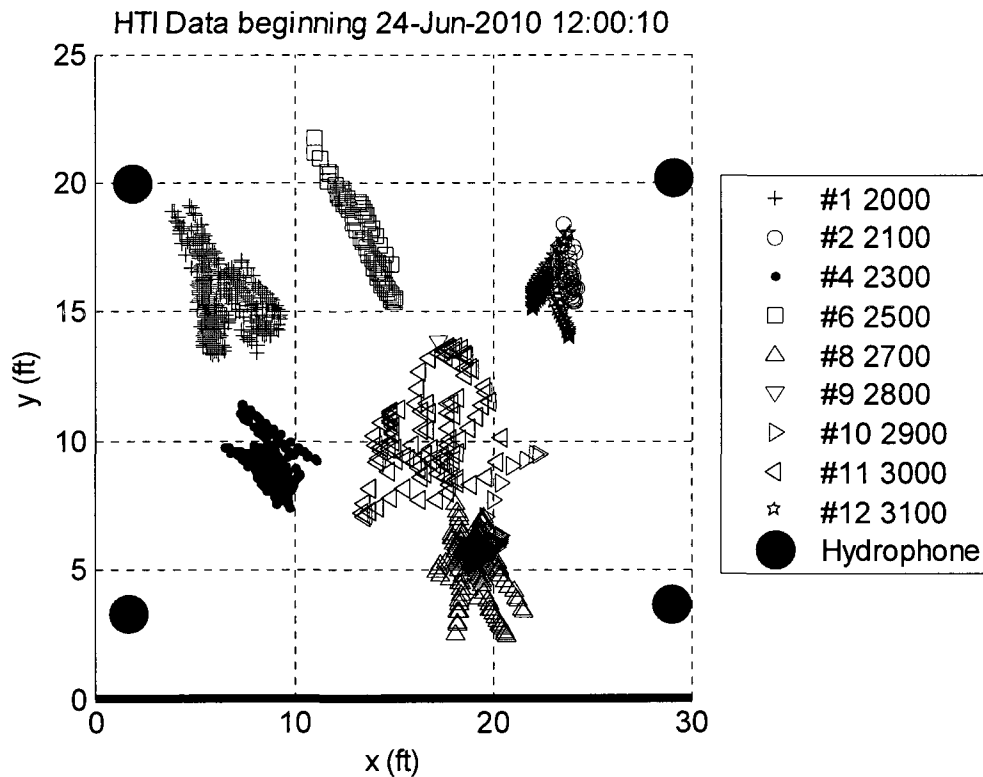


Figure 29: Results from the HTI pier testing (top view)

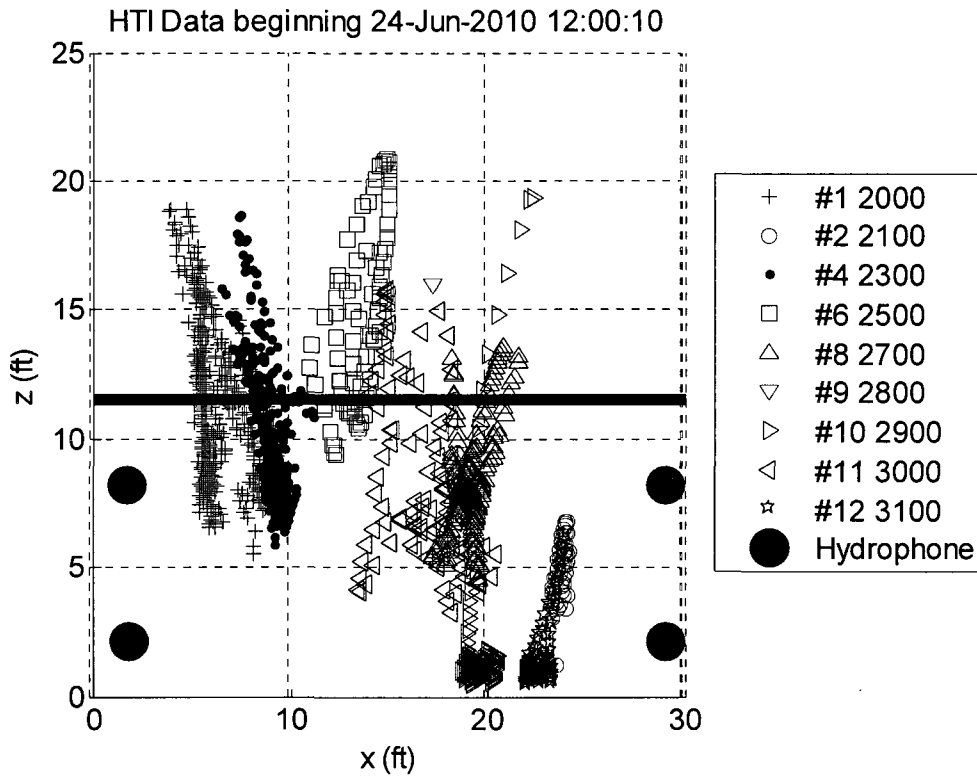


Figure 30: Results from the HTI pier testing (side view)

The larger dots represent the locations of the hydrophones and the solid blue line represents the water level in the side view. Again, locations were not determined for all of the pingers. In the top view, the pinger locations did not appear as small clusters in a circle as they had been expected to. The variability in the location of each pinger was far greater than what had been anticipated. The lack of accuracy was more pronounced in the side view, where in several instances the pingers were determined to be above the surface of the water. The conditions at the pier closely resembled the conditions in which the system would be used for a scale model test. Since the system was unable to identify the locations of the pingers with an accuracy much less than meter, it was determined that the HTI acoustic tracking was unsuitable for the scale model tests.

Visual Tracking

Since a measurement system could not be found within the budget and time constraint of the project, the decision was made to visually track the model during field tests using both rigid mounted cameras and mobile, diver-held video. Details about the camera and the mounting methods are explained in the test set-up description.

Final Large Scale Model Design and Construction

This model was primarily constructed of an HDPE outer shell, a steel support, concrete ballast, and closed-cell packing as shown in Figure 31.

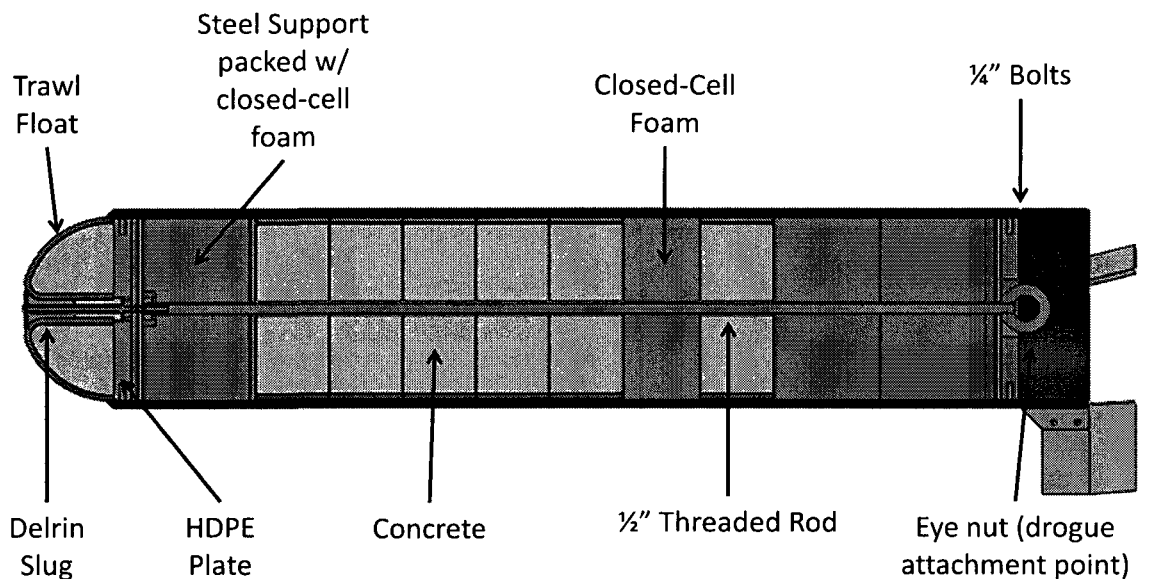


Figure 31: Cross-sectional view of the open ocean model

The scale of the model was adjusted to $1/4.87$ after determining the material for the outer shell. Table 12 summarizes the scaled physical characteristics for the model. The weight in water is equivalent to weight in air minus the weight of water displaced. The flooded weight represents the weight of the system including any water that enters the outer shell. The center of gravity is measured from the base of the nose towards

the rear of the model. The drogue is sized to slow the system from the terminal velocity to the impact velocity.

Table 12: Scaled physical characteristics for the open ocean model

	Full Scale	1/4.87 Scale
Length (ft)	15.7	3.22
Diameter (in)	42	8.625
Weight in Water (lbf)	3,094	26.79
Flooded Weight (lbf)	13,480	116.7
Center of Gravity Location (in)	73.56	15.104
Terminal Velocity (m/s)	12.26	5.55
Impact Velocity (m/s)	1	0.453
Drogue Diameter (ft)	16.82	3.46

The outer shell was 8 inch nominal DR 32.5 high density polyethylene (HDPE) pipe. The actual outside diameter was 8.625 inches, which dictated the adjustment in model scale, and was cut to 42 inches in length. The outer shell contained and concentrically located all of the other model components. A 37 inch long ½ inch threaded rod ran almost the entire length of the model and also located the internal components longitudinally and concentrically.

The majority of the model was composed of six concrete cylinders that served as ballast and were positioned to achieve the correct location of the center of gravity (CG). A sonnet tube of nominal 8 inch diameter was used as the mold when pouring the cylinders; the actual inside diameter of this tube was 7.375 inches. The tubes were cut into 3 inch sections and secured with tape to a plywood base. The center of each mold was marked on the base and a hole was drilled to fit a 5/8 inch wooden dowel post. The post created a hole down the center of the concrete cylinder for the threaded rod to slide

through. After mixing pouring, and letting the concrete cure, each cylinder was weighed and the results are displayed in Table 13.

Table 13: Weight of each concrete cylinder

Cylinder #	Weight (lbf)
1	11.11
2	11.28
3	10.88
4	11.01
5	10.71
6	11.13
7	11.21

Finer adjustment of the CG location was provided by $\frac{1}{4}$ inch thick steel disks that were strategically placed along the length of the model. The remaining interior space was occupied by closed cell foam which displaced water, since the model is not sealed. The stack of concrete cylinders was spaced from the nose cone by a steel support. The upper and lower ends of the support were constructed from $\frac{1}{4}$ inch thick steel disks. A nut was welded to the bottom steel plate to secure the $\frac{1}{2}$ inch coarse threaded rod that ran the length of the model. The disks were separated by four $\frac{1}{4}$ inch thick vertical plates that were welded 90 degrees apart. The space between the vertical supports was packed with closed-cell foam.

The internal components were held in place by two $\frac{3}{4}$ inch thick HDPE plates at either end of the model. Each plate was secured to the outer shell by six $\frac{1}{4}$ -20 bolts that threaded from the outside of the model into helical inserts that had been installed in the HDPE plates. A 2 inch diameter, centered hole was cut out of the rear plate to accommodate an eye nut that was threaded onto the end of the $\frac{1}{2}$ inch rod. The forward plate had a 1 inch diameter hole in the center and was attached to the nose cone assembly.

After exploring several options, the decision was made to construct the nose cone from half of an 8 inch trawl float that was cut perpendicular to the hole through the center of the float. The trawl float provided the necessary hemispherical shape and impact resistance in the event that the model struck a solid object on the seafloor at or near terminal velocity. The trawl float was butted against the forward HDPE plate. Behind the HDPE plate was another $\frac{1}{4}$ inch thick steel plate with a $\frac{1}{4}$ -20 threaded slug facing the nose cone. A delrin slug was turned down to fit snugly into the hole in the trawl float. A bolt was placed through a fender washer, the delrin slug, the trawl float, the HDPE plate, and was threaded into the steel plate. The entire nose cone assembly was then attached to the body of the model.

After completing the model construction, the center of gravity location was verified. A line was marked on the shell where the center of gravity should have been and the model was balanced on a piece of angle iron as shown in Figure 32. Figure 33 shows a closer view of the actual center of gravity in relation to the design center of gravity.

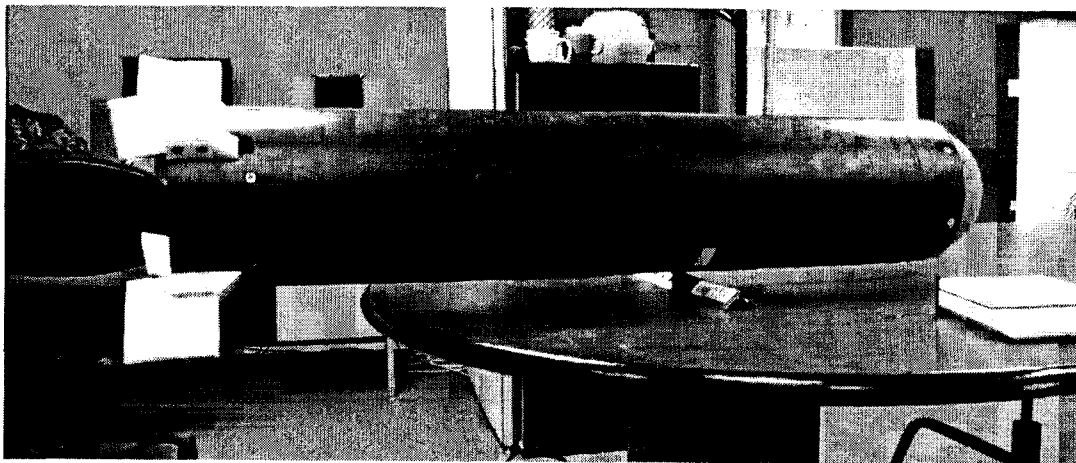


Figure 32: Large scale model center of gravity location verification

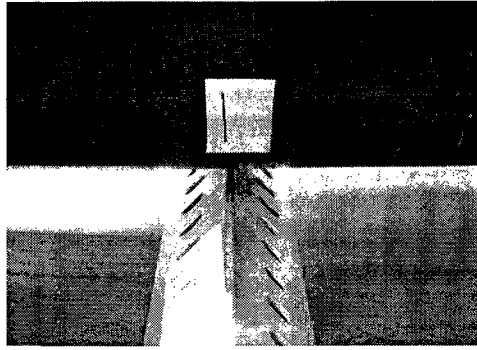


Figure 33: Large scale model center of gravity location

Like the small scale model, a drogue was sized and sewn from eight sport nylon panels. The opening of the drogue was hemmed and reinforced. Quarter inch grommets were installed in the hem near each of the panel seams for the shroud lines. The shroud lines were tied to a swivel so the model could spin independently of the drogue. Small triangular panels were cut out of the center of the drogue between the seams to maintain the drogue's strength while mimicking the hole in the drogue used for small scale testing. The drogue was attached to the model by shackling the swivel to the eye nut at the back of the model. A nylon circle with a large hole in the center was taped to the back of the model to keep the drogue packed until it was deployed. To limit the number of lines in the water, a single line was used to release the drogue and retrieve the model. The line passed through another grommet in the crown of the drogue and a washer with a knot behind it before it was tied to the swivel. The amount of line between the swivel and the knot was 65 inches, such that during descent the drogue would open and the shroud lines would support the weight of the model, but during retrieval the drogue would collapse and the long line would take up the weight.

Field Test

Figure 34 shows a schematic drawing the general test plan. A test barge originally designed for another project was re-purposed for the field tests. It would be

anchored from the bow and stern, holding it in place. A bottom frame with lights and cameras mounted to it would be lowered below the barge using drop lines. A GPS would be used to measure movement of the barge after the frame had been set. An acoustic Doppler current profiler (ADCP) would be used to measure the water currents, and divers would assist with the deployment of the frame, take pictures and video, and record how far away the model impact was from the target.

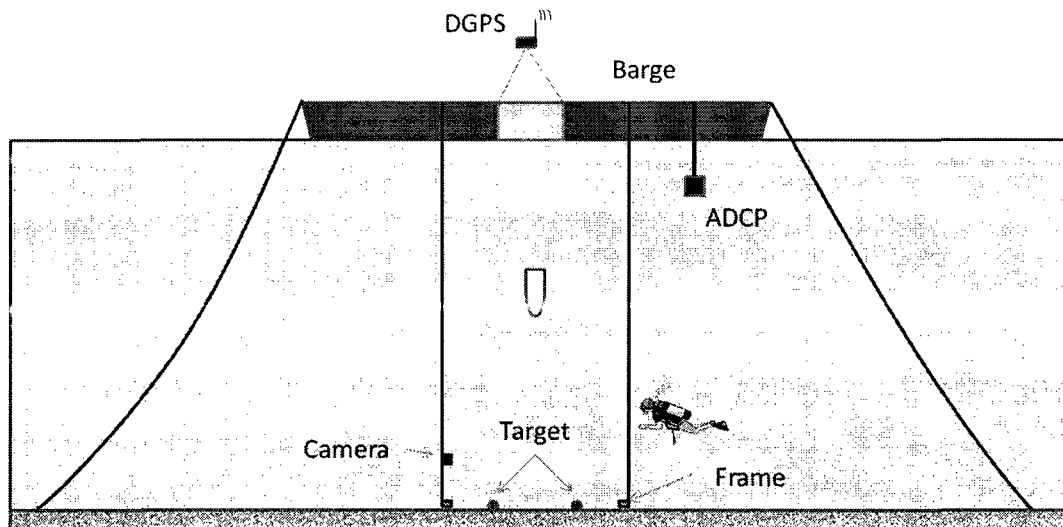


Figure 34: Schematic of the field test plan

A depth of 50 feet was chosen for the field tests as a balance between several factors. The minimum height from the bottom where the drogue deployed would be the same regardless of the water depth. A larger depth would allow for the model to free fall for a larger portion of the depth, giving a better idea how the system would behave for the majority of the 5000 meter (full scale) descent. However, a large water depth would introduce a variety of complications that would decrease the feasibility of completing the tests. The amount of line necessary to reach the bottom would be extremely prone to tangling both on the deck and in the water which would make deploying the bottom frame exceptionally difficult. Trying to position the frame directly under the test

platform would be nearly impossible in any current. Divers could assist in lowering the frame to the bottom, but they too would be restricted by the depth. A diver can remain at 50 feet for 80 minutes without completing a decompression stop according to the National Association of Underwater Instructors' (NAUI) dive tables. Any deeper than 50 feet, a diver's time underwater is limited to under an hour, which doesn't allow for nearly as many drops. Lastly, there are several sheltered, low current places where 50 feet of water is available near the UNH research pier. A preferable location would be outside Portsmouth Harbor to the north, away from the tidal current. However, in the event of poor open ocean conditions and large waves, 50 feet can also be found inside the harbor where tests can be completed at slack water. Two sites were selected with around 50 feet of water, one in a cove off Gerrish Island and another near the UNH research pier in Portsmouth Harbor.

Vessel, Equipment and Location

The research boat used for both the site evaluation and testing was the Galen J, equipped with a depth finder and GPS. The boat is 22 feet long and powered by a 75 HP outboard diesel engine. The test barge was tied to the port side of the Galen J during transportation and testing. The barge was previously built and used as a platform for testing the ability of a tidal turbine to extract energy from the tidal currents under the General Sullivan Bridge in the Piscataqua River. The barge has a wood deck that sits on top of two large metal pontoons. The deck measures 10 feet wide by 35 feet long, with a square hole near the center that measure 5 feet by 6 feet.

The barge was modified to meet the needs of this project. A wood frame was constructed six feet over the opening in the deck. It was supported on each side by 4 by 4's and braced with 2 by 4's as shown in Figure 35.

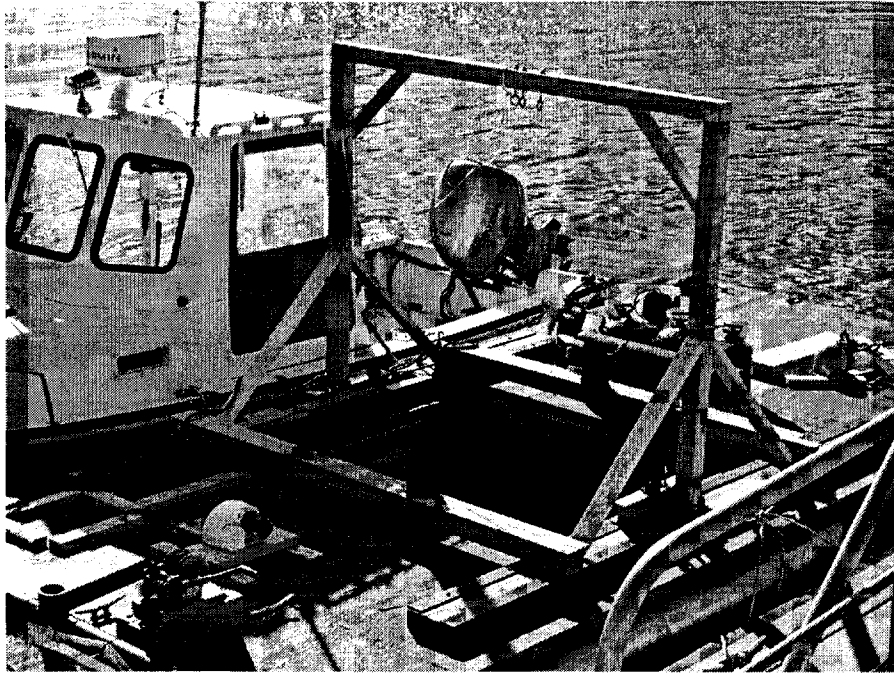


Figure 35: Test platform with wood drop frame

Two ½ inch eyebolts were installed in the middle of the beam. The quick release, which was used to drop the model, hung by a braided line from one of the eye bolts. The model retrieval line ran through a pulley that hung from the other eye bolt. A capstan winch was installed in-line with the pulley to assist in pulling the model back to the surface.

The bottom test frame was assembled on the bow of the test barge. It was built using four inch, DR 11 high density polyethylene (HDPE) pipe, and several fittings including tees, elbows, ends, and bolt plates. The frame, shown in Figure 36, measured 10 feet by 10 feet and was constructed in four pieces, which were later bolted together.

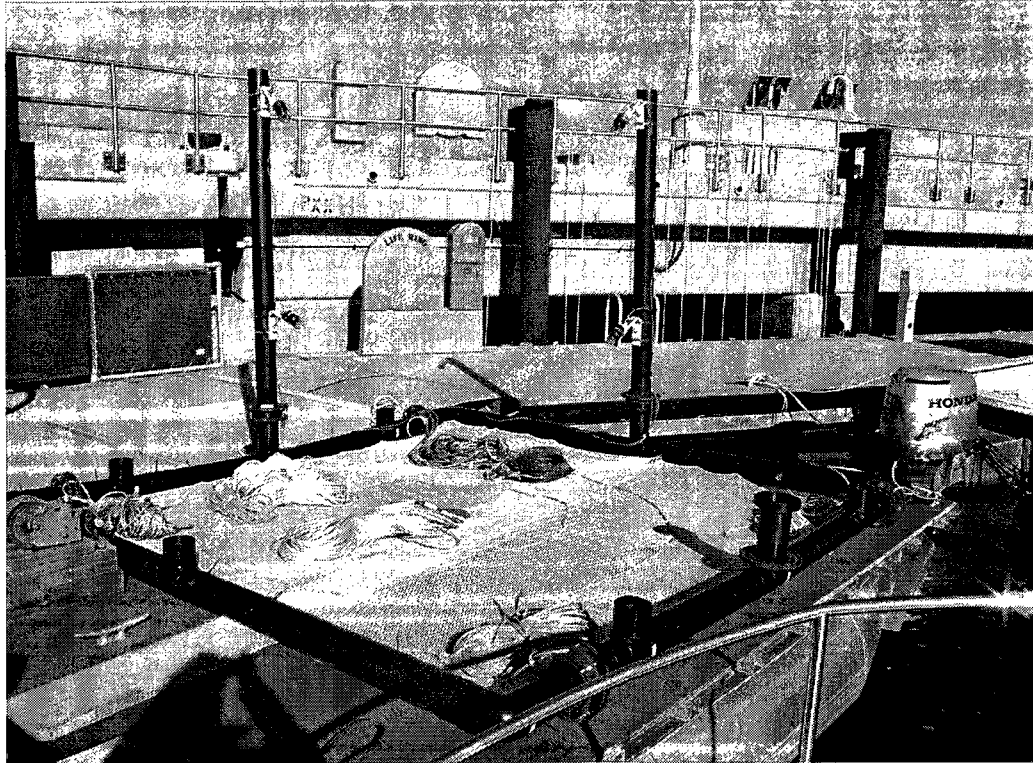


Figure 36: Bottom frame

This construction method allowed for a large frame that was still manageable to move and transport. The opposing sides of the frame were identical. The longer sides included two elbows and a tee fitting, extending upwards; the shorter sides included 3 tee fittings, also extending upwards. At each of the ends was a steel plate with 8 bolt holes that was kept from falling off by an end fitting with a flange.

Each of the joints between the pipe sections and fittings was fused together using the pipe fuser shown in Figure 37.

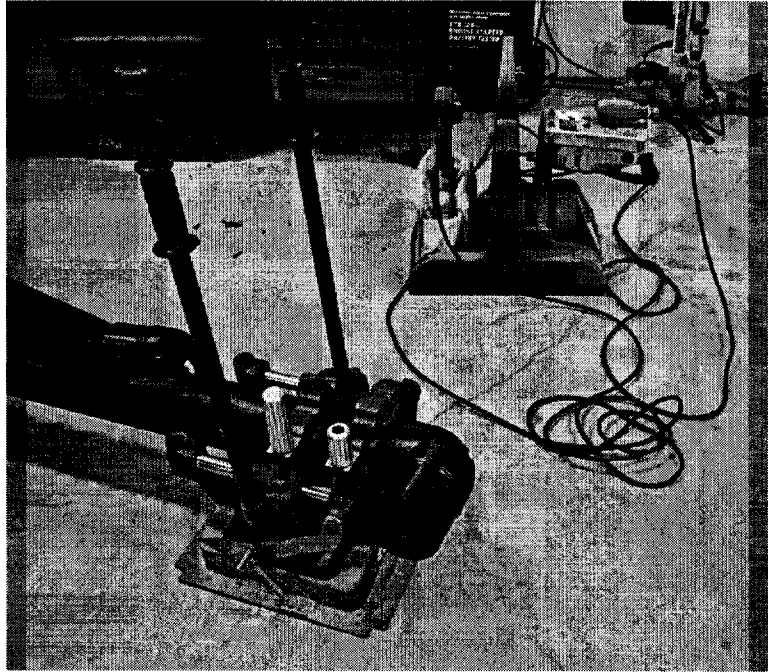


Figure 37: HDPE pipe fuser

The two pipe sections or fittings were secured into the press by tightening the silver handles. The alignment of the two pieces was checked to be sure that the resulting joint would create a straight pipe section. Then the ends of the pipe were squared off using the saw on the right side of the green cradle. The saw had two rotating knife edges that cut away a small amount from the end of the pipe. Once the edges were clean and square, the heating plate was placed between the two pieces and allowed to melt the plastic for about a minute. When about an 1/8 inch of plastic had melted on both pieces the heating plate was removed and the two pieces were pushed together and held in place until they were cool enough to touch. At that point, the newly formed section was removed from the press and the next joint was made.

After the fuses were complete, the frame was bolted together with 1/2 inch bolts and a net was stretched across the square opening and zip tied in place. In the center of the net, targets were marked which corresponded to the 100 meter target radius, scaled for both of

the testing depths: 20 feet and 50 feet. Lines that were tied to each corner of the frame were used to lower the frame to the seafloor and retrieve it when testing was complete for the day.

Two posts were bolted to the upward facing tees on adjacent sides on the frame, each of which held an underwater light and camera manufactured by SeaView. The camera, model number SM-50-C, captured black and white video and was rated to 300 feet. It came with 50 feet of cable which terminated in an RCA video jack and 12 VDC cigarette lighter adapter power plug. The SeaLite Spectra 35 light included a 100 Watt halogen lamp, powered at 12 VDC, and 35 feet of cable with positive and negative alligator clips on the end. Since none of the cables were long enough to extend to the seafloor and connect to the equipment on the test platform, additional cable was spliced between the end connections and the cameras and lights.

The cameras and lights were attached to the vertical pipes on the frame with small mounts, one of which is shown in Figure 38.

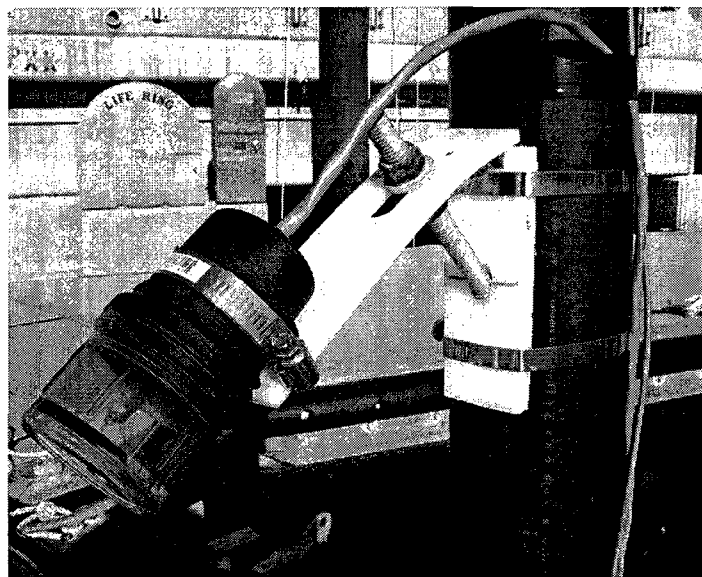


Figure 38: Mount for the underwater cameras and lights

Two hose clamps held the mount to the pipe and another hose clamp held the light or camera to the mount. A small piece of neoprene was placed between the light or camera and the mount to prevent any slipping. The two plates were constructed from HDPE sheet plastic. The top plate was $\frac{1}{4}$ inch thick and had a $\frac{5}{8}$ inch slot milled between 1 inch and 3 inches from the end. The other plate was $\frac{1}{2}$ inch thick and had a hole drilled 3 inches down from the top at a 45 degree angle, into which a helical insert was installed. The two plates were held together by a 1 inch wide brass door hinge. A $\frac{1}{2}$ -13 threaded rod was installed through the slot in the top plate and threaded into the helical insert. The rod had a nut and washer on both sides of the top plate which were used to hold it at a particular angle, aiming the light or camera.

The cables from the cameras and lights were taped to the pipes, along the frame, and up one of the lines used to lower and retrieve the frame, where they were connected to their power supplies and video equipment. The lights were clipped onto two 12 V marine batteries wired in series. The additional voltage was required because of the power losses in the extra cable that had been spliced onto the light. The camera cables ran into a plastic tub that housed their power supply and video conversion equipment as shown in Figure 39.

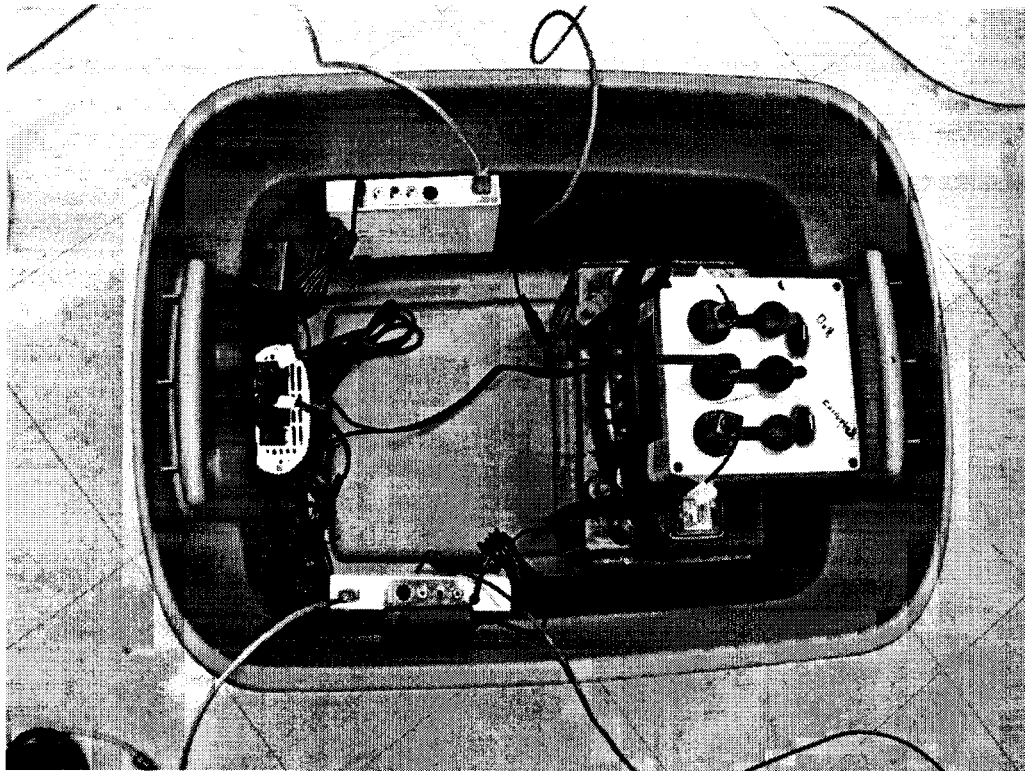


Figure 39: Electronic test equipment set-up

Two Canopus ADV100 video converters were used to convert the video signal from analog to digital. The converter boxes output the signal via a 4-pin IEEE 1394 firewire cable which was plugged into a laptop for recording. Windows Movie Maker was used to capture all of the video. All of the cameras and video conversion equipment was powered by a 12 V marine battery. A power conversion box was created which connected to the leads on the battery and had 3 cigarette lighter outlets, two of which were used to power the cameras. The last outlet was used for a power inverter since the video converters required 110 VAC for power. All of these components were held in place inside the tub by Velcro to prevent any damage.

Since the currents at the test site would directly affect the experiments outcome, a RD Instruments Workhorse acoustic Doppler current profiler (ADCP) was used. It gave a real-time readout of the current magnitude and direction in addition to storing that data

for processing after testing was completed. All of the equipment was tested while tied to the pier on October 28, 2010.

Because the marine forecast leading up to the November 10, 2010 test day predicted open sea waves in the 10 foot range, the decision was made to test at a site inside Portsmouth Harbor. Figure 40 shows the area of Portsmouth Harbor near the UNH research pier. Much of the area is around 50 feet deep.

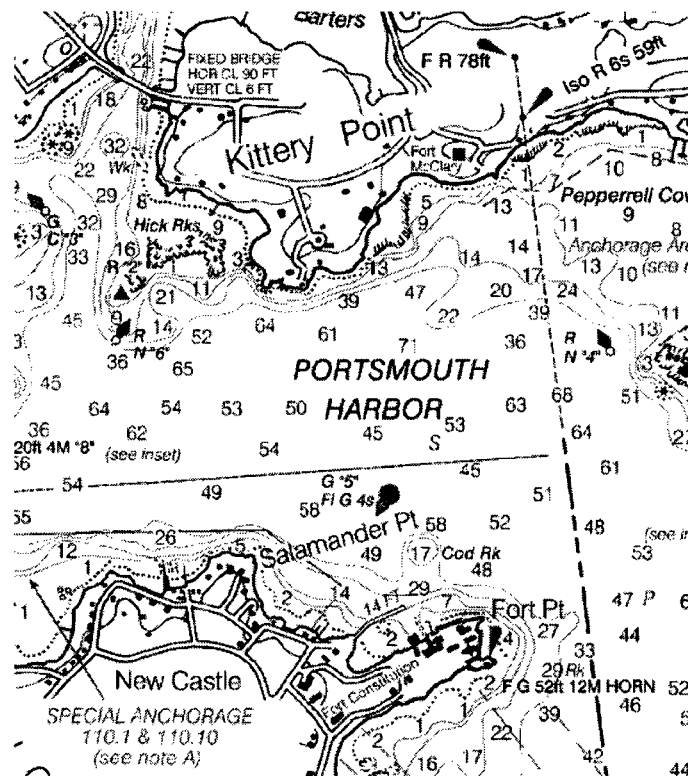


Figure 40: Portsmouth Harbor test site (NOAA nautical chart # 13282)

Before testing, a day was taken to scout the site for an exact location to determine how the barge would be tied up, find a suitable, sandy bottom free of large rocks, and measure the current around slack tide. The UNH Galen J, a research boat, was taken just north of the research pier to a large mooring field which was largely empty since most boats are taken out of the water and winterized in the fall. The empty mooring balls

presented a quick and easy way to position the test platform without the need for deploying and setting anchors.

A drop sampler and underwater video camera were both used to inspect the bottom inside the mooring field. The drop sampler, shown in Figure 41, was set so the clamshell halves were held open, dropped over the side of the boat, and allowed to free fall to the bottom where the impact caused the clamshell halves to close, collecting a sample of the bottom.

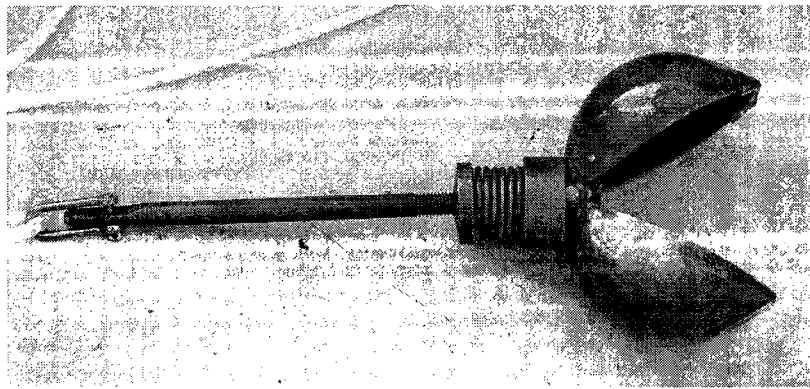


Figure 41: Bottom sampler

Some samples revealed that the bottom was composed mostly of small pebbles, sand, silt, and shells while other came up completely empty. It was possible that the empty samples were a result of the drop sampler closing on top of much larger rocks, so a video camera was lowered into the water to visually inspect the bottom. The video confirmed that there were patches of sandy bottom surrounded by rocky outcroppings. A still from the camera is shown in Figure 42.

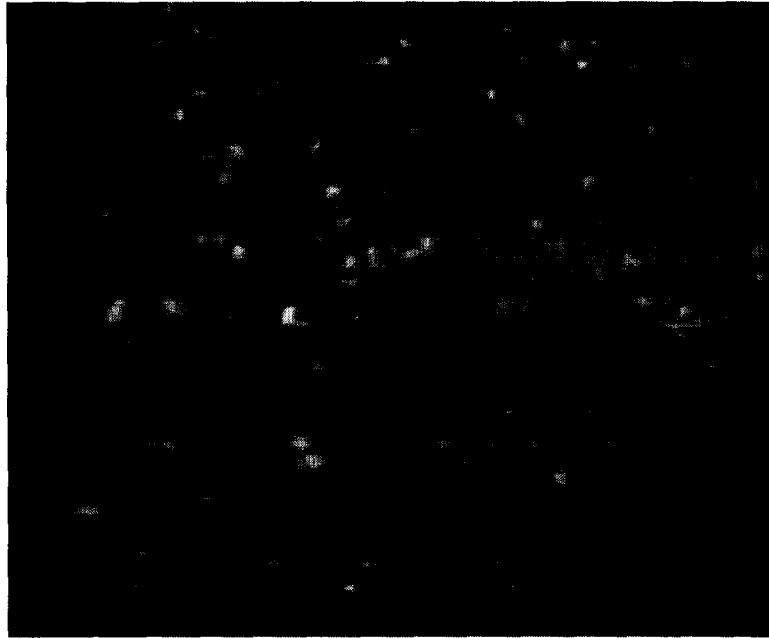


Figure 42: Still capture from the bottom inspection at the 50 foot test location

Using the video camera in combination with the boat sonar, an exact location was determined which had an acceptable bottom and 55 feet of water. The test site location is marked by the green arrow in Figure 43; the GPS coordinates were N 43° 4.402, W 70° 42.78'. The test platform could be tied off between the mooring balls just to the left and to the upper right of the arrow.

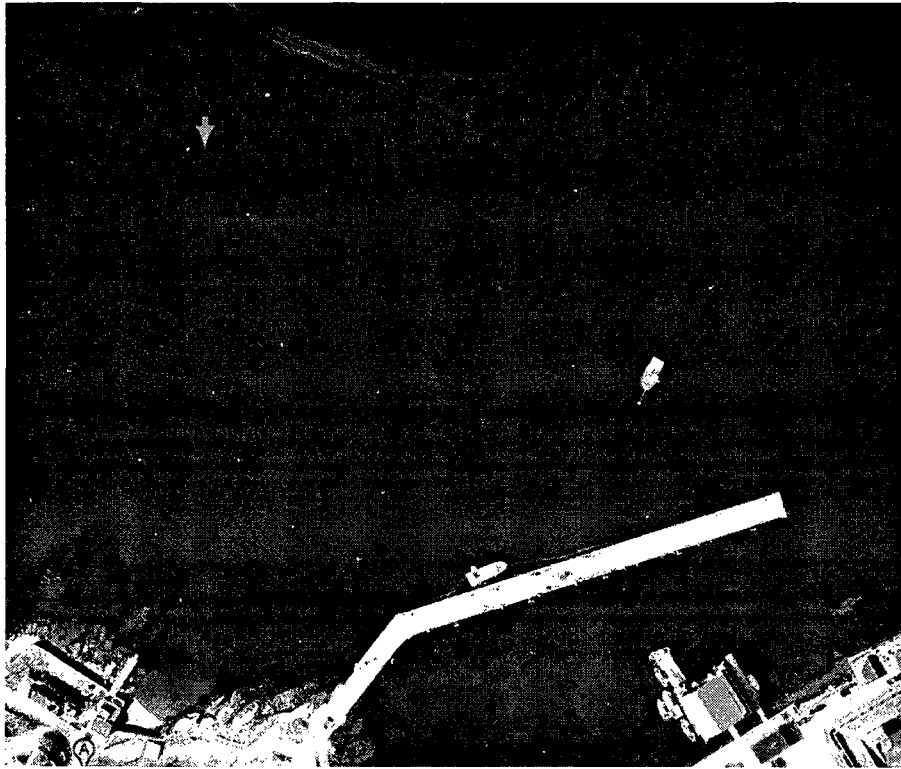


Figure 43: Exact test site in the mooring field

Since the site was in a harbor, significant currents were present due to the tidal changes. It was necessary to gather more information about the currents at the location in the river where testing was to take place. Knowing when slack occurred and what current velocities were present at that time were important in interpreting the model behavior during the tests because even at slack water, there is still some current present. A Marsh-McBirney electro-magnetic current meter was used to take the current measurements. When lowered into the water on a pole, it gave a value for the current speed at a point location when the sensor was directed into the flow. In Portsmouth Harbor, low tide and low slack water, for example, do not occur at the same time. The National Oceanic and Atmospheric Administration (NOAA) provides predictions for the time of slack for several locations in the harbor, one of which is Salamander Point, just to the northwest of the research pier. On November 9, 2010, the day the test site was investigated, NOAA

predicted that low slack tide would occur at 8:59am (NOAA 2006). The measurements that were taken with the Marsh-McBirney are presented in Table 14.

Table 14: Site evaluation current measurements

Time	Current (ft/s)
8:11 AM	1.5
8:17 AM	1.1
8:23 AM	1.1
8:27 AM	0.8
8:31 AM	0.9
8:35 AM	0.8
8:37 AM	0.8
8:41 AM	0.9
8:44 AM	0.3
8:49 AM	0.3
8:53 AM	0.2
8:58 AM	0.5
9:01 AM	0.2
9:09 AM	0.3

It is important to note that wind was considerably high and may have generated a surface current that affected the measurements. These measurements showed that approximately 15 minutes before the predicted slack tide, the current became noticeably lower, which indicated when testing could be started in relation to the slack tide prediction.

Test Procedures

Preparation for the 50 foot testing started early in the morning on November 10, 2010 because NOAA predicted that slack tide would occur at 9:52 am. Before leaving the research pier, all of the electronic equipment including the cameras, lights, ADCP, and winch were connected to their batteries and their function was verified. The camera mount angles were checked. The drogue was packed into the back of the model and the 15 degree fins were bolted in place. The barge was tied to the port side of the Galen J

with a stern line, bow line, and two spring lines, and then transported to the testing site at the edge of the mooring field on the other side of the pier.

Once at the test site, the barge was tied up to two existing mooring balls. A line was secured to a cleat on the fore starboard of the barge and run through the eye of the mooring ball pick-up line. The free end of the line was let out as the boat reversed towards the second mooring ball. A second line was tied off to a cleat on the aft portside of the barge and run through the eye of the second mooring ball's pick-up line. The free ends of the two lines were pulled until the lines were taut and the barge was positioned over the test site that had been identified the day before. The lines were then secured to cleats on the remaining corners of the barge.

The last major task before testing began was deploying the frame. The drop lines that were tied to each corner were faked out to prevent tangling as the frame was lowered. The lines that were tied to the port side of the frame were run across the barge and back under it, so that the frame would hang below the barge with two lines on either side. The frame was pushed off the starboard side of the barge and lowered to the bottom of the harbor. In the current, the frame proved hard to manage. At this point, the divers entered the water and the plum bob was lowered from the wooden frame over the hole in the barge. The divers adjusted the frame's position on the bottom so that the plum bob hung near the center of the target marked on the net. Because of the current and constant motion of the barge, the frame could not be positioned exactly in the center of the target. For this reason, the target rings served as scales rather than actual targets the model should land within. While the divers were moving the frame, the quick release was attached to the eye nut on the tail of the model. When the divers were clear, the model

was lowered into the water so that it hung just below the surface and was ready to begin the first drop.

Each drop started with the model hanging from the quick release in the center of the hole in the barge and the plum bob hanging from the other eyebolt. The procedure for each drop was as follows:

1. The divers were notified of the intent to drop the model with three knocks on the barge's metal pontoon.
2. The plum bob was pulled to the side and the line was retained by a hook in the wooden frame.
3. The laptops were set to record video from the cameras.
4. The time, GPS location, depth and current magnitude were recorded.
5. The quick release was tripped and the model dropped.
6. The plum bob was taken off the hook and hung straight down from the center of the hole in the barge.
7. The divers measured the distance between the plum bob and the model impact point.
8. The model was pulled back to the surface with the winch
9. The drogue was repacked, the quick release was reattached and the model was ready to be dropped again.

Test Results

The model had fins bent at 15° installed for all of the tests performed on November 10, 2010. The first test also included the drogue which was pulled from its cloth packing cover 35 feet below the surface, approximately 20 feet from the bottom.

Deploying the bottom frame took longer than anticipated. As a result, testing began after 9:52 am, when NOAA predicted that slack water would occur. The results for all four drops are shown in Table 15.

Table 15: Field test results

	Drop 1	Drop 2	Drop 3	Drop 4
Time	10:00 am	10:08 am	10:17 am	10:24 am
Minutes after Slack Water Prediction	8 minutes	16 minutes	25 minutes	32 minutes
Depth	55.1 ft	55.5 ft	55.1 ft	55.7 ft
GPS Location	N 43° 4.403' W 70° 42.778'	N 43° 4.405' W 70° 42.782'	N 43° 4.404' W 70° 42.781'	N 43° 4.405' W 70° 42.783'
Current Magnitude	0.25 m/s	0.3 m/s	0.5 m/s	0.25 m/s
Distance from Plum bob	1.1 ft	8 inches	3.5 ft	2.5 ft
Diver Comments		Just off red target, right next to plum bob	Crack in the nose upon inspection	Nose completely smashed during impact

The videos were examined and the ADCP data was processed after testing was completed. The video from drop number 1 showed that the drogue deployed and the model slowly drifted to the bottom. The videos from drop number 2 showed the model impacting the bottom with enough force to kick up a small sediment cloud. During drop number 3, the model could not be identified in any of the videos as visibility had become poor. Upon retrieving the model after the third drop, the nose cone was cracked. The model was dropped for a fourth and final time. Video again showed the model impacting the bottom with significant force, enough to shatter the already damaged nose cone.

The current magnitudes reported in the table were instantaneous current magnitude read-outs from the ADCP. The recorded current data was processed after testing was complete. The data containing information about one minute before and one

minute after each drop test was extracted and an average direction was found for each drop. Using the north and east components, a set of velocity current profiles in the average direction was computed. From these profiles, one average current profile was calculated for each drop, shown in Figure 44.

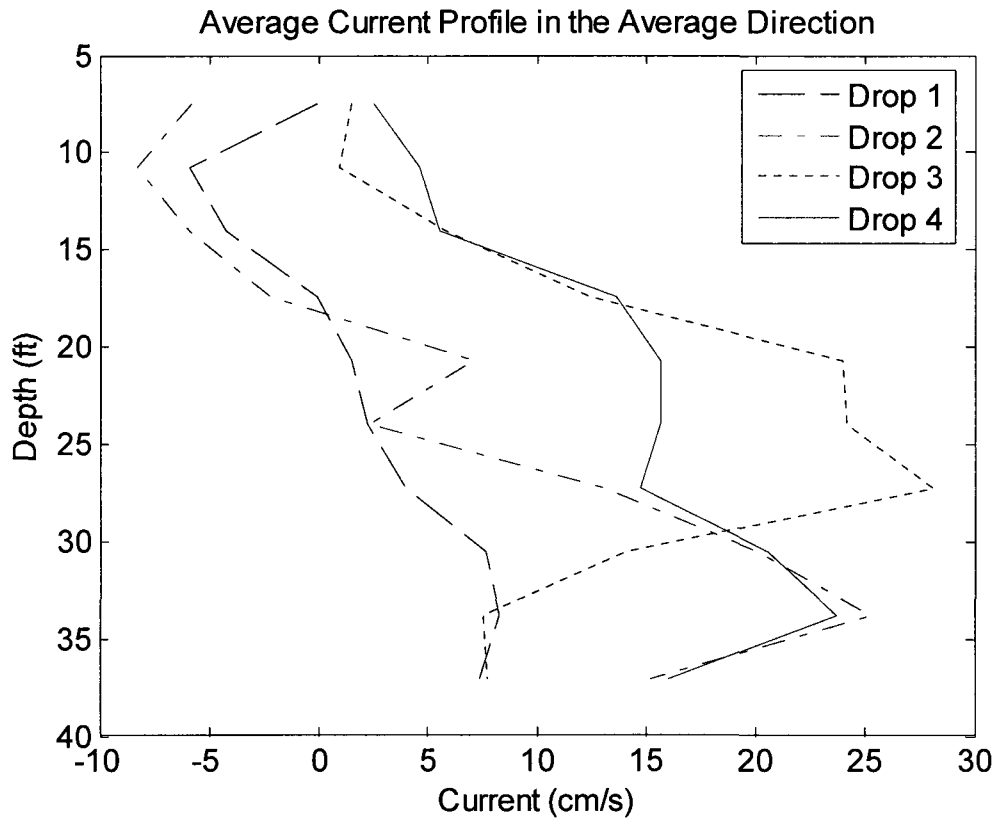


Figure 44: Average current profiles for each drop test

A depth-averaged current velocity magnitude was found for each of the average current profiles and was used to evaluate whether or not the system would have landed within the 100 meter target in the full scale case. The method was very similar to the displacement calculations in Chapter V. Recall that the terminal velocity for the model was 5.55 m/s. In 55 feet of water, the model reached the bottom in 3.02 seconds. Maintaining the assumption that the model travels with the current, the product of the time to reach the bottom and the depth-averaged current velocity magnitudes gave the

horizontal drift from the current which was used to correct the divers' measured distances. That result was converted to a full scale distance from the center of the target area. The results of these calculations are given in Table 16 for each drop.

Table 16: Scaled field test results

	Average Direction (deg)	Depth-Averaged Current Velocity (cm/s)	Horizontal Drift From Current (in)	Measured Distance (in)	Full Scale Distance from the Target Center (m)
Drop 1	209.9	2.053	2.44	13.2	82
Drop 2	196.7	6.097	7.24	8	6
Drop 3	210.0	12.63	15.01	30	114
Drop 4	220.8	13.26	15.75	42	199

The processed depth-averaged current velocities shown in Table 16 are far lower than the instantaneous current velocity magnitudes in Table 15. This is because of the significant scatter in the ADCP data shown in Figure 45. The current velocities are plotted from four selected depths, for one minute before and after each drop.

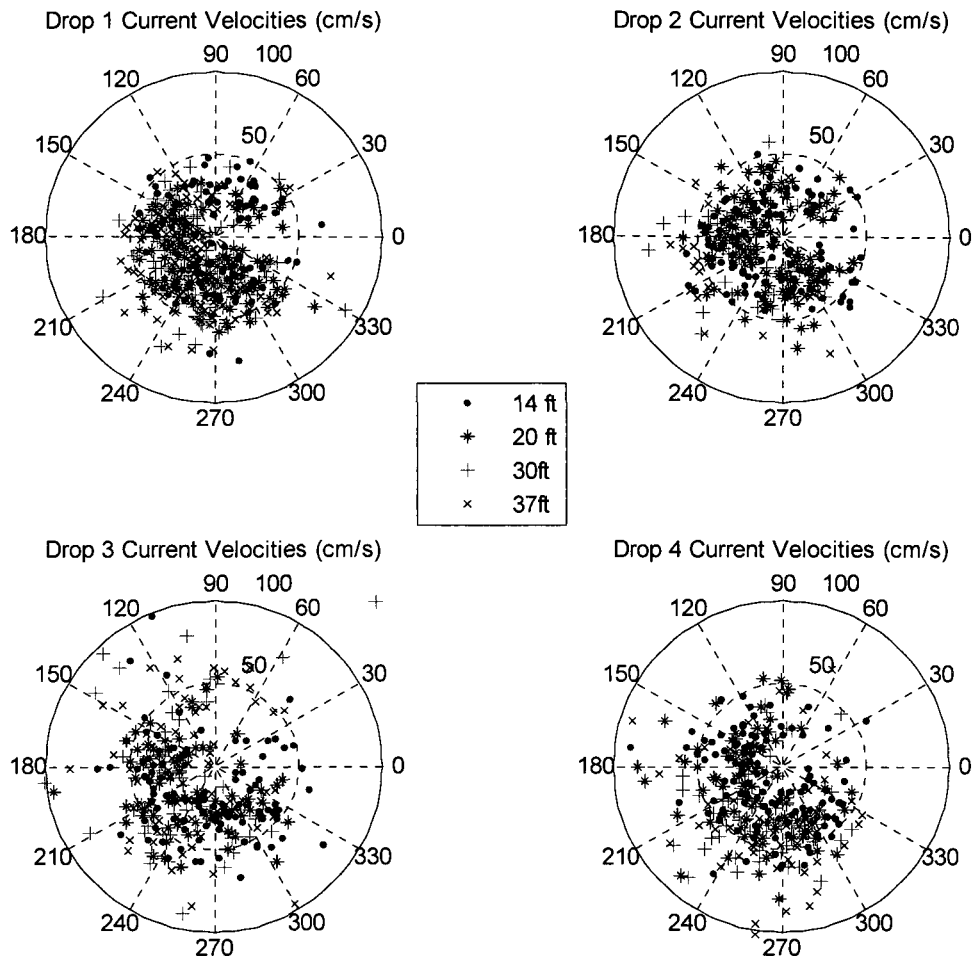


Figure 45: ADCP magnitude and direction data

Since there were significant currents in almost every direction, the higher values were averaged out when computing the depth-averaged current velocity in the dominant direction. The average profiles may have underestimated the actual currents that were present during testing. Additionally, it is important to note that the divers observed the plum bob moving around as it hung from the barge due the waves and wind. This introduced significant error into their measurements.

CHAPTER IX

CONCLUSIONS

Based on the final design, the system could meet the size requirements while providing pressure protection for the electronics and supplying sufficient power with pressure tolerant batteries. The total system volume was well under the 22 m³ design criteria. The analysis also showed that the system could land within the 100 meter target area for the design current profile as well as the currents present at two of the WOCE locations. In the third location, the system would have landed within 200 meters of the target destination in the extreme cases.

Scaled model testing demonstrated the potential of using a free fall scenario. In small scale testing, several center of gravity and fin combinations produced a stable, nose-down orientation during descent, which lead to a vertical trajectory. A drogue could be deployed just above the seafloor to reduce the impact speed, thereby reducing penetration into the sediment and shock loads on the system. Since the drogue would be deployed just before impact in the region of minimal transverse current in the deep ocean, sideways drift at the slower descent speed would be very small. Field testing with the large scale model further solidified a free fall scenario as a viable option for deep ocean deployment. Additional field testing in deeper water, in a location free of tidal currents, would provide more data to determine the repeatability of the field experiments.

LIST OF REFERENCES

Bearman, G. 1989, *Ocean Chemistry and Deep Sea Sediments*, Elsevier Science Ltd, Tarrytown, NY

Berger, W.H. & Winterer, E.L. 1974, 'Plate stratigraphy and the fluctuating carbonate line' in *Pelagic Sediments on Land and under the Sea*, ed K.J. Hsu & H. Jenkyns, Blackwell Scientific Publications, Oxford, England, International Association of Sedimentation, Special Publication 1, pp 11-48.

Chu, Peter C., Gilles, Anthony F., Fan, Chenwu & Fleishcher, Peter. 2002, 'Hydrodynamics of Falling Mine in Water Column', *Fifth International Symposium on Technology and Mine Problem*, Journal of Counter-Ordnance Technology.

Ehrenberg, John E. & Steig, Tracey W. 2002, 'A method for estimating the 'position accuracy' of acoustic fish tags,' *Journal of Marine Science*, vol. 59, pp 140-194.

Ehrenberg, John E. and Steig, Tracey W. 2003, 'Improved techniques for studying the temporal and spatial behavior of fish in a fixed location', *Journal of Marine Science*, vol. 60. pp 700-706.

Teledyne Benthos. 2010, 'Flotation', *Teledyne Technologies Inc.*, [Online] Available at: <http://www.benthos.com/undersea-flotation-device-housing-glass-spheres.asp>

Green, A.W. 1984, 'Bulk dynamics of the expendable bathythermograph(XBT),' *Deep Sea Research Part A Oceanographic Research Papers*, vol. 31, no. 4, pp 415-426.

Hoerner, Sighard. 1964, *Fluid-Dynamic Drag*, Hoerner Fluid Dynamics, New York City, pp.3-12.

NOAA. 2006, 'Tide and Currents: Salamander Point ', *National Ocean Service*, [Online] Available at: http://tidesandcurrents.noaa.gov/get_predc.shtml?year=2010&stn=5595+Portsmouth+Harbor+Entrance&secstn=Salamander+Point,+north+of+&sbfh=%2B0&sbfm=24&fldh=%2B0&fldm=44&sbem=%2B0&sbem=26&ebbh=%2B0&ebbm=45&fldr=1.2&ebbr=0.6&fldavgd=257&ebbavgd=091&footnote=

Rocker Jr., Karl (ed.) 1985, *Handbook of Marine Geotechnical Engineering*, Deep Ocean Technology, Naval Civil Engineering Laboratory, Port Hueneme, CA.

Scher, Stanley H. & Gale, Lawrence J. 1949. *Wind-Tunnel Investigation of the Opening Characteristics, Drag, and Stability of Several Hemispherical Parachutes*, National Advisory Committee for Aeronautics, Langley Aeronautical Laboratory, Washington, Technical Note 1869.

Bluefin. 2010, 'Sub-Sea Batteries', Bluefin Robotic Inc., [Online] Available at: http://www.bluefinrobotics.com/subsea_batteries.htm

WOCE. 2002, 'World Ocean Circulation Experiment Global Data Resource', *National Oceanographic Data Center*, [Online] Available at: <http://woce.nodc.noaa.gov/wdiu>

Young, Warren C. 1989, *Roark's Formulas for Stress and Strain*. 6th edn, McGraw-Hill, New York.

APPENDICES

APPENDIX A

SEDIMENT INTERACTIONS

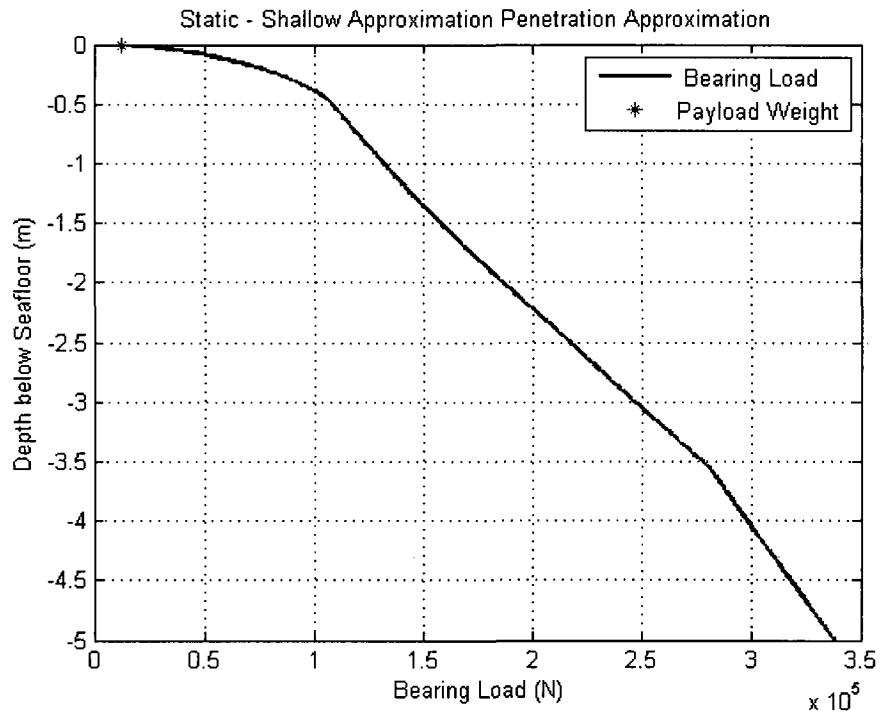


Figure 46: Static penetration for a side impact in siliceous ooze

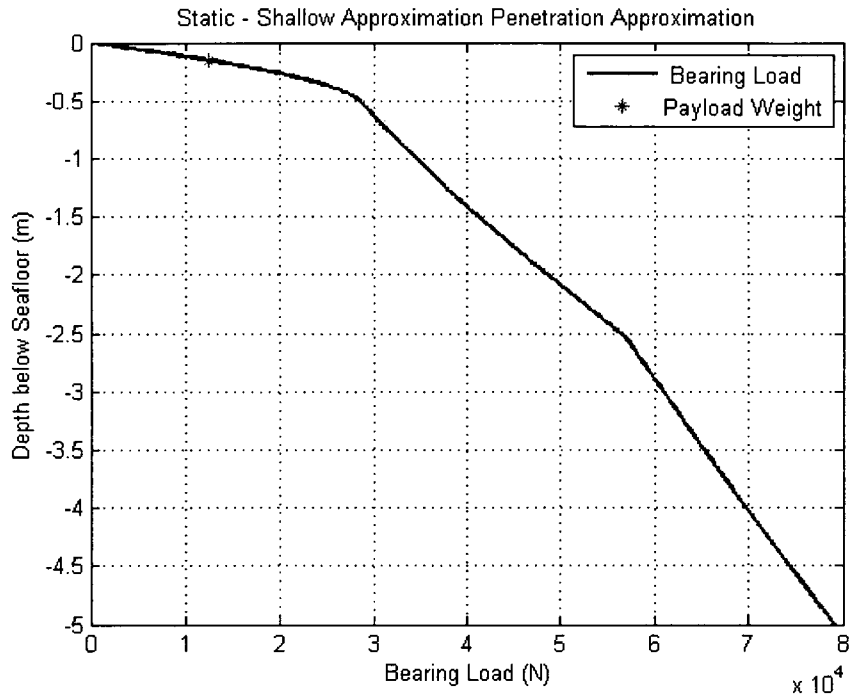


Figure 47: Static penetration for a head-on impact in siliceous ooze

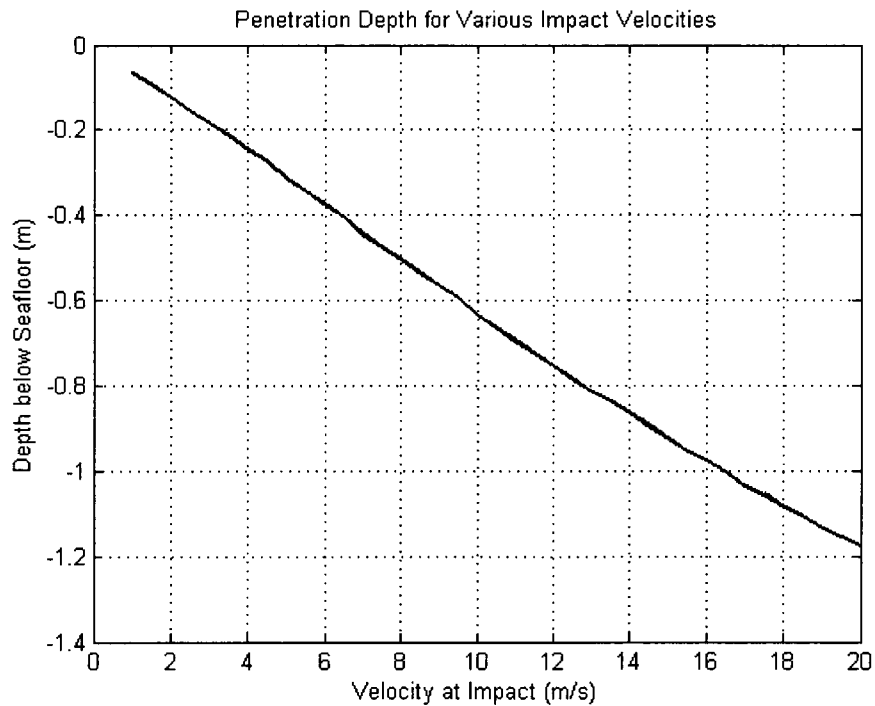


Figure 48: Dynamic penetration depth for a side impact in siliceous ooze

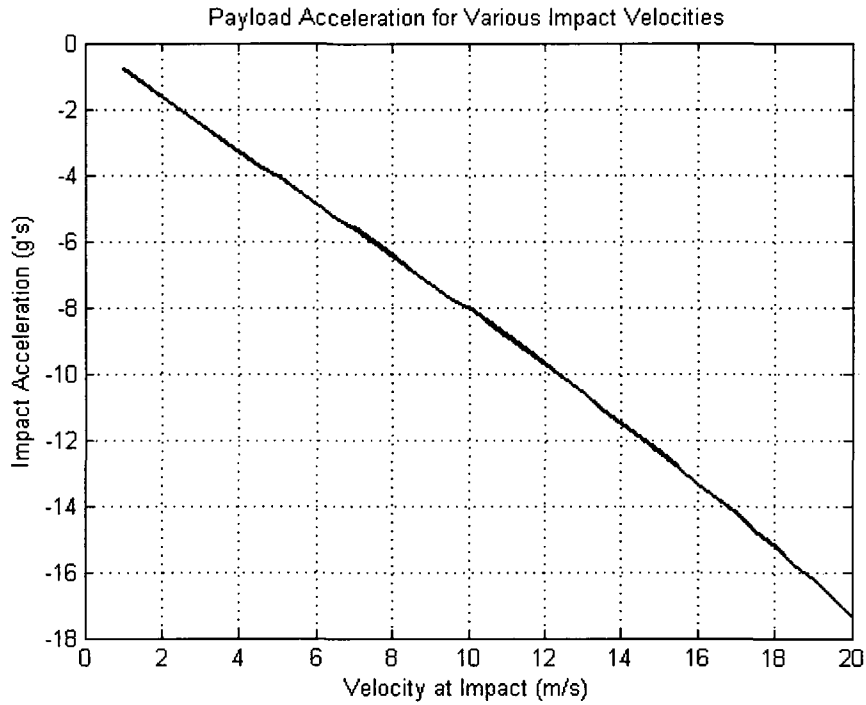


Figure 49: Deceleration for a side impact in siliceous ooze

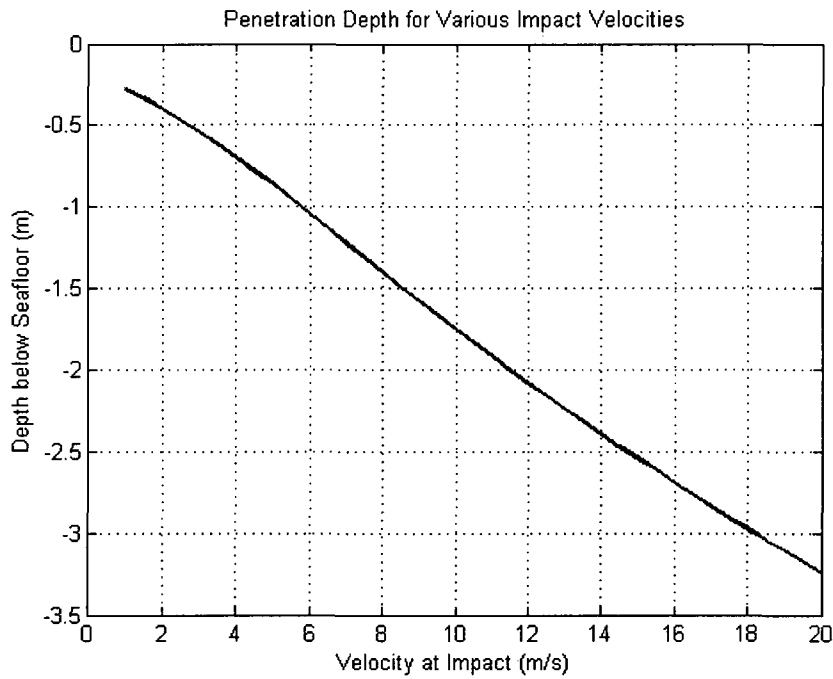


Figure 50: Dynamic penetration depth for a head-on impact in siliceous ooze

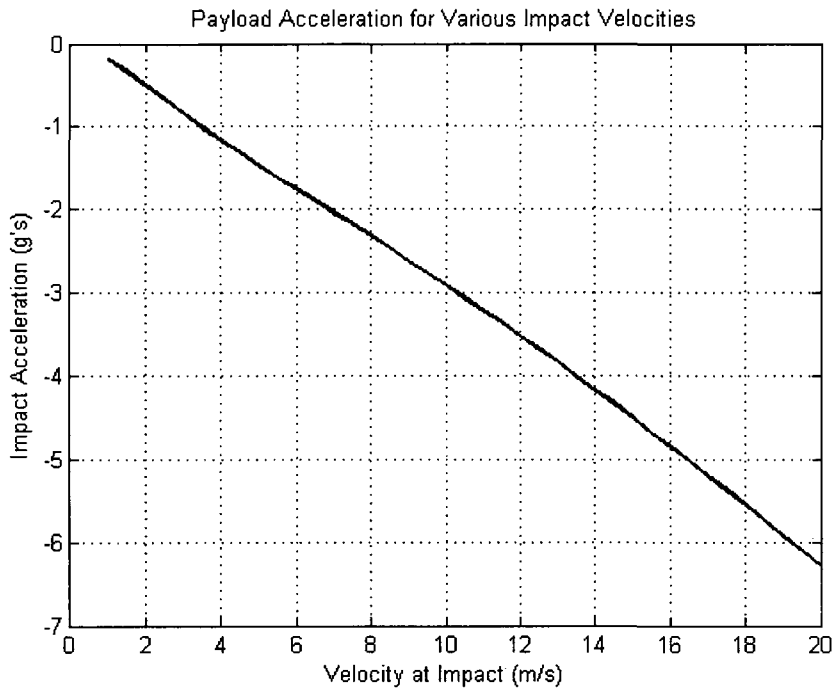


Figure 51: Deceleration for a head on impact in siliceous ooze

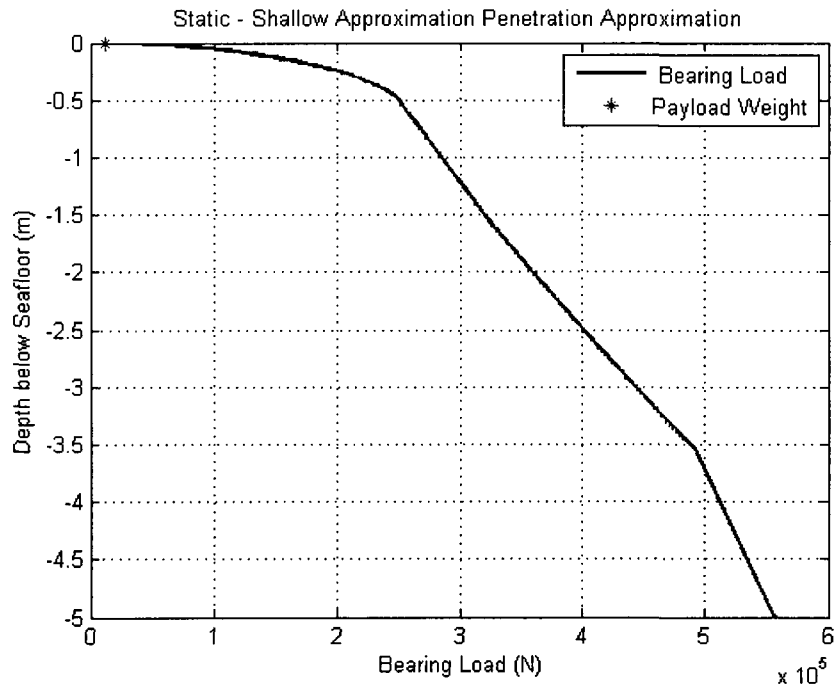


Figure 52: Static penetration for a side impact in fine calcareous ooze

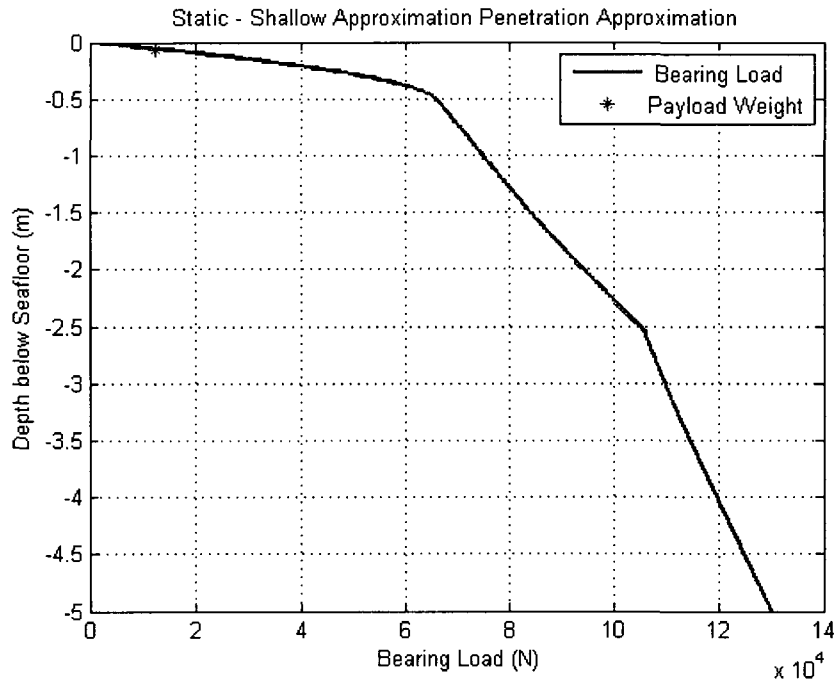


Figure 53: Static penetration for a head-on impact in fine calcareous ooze

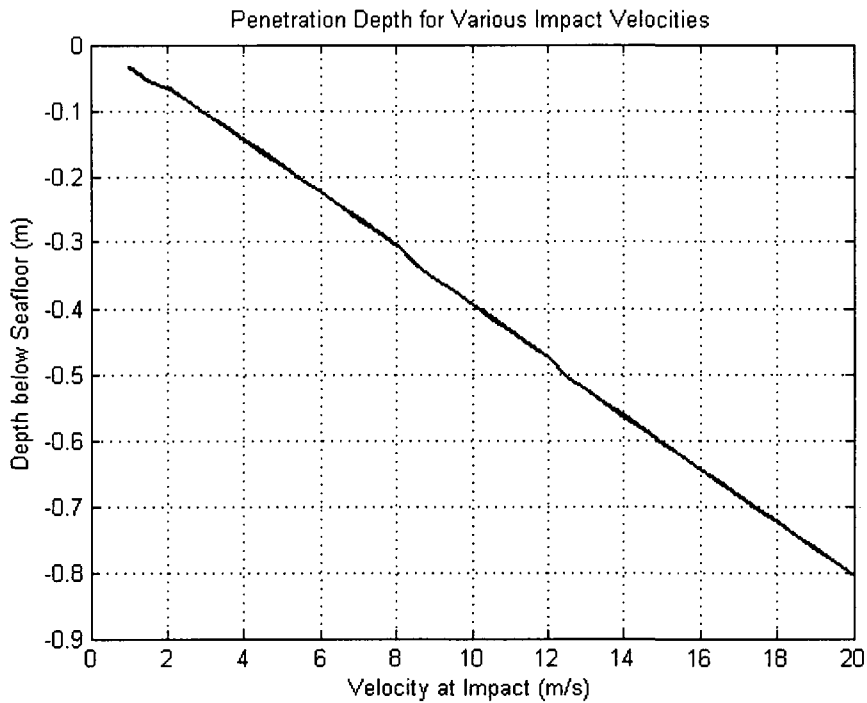


Figure 54: Dynamic penetration depth for a side impact in fine calcareous ooze

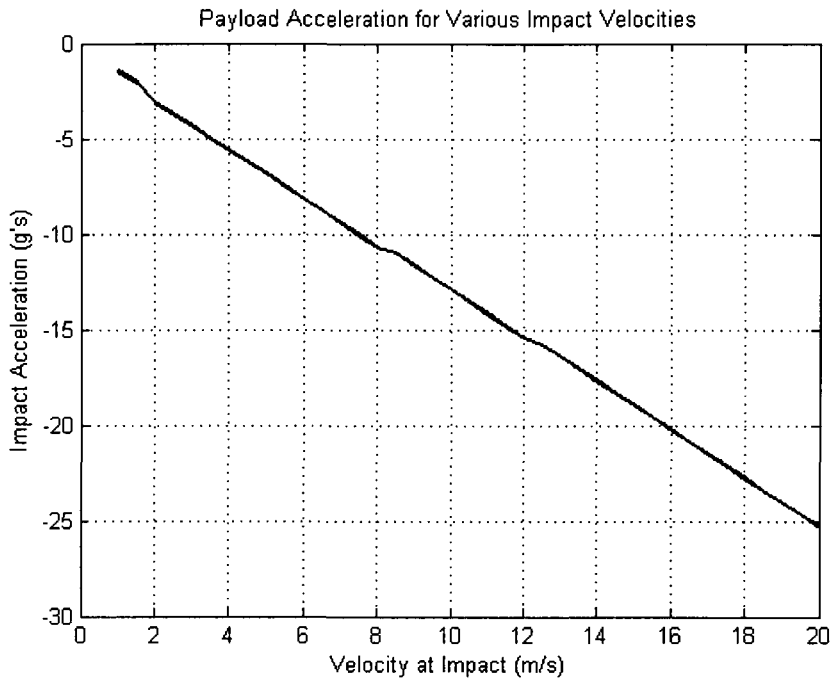


Figure 55: Deceleration for a side impact in fine calcareous ooze

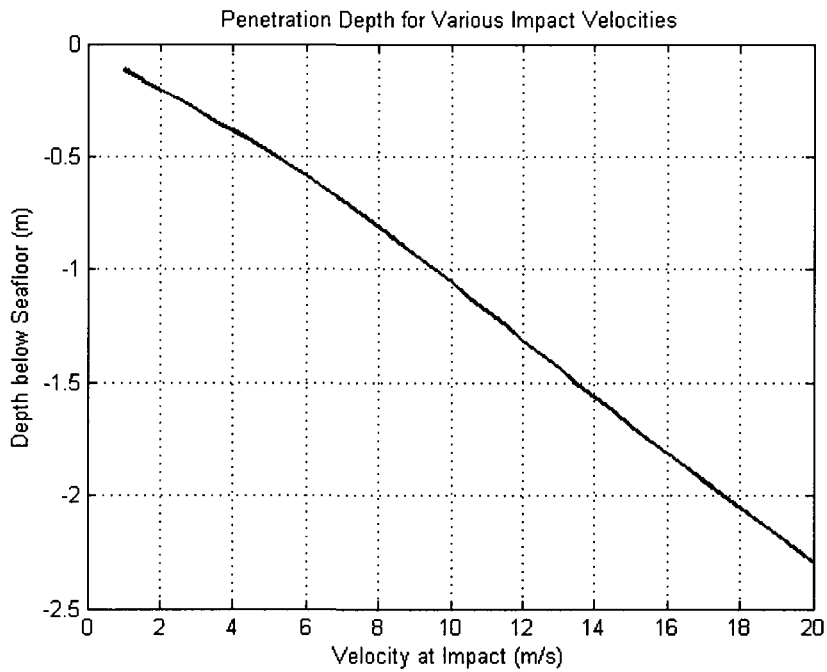


Figure 56: Dynamic penetration depth for a head-on impact in fine calcareous ooze

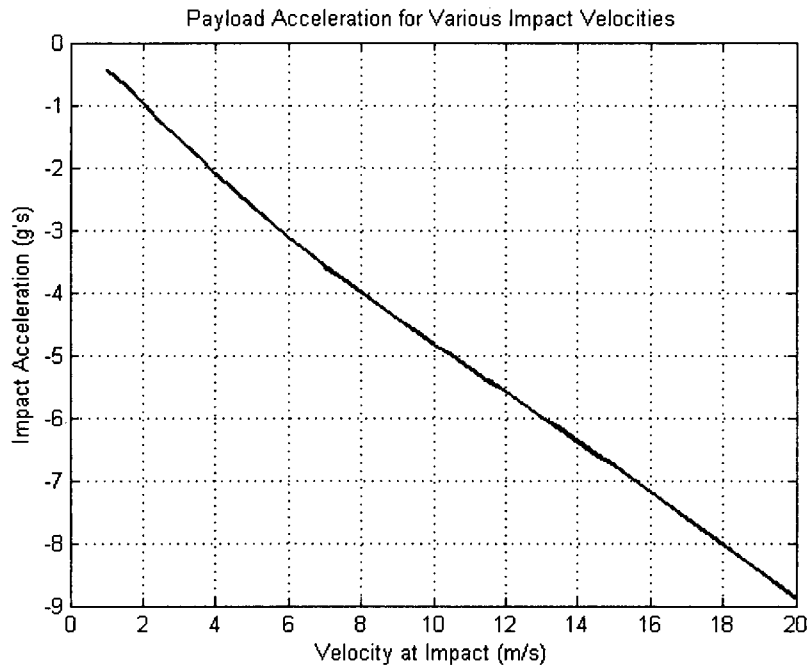


Figure 57: Deceleration for a head on impact in fine calcareous ooze

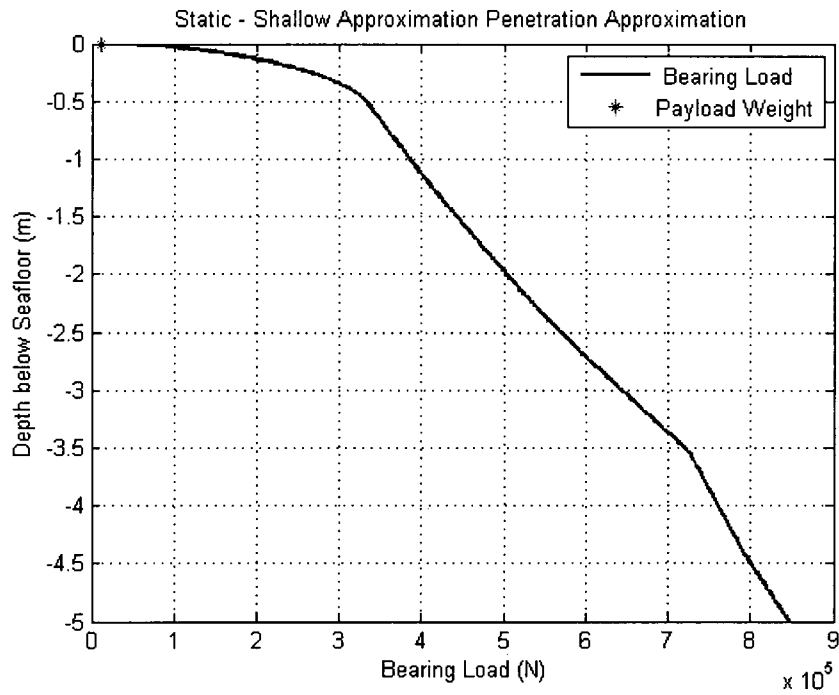


Figure 58: Static penetration for a side impact in coarse calcareous ooze

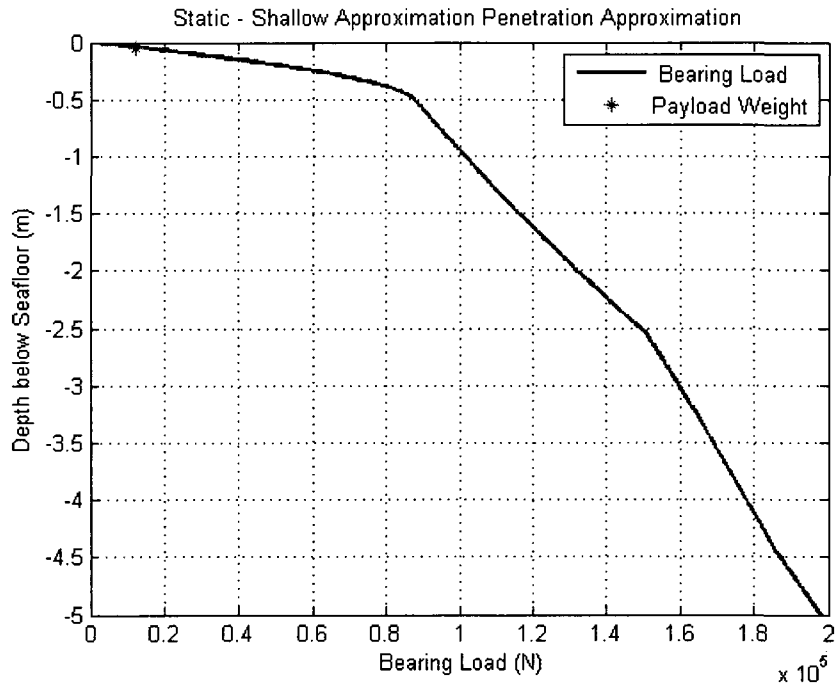


Figure 59: Static penetration for a head-on impact in coarse calcareous ooze

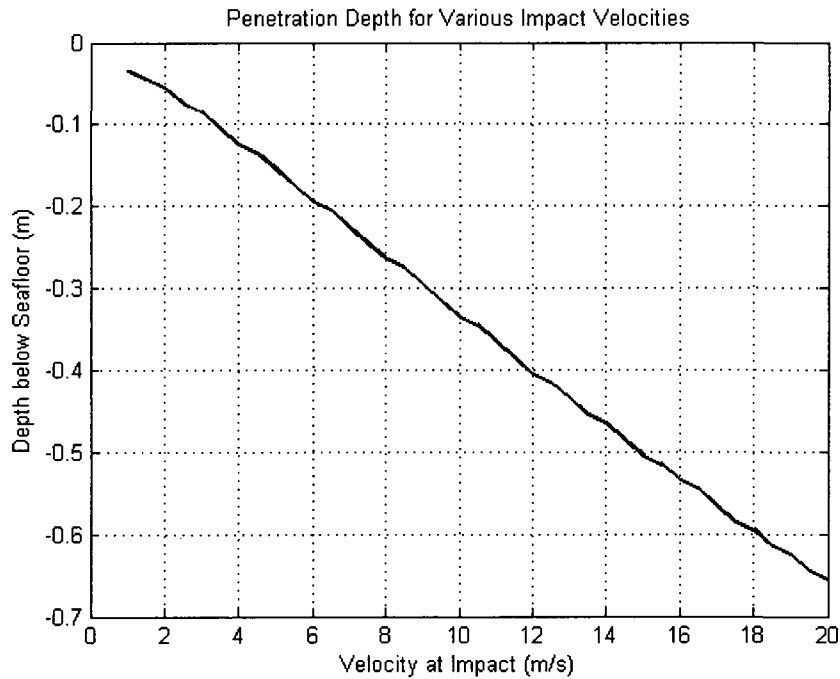


Figure 60: Dynamic penetration depth for a side impact in coarse calcareous ooze

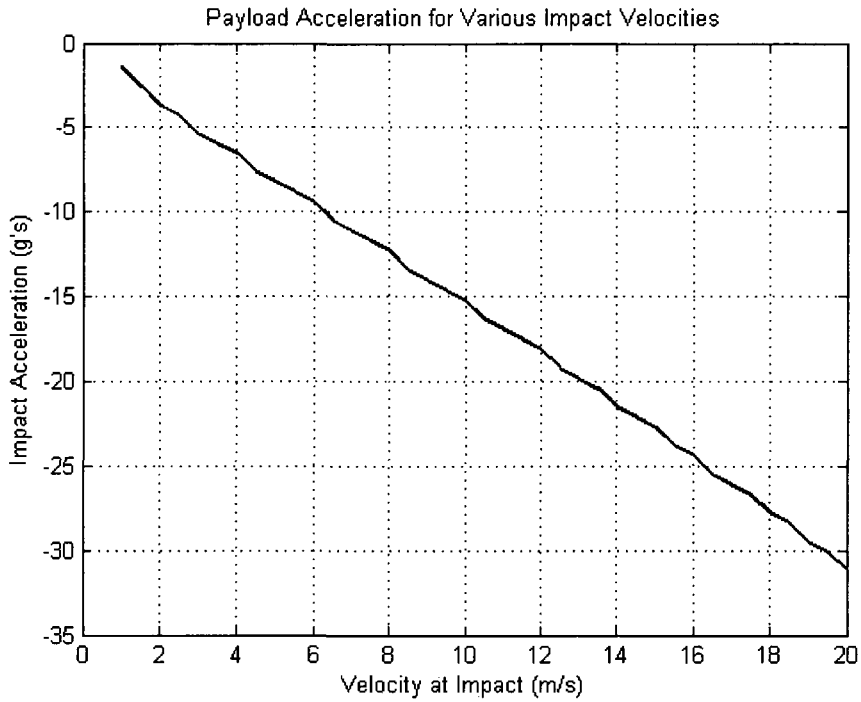


Figure 61: Deceleration for a side impact in coarse calcareous ooze

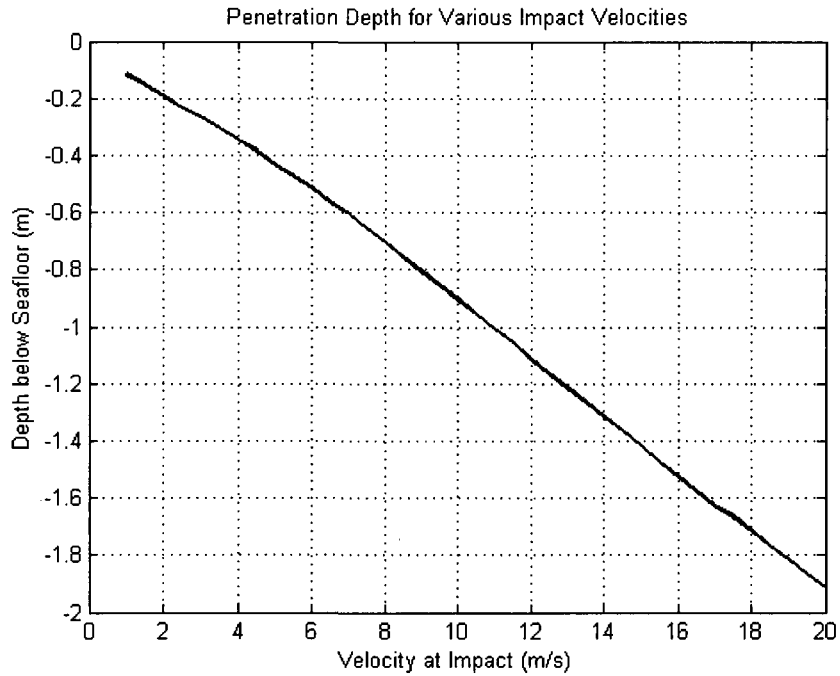


Figure 62: Dynamic penetration depth for a head-on impact in coarse calcareous ooze

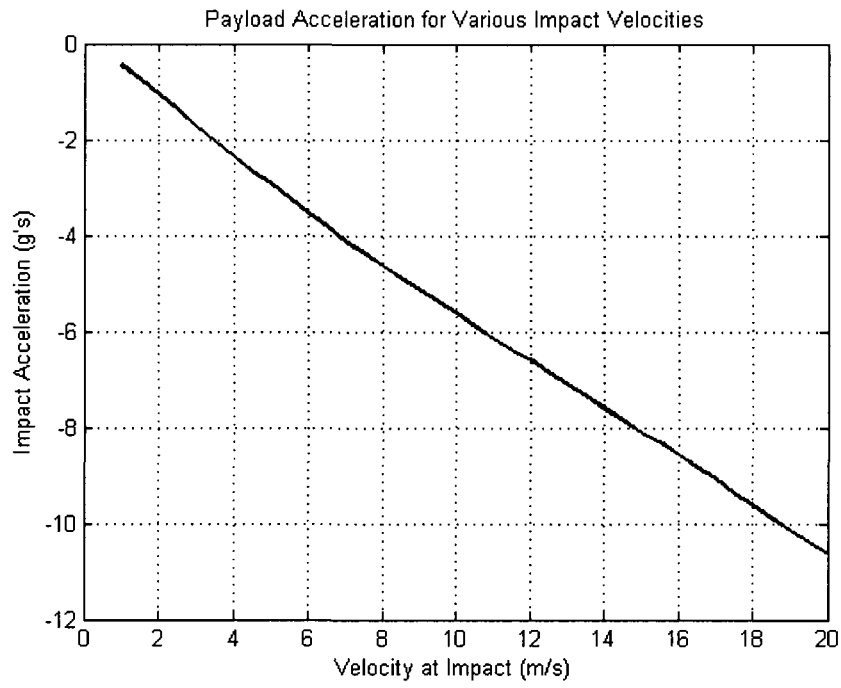
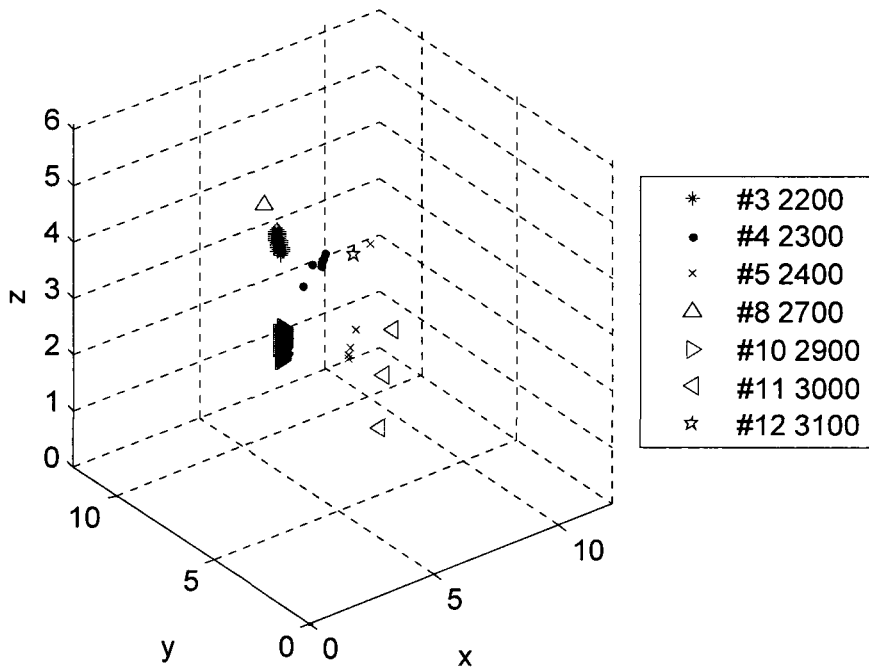


Figure 63: Deceleration for a head on impact in coarse calcareous ooze

APPENDIX B

HTI TANK TESTING RESULTS

HTI Data beginning 27-Apr-2010 13:00:05



HTI Data beginning 27-Apr-2010 13:00:05

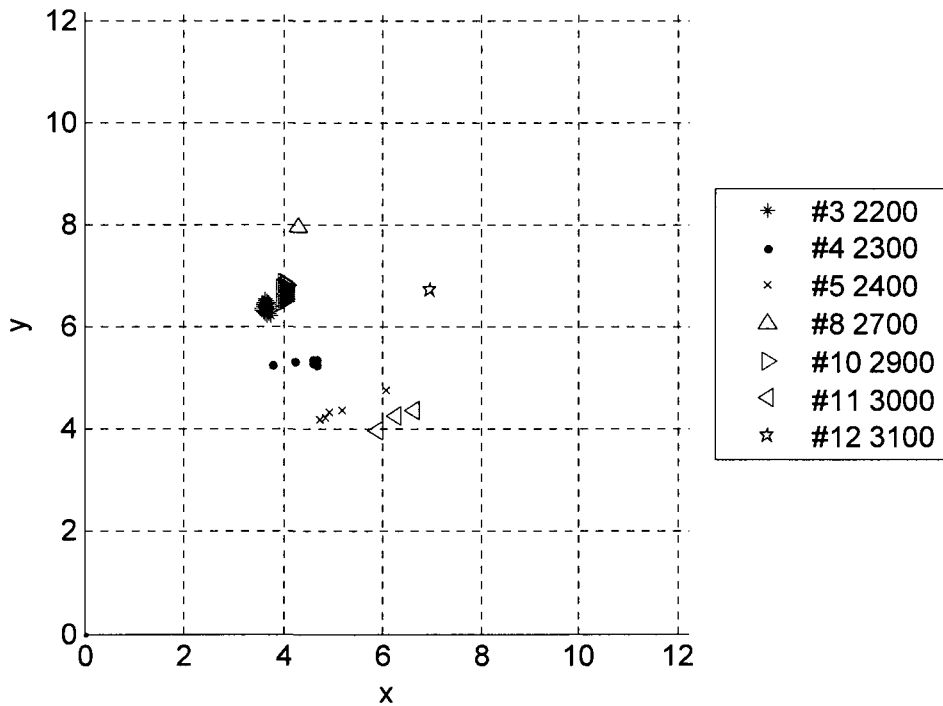
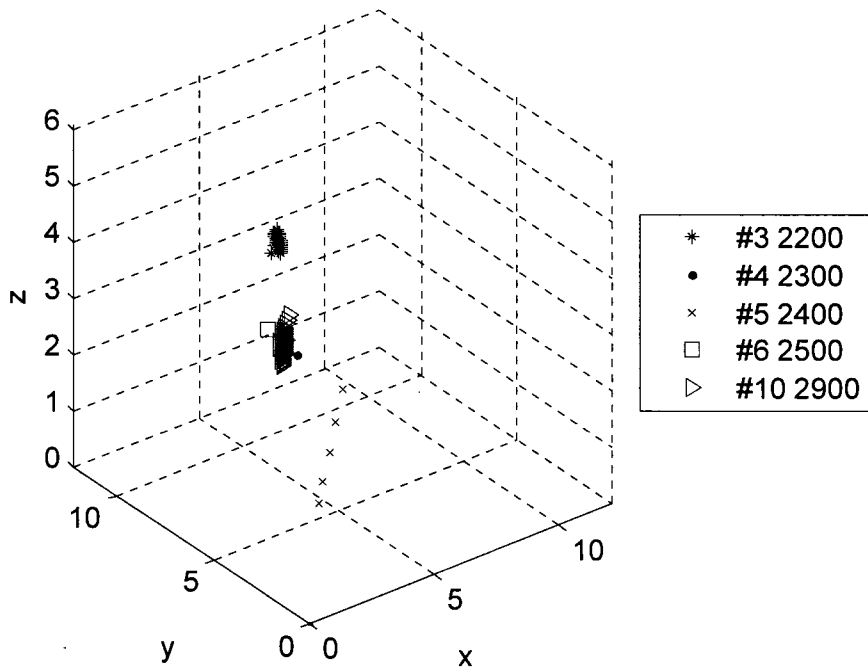


Figure 64: HTI results from static pool testing April 27, 2010 at 1 pm (3D and top view)

HTI Data beginning 27-Apr-2010 14:00:04



HTI Data beginning 27-Apr-2010 14:00:04

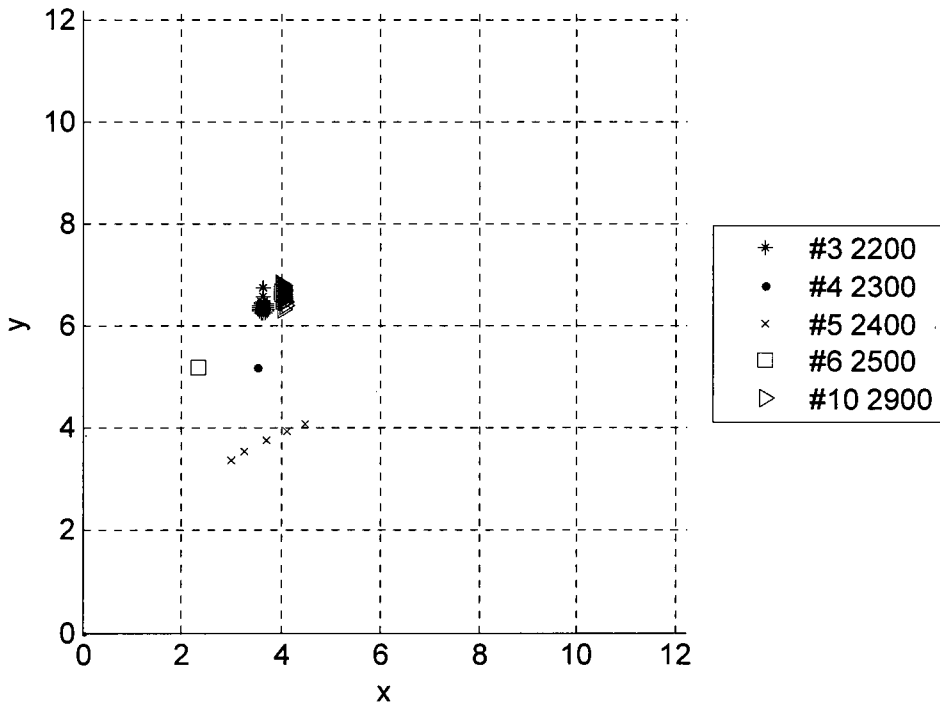
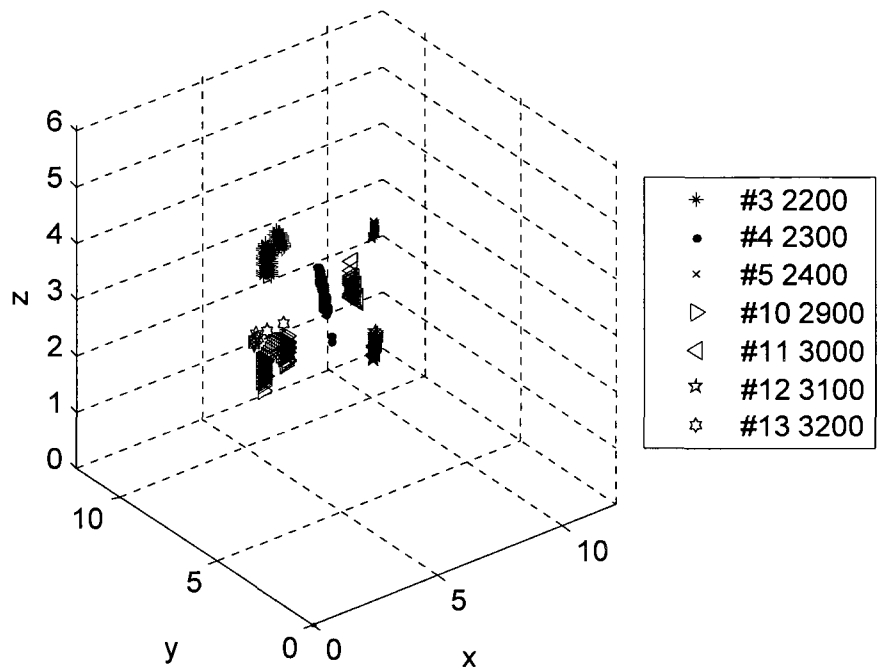


Figure 65: HTI results from static pool testing April 27, 2010 at 2 pm (3D and top view)

HTI Data beginning 27-Apr-2010 14:37:19



HTI Data beginning 27-Apr-2010 14:37:19

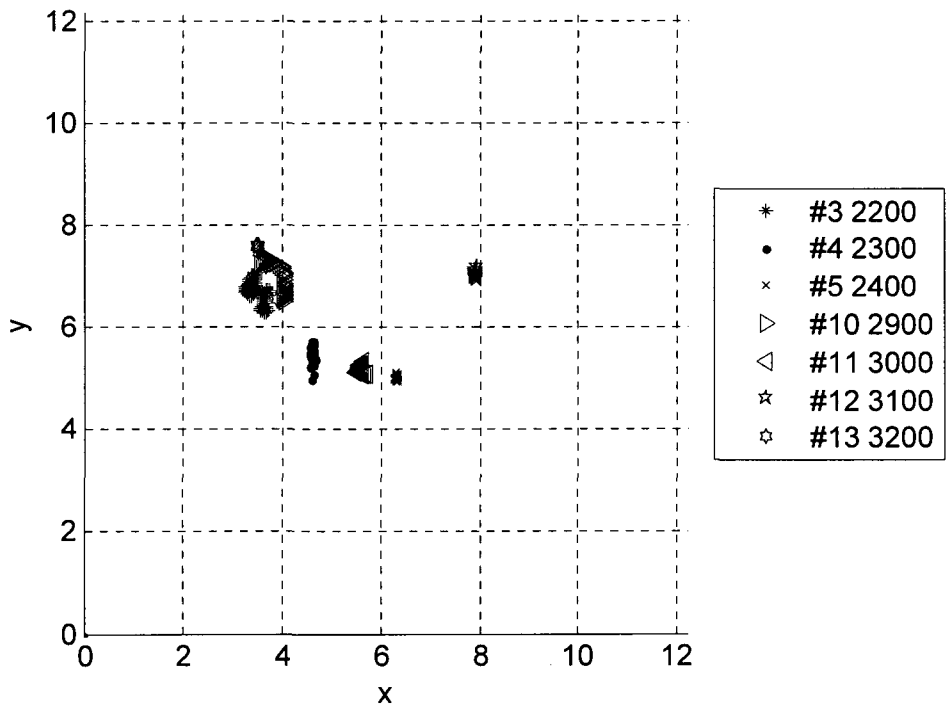
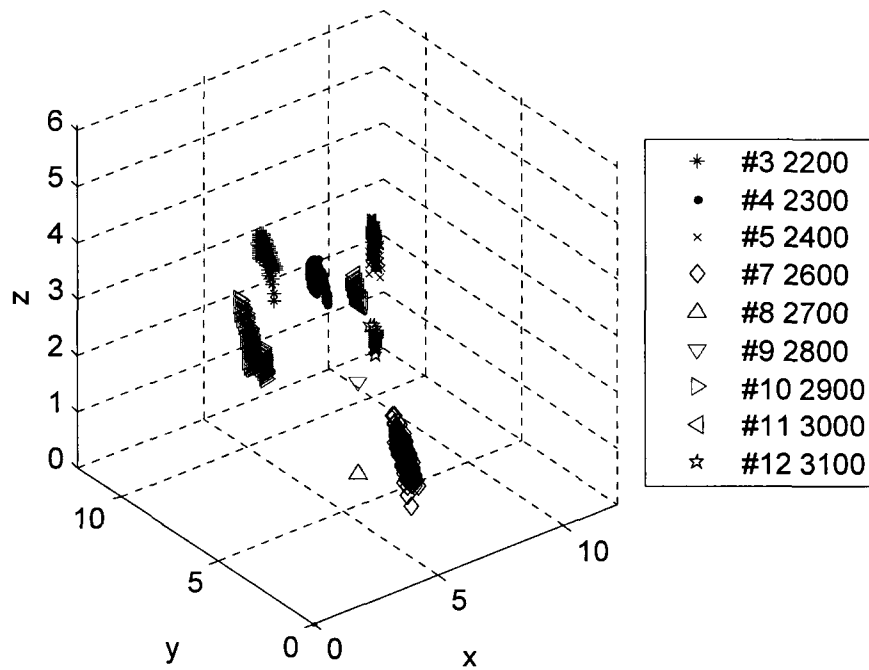


Figure 66: HTI results from static pool testing April 27, 2010 at 2:37 pm (3D and top view)

HTI Data beginning 27-Apr-2010 15:00:05



HTI Data beginning 27-Apr-2010 15:00:05

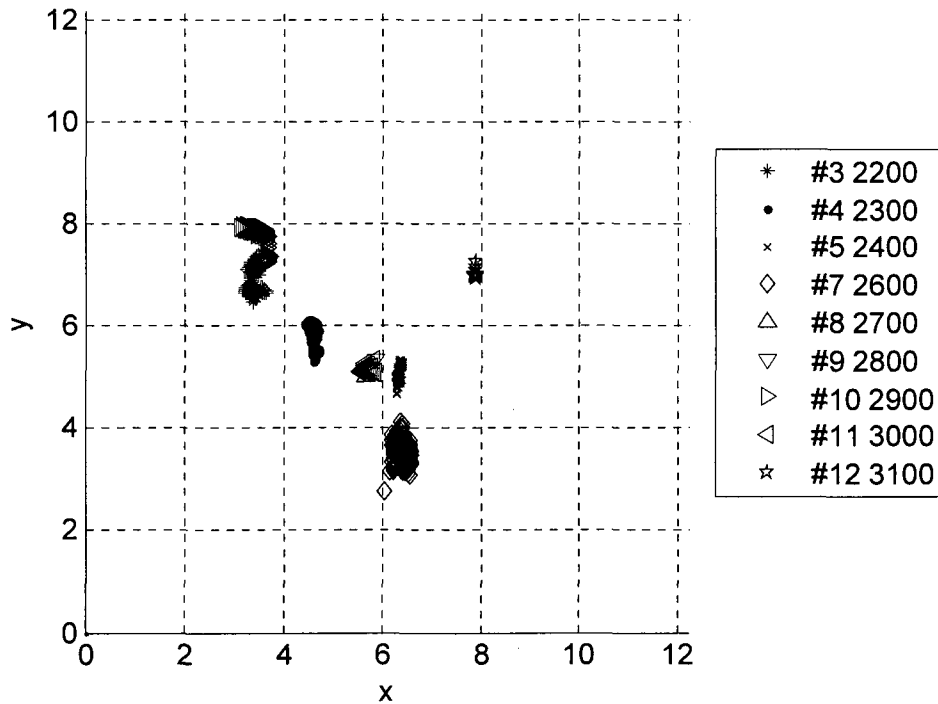
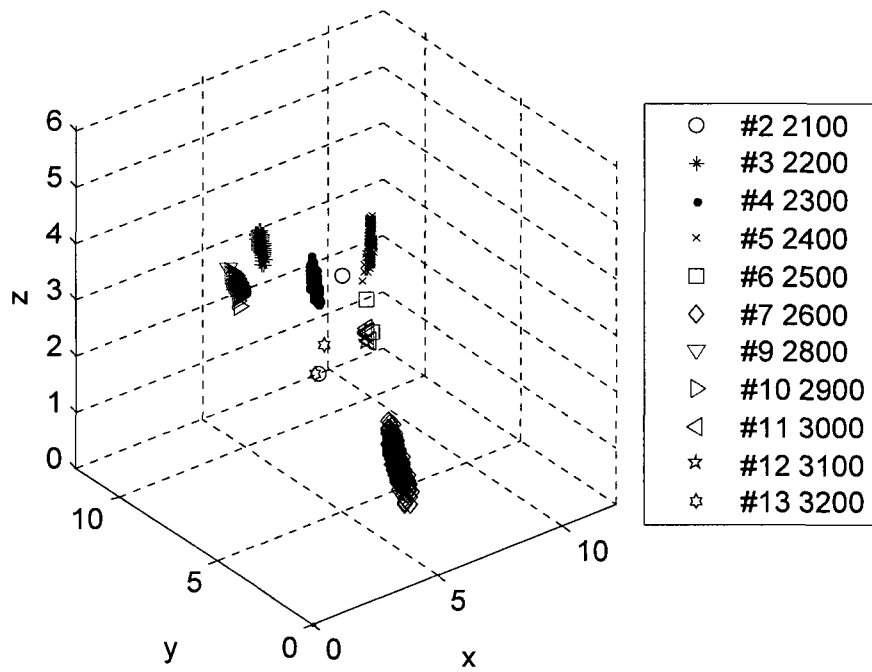


Figure 67: HTI results from static pool testing April 27, 2010 at 3 pm (3D and top view)

HTI Data beginning 28-Apr-2010 09:00:05



HTI Data beginning 28-Apr-2010 09:00:05

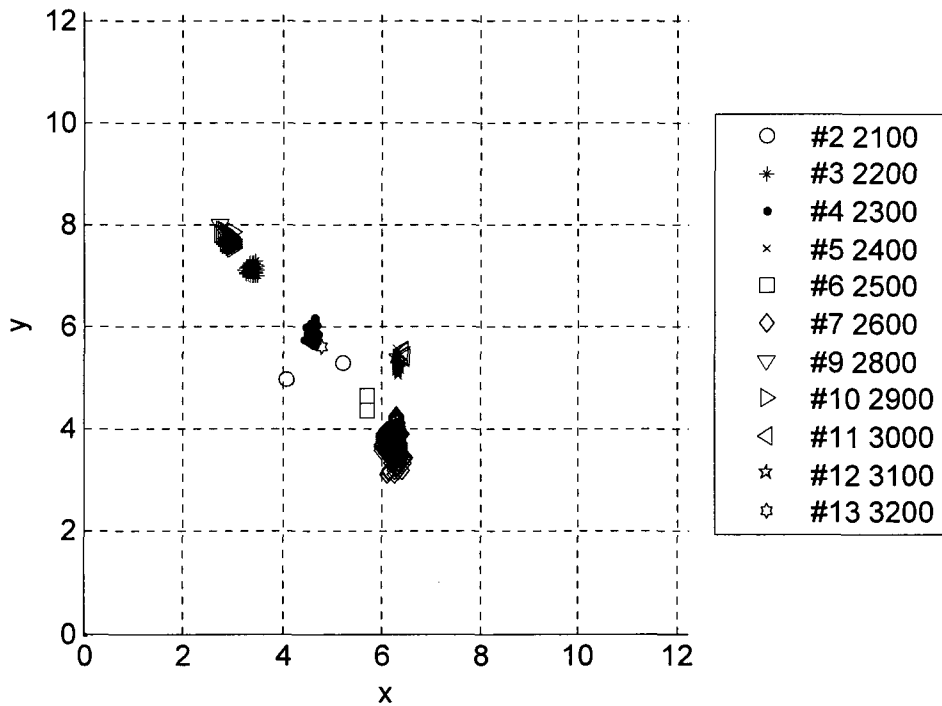
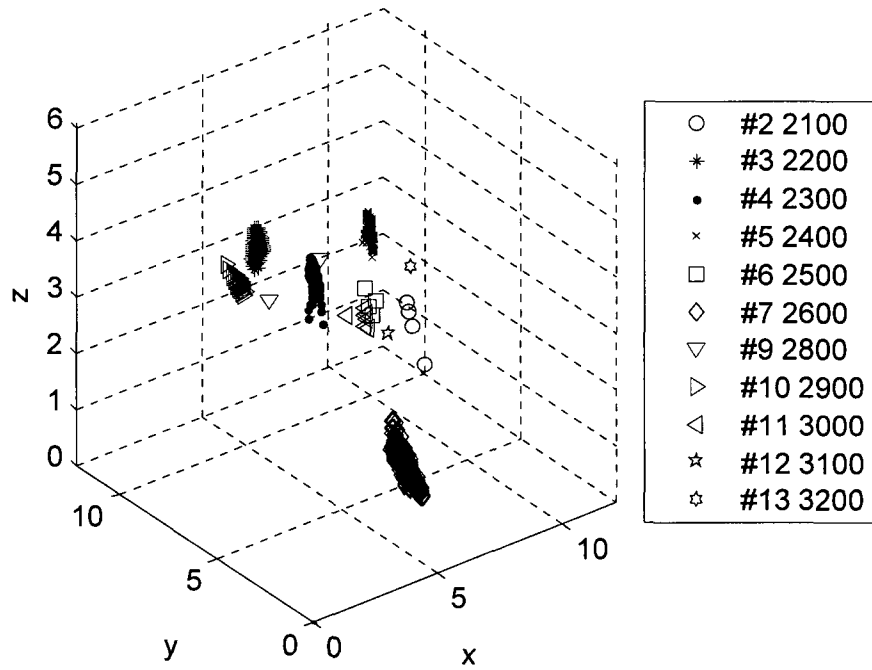


Figure 68: HTI results from static pool testing April 28, 2010 at 9 am (3D and top view)

HTI Data beginning 28-Apr-2010 10:00:06



HTI Data beginning 28-Apr-2010 10:00:06

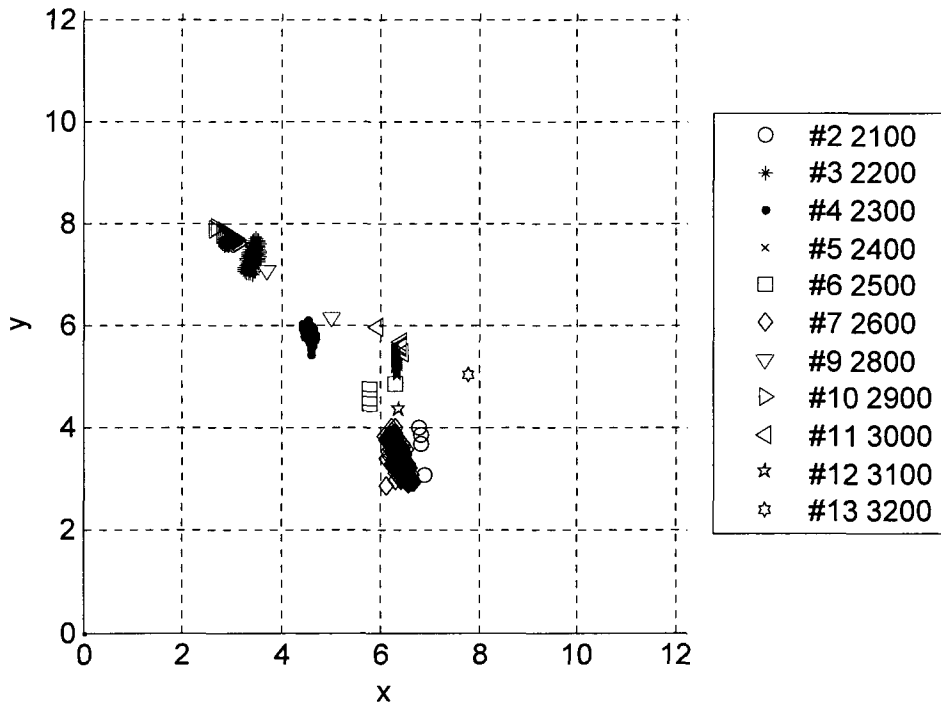
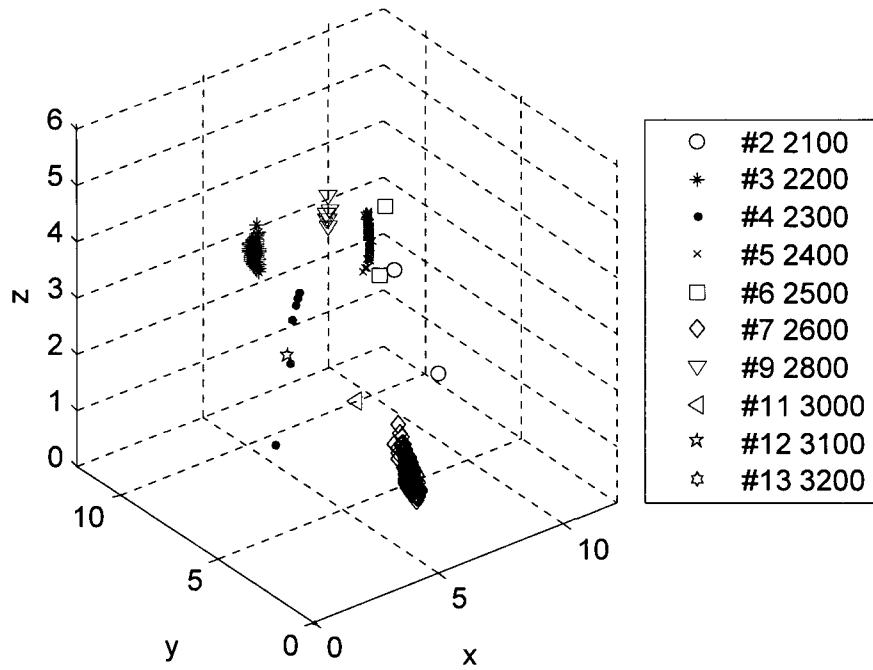


Figure 69: HTI results from static pool testing April 28, 2010 at 10 am (3D and top view)

HTI Data beginning 28-Apr-2010 11:00:07



HTI Data beginning 28-Apr-2010 11:00:07

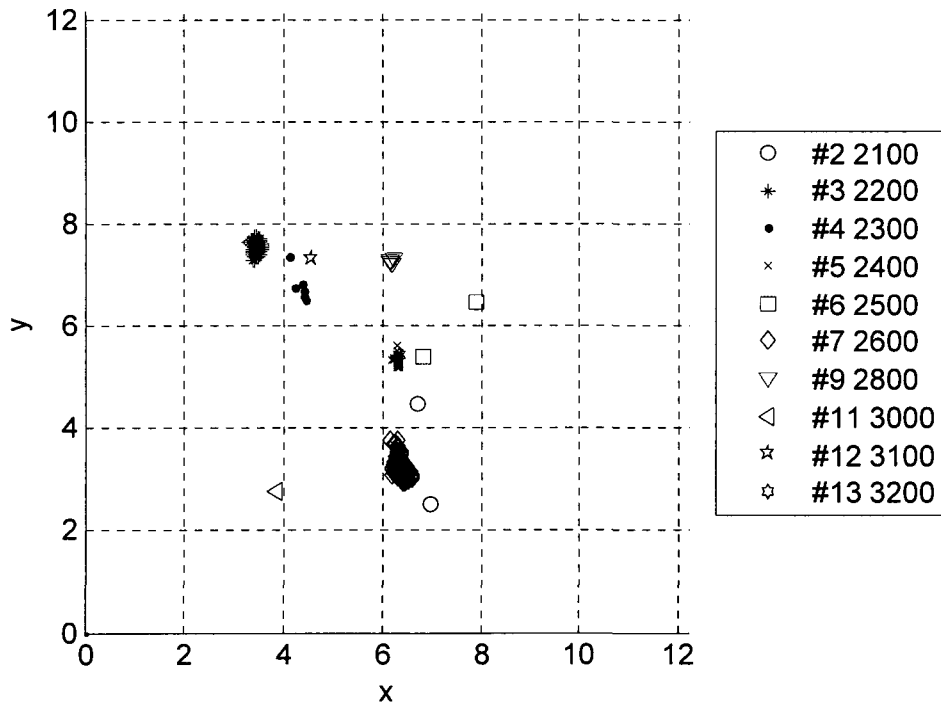
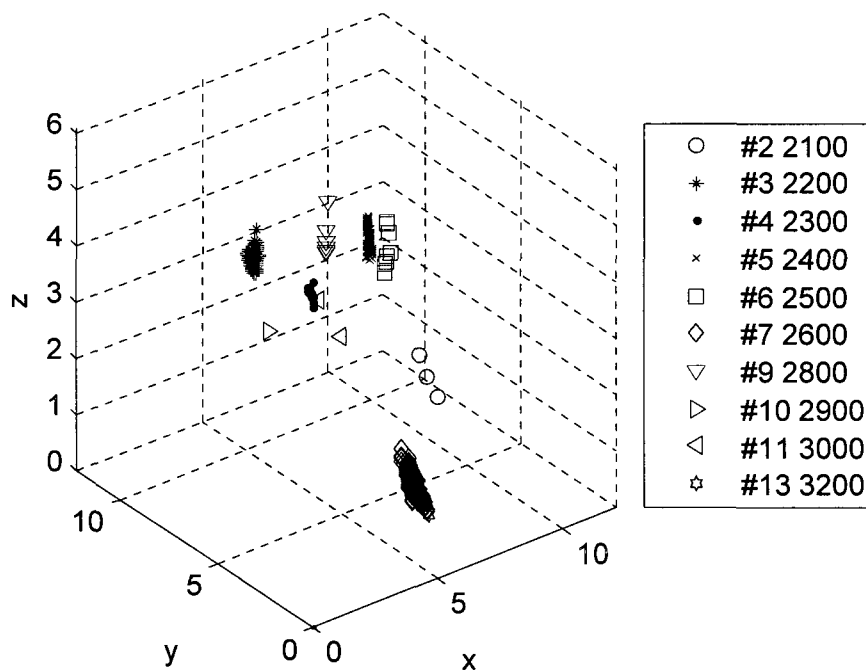


Figure 70: HTI results from static pool testing April 28, 2010 at 11 am (3D and top view)

HTI Data beginning 28-Apr-2010 12:00:08



HTI Data beginning 28-Apr-2010 12:00:08

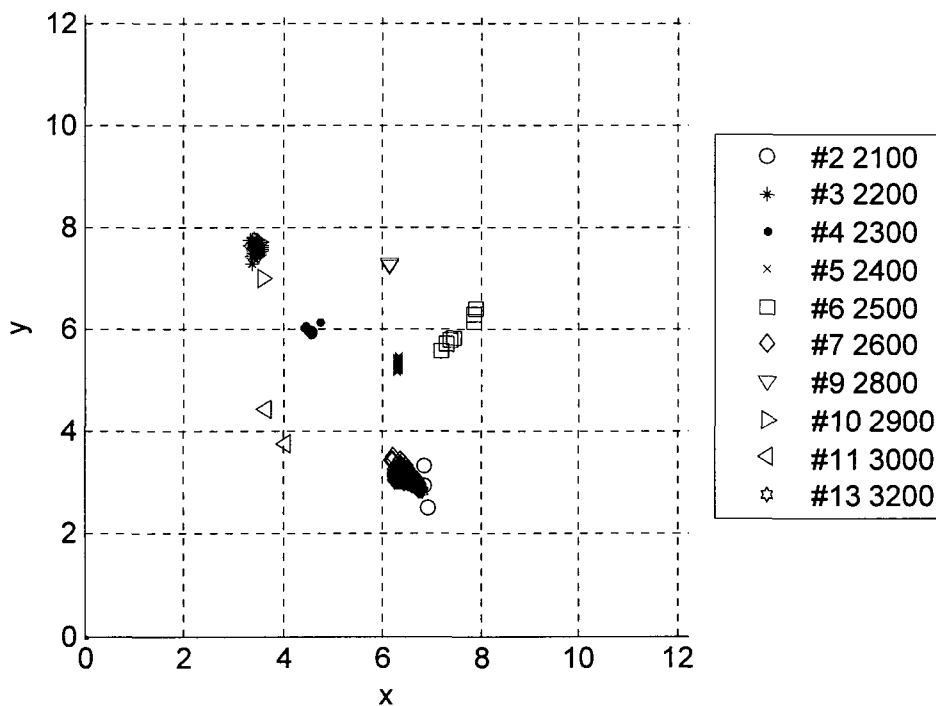
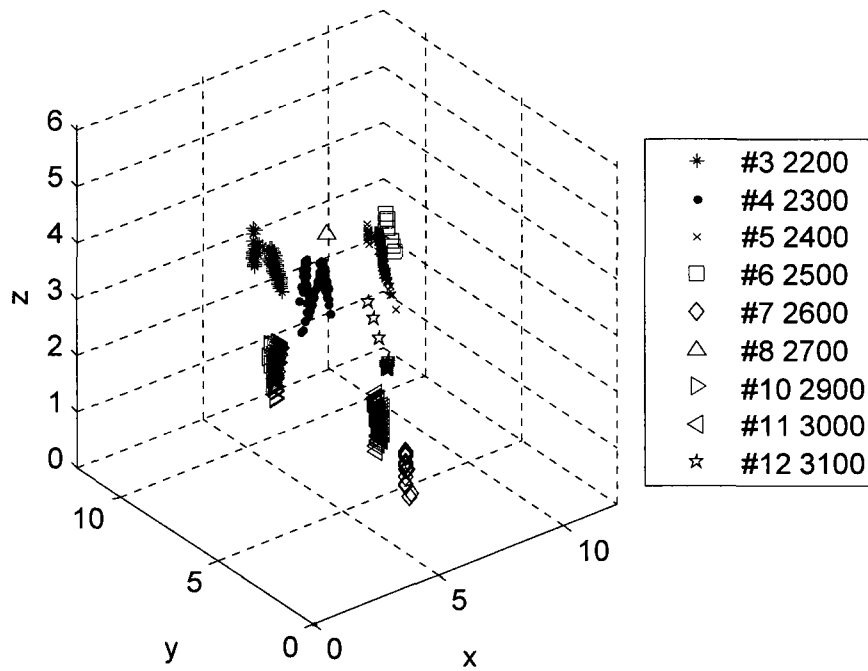


Figure 71: HTI results from static pool testing April 28, 2010 at 12 pm (3D and top view)

HTI Data beginning 28-Apr-2010 13:00:02



HTI Data beginning 28-Apr-2010 13:00:02

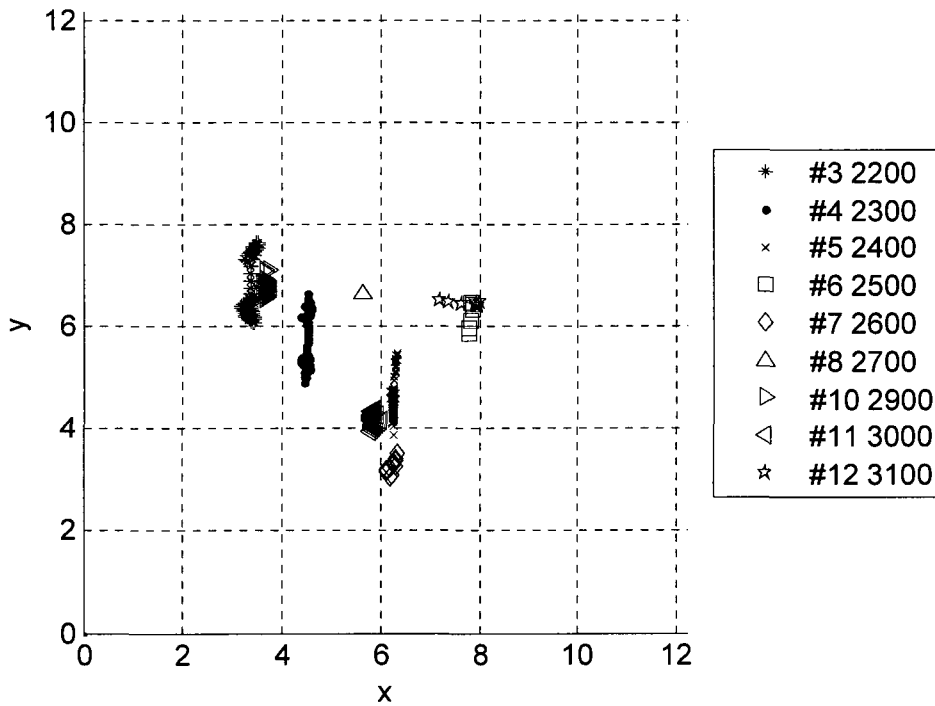


Figure 72: HTI results from static pool testing April 28, 2010 at 1 pm (3D and top view)